

**STUDIES OF MAGNETIC AND TRANSPORT
PROPERTIES OF
DISORDERED SYSTEMS**

**THESIS SUBMITTED FOR THE DEGREE OF
DOCTOR OF PHILOSOPHY (SCIENCE)
OF THE
UNIVERSITY OF JADAVPUR**

Mitali Banerjee

**SATYENDRANATH BOSE NATIONAL CENTRE
FOR BASIC SCIENCES
JD BLOCK, SECTOR 3, SALT LAKE CITY
KOLKATA 700 098, INDIA**

APRIL, 2011

CERTIFICATE FROM THE SUPERVISOR(S)

This is to certify that the thesis entitled “**Studies of magnetic and transport properties of disordered systems**” submitted by **Mitali Banerjee**, who got her name registered on **August 12, 2008** for the award of **Ph.D. (Science)** degree of **Jadavpur University**, is absolutely based upon her own work under the supervision of **Professor Abhijit Mookerjee & Professor A. K. Majumdar** at **S. N. Bose National Centre For Basic Sciences, Kolkata, India** and that neither this thesis nor any part of it has been submitted for any degree/diploma or any other academic award anywhere before.

ABHIJIT MOOKERJEE

Distinguished Professor

(Supervisor)

Date :

A. K. MAJUMDAR

Emeritus Scientist

(Supervisor)

Date :

Material Sciences,
S N Bose National Centre For Basic Sciences,
Block JD, Sector III, Salt Lake, Kolkata 700098
India.

*TO
MY BEST FRIEND*

ACKNOWLEDGEMENTS

First of all I want to express my sincerest gratitude to Prof. Abhijit Mookerjee and Prof. A. K. Majumdar for being such wonderful thesis advisers. Their remarkable insights into various problems, persistence and insistence on clarity have helped me in learning numerous things. Prof. Mookerjee is a dream supervisor to any student; his encouragements for experimental condensed matter physics is really overwhelming. Starting from deciding the projects for my thesis work to its successful completion, nothing could have been this smooth if Prof. Majumdar would not have been my mentor. I must mention that, I could access the numerous laboratories across India for my work is due to his wonderful reputation in low temperature experimental physics. In short, working with both of them has been a rich and rare experience and I am indebted to them for reasons much beyond the pages of this thesis.

I would like to take the opportunity to appreciate the benefits I have received from my collaborators, without their support this thesis would not have taken the present form. I am grateful to Prof. A K Nigam of Tata Institute of Fundamental Research, Mumbai for giving me opportunity to use the experimental facilities in his laboratory whenever it is needed. In fact almost three quarter of my present thesis work is the result of his strong support and cooperation. I am also thankful to Dr. D M Phase, Dr. R J Chowdhury, Dr. Alok Banerjee, Dr. R Rawat, Dr. V R Reddy and Dr. V Ganeshan of UGC-DAE Consortium for Scientific Research, Indore and Dr. G S Lodha, Mr. Sanjay Rai and Mrs. Pragya Tiwari of Raja Ramanna Centre for Advanced Technology, Indore and Dr. K G M Nair of Indira Gandhi Centre for Advance Research, Kalapakkam for giving me the opportunity to use their laboratories for synthesis and characterizations of thin film samples. This thin film project is an integral part of the present thesis, and thanks to all my collaborators, whose interest and support made me able to learn various important technicalities of the whole process. Finally I would like to thank Prof. Avinash Singh of Indian Institute of Technology, Kanpur for his active involvement in the analysis of the experimental data and also providing sufficient theoretical support to strengthen the findings. Apart from these, I want to thank Dr. P. Khatua of Indian Institute of Science Education and Research, Kolkata, and Dr. S Chakroborty of Emerson Electric, Minnesota, and Prof. R Chatterjee of Indian Institute of Technology, Delhi and Dr. A Mitra of National Metallurgical Laboratory, Jamshedpur and Dr. A Das of Bhaba Atomic Research Centre, Mumbai, Dr. Sindhunil Roy Burman and Dr. Gautam Sinha of Raja Ramanna Centre for Advanced Technology, Indore and Dr. Shankar Dhar of National University of Singapore, and Dr. P. Mitra of Indian Institute of Science Education and Research, Kolkata for

their active support whenever needed. I would also like to thank Prof. R. Ranganathan of Saha Institute of Nuclear Research, Kolkata and Prof. Anjan Burman of our centre for many critical discussions which helped me in improving my interpretations. Amongst the other faculty members of S N Bose National Centre for Basic Sciences, I would like to thank Prof. J K Bhattacharjee, Prof. Amitabha Lahiri, Prof. Rabin Banerjee, and Prof. Priya Mahadevan for not only being wonderful course instructors but providing insights into various problems whenever needed.

I would like to mention this long six year stay in this institute, gave me three wonderful friends, the lovely bond I share with Abhi, Shreemoyee and Sourav, will remain in my heart forever. Apart from them I would like to mention the love and support I have received from my seniors as well as juniors, Tuhin da, Rupa di, Aftab Bhaiya, Manoj Bhaiya, Harun da, Chadu da, Moshior, Bulbul, Rajiv, Ambika, Prashant, Debraj, Soumajit, Pampa, Swastika, Hira, Indrakshi, Rudranil, Raka, Jalla, Debmalya and many more. I would like to thank all my friends for being part of my life. My special thanks to Moshior and Debraj for helping me with LaTeX commands whenever I am stuck. This life would not have been so good without these wonderful people around for all these years.

I would like to acknowledge financial support from the University Grant Commission, Government of India and S N Bose National Centre for Basic Sciences during the period of this stay. I would like to thank our Director, Prof. A K Raychaudhuri for increasing the in-house facilities for the students. I should not forget to mention the overwhelming support of the non-academic staff of the centre and the gang of gardeners who make our centre look so gorgeous round the year.

Finally I want to express my love and gratitude to my best friend, without her I must not have been what I am today. I also want to thank my mother for being what she is and my father for showing me how to have fun in life and my little brother for being such a lovely brat. The list will remain incomplete if I do not express my love to Jayanta, who has been an indispensable part of my life. He has not only shared my dreams but encouraged me to fight for it till there is hope. He has been a wonderful companion through every thick and thin, making it a wonderful journey since we met.

Mitali Banerjee
S.N.Bose National Centre for Basic Sciences,
Kolkata, India.

List of Publications

1. **Quantum interference effects and magnetic scattering in the electrical resistivity of Ni nanocrystallites in TiN matrix.**
P. Khatua, T. K. Nath, Mitali Banerjee and A. K. Majumdar
Appl. Phys. Lett. **92** 193106 (2008).
2. **Electrical resistivity in Co-rich pseudobinary NiCr ferromagnetic metallic glasses from 1.5 to 300 K.**
Mitali Banerjee Swapan Chakraborty and A. K. Majumdar
J. Appl. Phys. **103** 123702 (2008).
3. **Structural Characterization of PLD-grown Nanometer Size Ferromagnetic NiFeMo Films.**
Mitali Banerjee A. K. Majumdar, R J Choudhary, D M Phase, S Rai, Pragya Tiwari, G S Lodha
MRS Proceedings **1200E** G09-05 (2010).
4. **Magnetism in NiFeMo disordered alloys: experiment and theory.**
Mitali Banerjee, A. K. Majumdar, Abhijit Mookerjee, Rudra Banerjee, Biplab Sanyal and A. K. Nigam
Physica B **405**, Issue 20, 4287-4293 (2010).
5. **Magnetism in FeNiW disordered alloys: experiment and theory.**
Mitali Banerjee, Abhijit Mookerjee, A. K. Majumdar, Rudra Banerjee, Biplab Sanyal and A. K. Nigam.
J. Magn. Magn. Mater. **322** Issue 21, 3558-3564 (2010).
6. **Fe_{3.3}Ni_{83.2}Mo_{13.5}: does it show spin-glass behaviour at low temperatures?**
Rudra Banerjee, Mitali Banerjee, A. K. Majumdar, Abhijit Mookerjee, Biplab Sanyal and A. K. Nigam
Journal of Physics : Condens. Matter **23** 106002 (2011).
7. **Signature effects of spin clustering and distribution of spin couplings on magnetization behaviour in Ni-Fe-Mo and Ni-Fe-W alloys.**
Mitali Banerjee, Avinash Singh, A. K. Majumdar and A. K. Nigam
(Communicated to J. Phys: Cond. Matt) : (Cond-mat/arXiv:1101.0343v2)
8. **Structural and magnetic characterization of nanometer size NiFeMo alloy films.**

Mitali Banerjee, A. K. Majumdar, R. J. Chowdhury, D. M. Phase, Alok Banerjee
Pragya Tiwari, S. Rai and G. S. Lodha.
(Communicated to J. Appl. Phys.)

9. **Detailed analysis of various scattering processes in disordered of Ni-rich
NiFeV, NiFeMo, and NiFeW alloys.**

Mitali Banerjee, A. K. Majumdar and A. K. Nigam
(To be communicated)

Contents

1	Introduction	1
1.1	Effects of Disorder on Magnetic Properties	2
1.1.1	Density of States	2
1.1.2	Magnetic Moments	4
1.1.3	Interaction Between Moments	4
1.1.4	Magnetic Anisotropy	6
1.2	Magnetic Order in Disordered Systems	6
1.3	Low-lying Magnetic Excitations	8
1.3.1	Localized-electron Model	8
1.3.2	Itinerant-electron Model	11
1.4	Thermal Critical Phenomenon	12
1.5	Electrical Transport in Disordered Alloys	15
1.5.1	Electron Phonon Scattering	16
1.5.2	Ziman-Faber Diffraction Model	17
1.5.3	Spin-Disorder Resistivity	18
1.5.4	Kondo Spin-Flip Model	19
1.5.5	Weak Localization and Quantum Interference Effects	20
1.6	Aim and Scope of the Thesis	22
2	Sample preparation and experimental details	25
2.1	Sample Preparation	25
2.1.1	Bulk samples	25
2.1.2	Thin film samples	26
2.2	Experimental set-up and measurements	29
2.2.1	Magnetic measurements	29
2.2.2	Electrical Transport Measurements	32
3	Magnetic phases of Ni-rich NiFeMo and NiFeW alloys	34
3.1	Structural Characterizations	34

3.1.1	X-ray diffraction	34
3.1.2	Energy dispersive X-ray spectroscopy	35
3.2	Magnetic Characterizations	36
3.2.1	DC magnetization	36
3.2.2	AC Susceptibility	41
3.3	Low-temperature Complex Phase of Ni _{83.2} Fe _{3.3} Mo _{13.5} Alloy	43
3.4	Conclusions	50
4	Signature effects of spin clustering in Ni-Fe-Mo and Ni-Fe-W alloys	51
4.1	Introduction	52
4.2	Low-temperature high-field magnetization of the alloys	53
4.3	Intermediate-temperature behaviour	57
4.4	Magnetic phase transition and the associated critical exponents	60
4.5	Conclusion	66
5	Electrical transport properties of a few disordered systems	68
5.1	Introduction	69
5.2	Electrical Resistivity of the Disordered Ni-Fe-V, Ni-Fe-Mo and Ni-Fe-W Alloys	69
5.3	Electrical Resistivity of the Ferromagnetic Amorphous Alloys	81
5.3.1	Low-temperature: $T \ll T_{min}$	84
5.3.2	Intermediate temperature: $\theta_D \gg T > T_{min}$	85
5.3.3	Higher temperature: $T \geq \theta_D$	88
5.4	Electrical Resistivity of PLD-grown Ni-nanocrystalites in TiN matrix	90
5.5	Conclusion	94
6	PLD grown nanometer size Ni-Fe-Mo alloy thin films	97
6.1	Introduction	98
6.2	Thin Film Preparation	98
6.3	Structural Characterizations	99
6.3.1	X- ray Diffraction	99

6.3.2	X-ray Reflectivity	102
6.3.3	Rutherford Backscattering Spectroscopy	109
6.3.4	Atomic Force Microscopy	112
6.3.5	Scanning Electron Microscopy	115
6.3.6	Magnetic Characterization	118
7	Conclusions and Future prospects	126
7.1	Concluding Remarks	126
7.2	Future Directions	130

List of Figures

1.1	Comparison of pure Ni total DOS with partial DOS of Ni in disordered Ni ₉₂ Mo ₈ alloy.	3
1.2	Variation of exchange coupling with the distance between spins of 3d transition metals.	5
2.1	A schematic view of the pulsed laser deposition technique.	27
2.2	The superconducting ring with two junctions.	30
2.3	Sample position in SQUID detection coil and the corresponding signal. . .	32
2.4	Schematic diagrams of QD-PPMS system and the photograph of pucks used for mounting samples.	33
3.1	X-ray diffraction patterns of Ni _{83.1} Fe _{6.0} Mo _{10.9} and Ni _{82.6} Fe _{6.9} W _{10.5} alloys. .	35
3.2	Magnetization (ZFC) vs. temperature for two compositions: (left) Mo10.9 with a lower T _C and (right) Mo5.9 with a higher T _C	37
3.3	Magnetization as a function of temperature for Mo13.5 for both field-cooled and zero field-cooled situations at an applied field of 20 Oe.	37
3.4	Magnetization vs. temperature for three compositions: (left) low Fe content of 3.1 at %, also showing dM/dT vs. T in the inset and (right) higher Fe content of 11.8 and 14.1 at %.	38
3.5	M vs. H are shown for three representative samples of each series: Mo8.9, Mo10.9, and Mo13.5 (left panel) and W8.9, W10.5, and W10.3 (right panel) at 5 K till applied fields of 5 T.	39
3.6	Curie Temperature (T _C) is plotted as a function of Mo and W content in the respective alloy systems.	40
3.7	Temperature variation of real (upper panel) and imaginary (lower panel) parts of ac susceptibility measured at 33 Hz for samples Mo13.5, Mo10.9, W10.3, and W10.5.	41

3.8	Magnetization vs. temperature under FC and ZFC conditions at three different external fields.	44
3.9	Variation of the real part of ac susceptibility with temperature for different frequencies.	45
3.10	Variation of peak temperature (T_g) with frequency of the applied ac field. The solid line is just a guide to the eye.	47
3.11	The hysteresis (magnetization vs. magnetic field) curves for temperatures above and below the spin-glass temperature.	47
3.12	(Top panel) Relaxation of magnetization at different temperatures. (Bottom panel) Double exponential decay at 6 and 10 K.	49
4.1	Magnetisation vs. Temperature plot for four samples are given, among them three samples fit better using Eq. (??) including anharmonic term another one shown fitted to Blochs $T^{3/2}$ law.	54
4.2	Rapid enhancement of the calculated spin-wave parameter B with dilution (upper panel), and (lower panel) nearly $T^{3/2}$ fall-off of site-averaged magnetization and stretching of magnetic order near T_C (from ref. [7]). . .	59
4.3	The modified Arrott-Noakes (AN) plot and X (T) and Y (T) vs. temperature plots for Mo10.9 alloy with values of β and γ for which the best-fitted isotherms are obtained.	61
4.4	χ_0^{-1} vs. $\ln \varepsilon$ plot for W10.3 alloy, $\ln M_s$ vs. $\ln H$ plot for W10.5 alloy, $\ln M_s$ vs. $\ln \varepsilon$ plot for Mo10.9 alloy and $M/ \varepsilon ^\beta$ vs. $H/ \varepsilon ^{\beta\delta}$ plot for W10.3 alloy. .	65
5.1	Resistivity is plotted against temperature from 2 to 300 K at four different applied fields for the $\text{Ni}_{83.1}\text{Fe}_{6.0}\text{Mo}_{10.9}$ alloy. The inset shows the low temperature resistivity minima at different applied fields for the $\text{Ni}_{78}\text{Fe}_4\text{V}_{18}$ alloy.	72
5.2	Zero field resistivity is plotted against temperature from 1.5 to 10 K for $\text{Ni}_{79}\text{Fe}_5\text{V}_{16}$ alloy. The solid line is the best fit of the data found using $\rho(T) = \rho_0 + \rho_{e-e} + \rho_{e-m}$	73
5.3	Zero field resistivity data against temperature have been plotted for (a) $\text{Ni}_{83}\text{Fe}_{10}\text{V}_7$ alloy. The solid lines give the best fit using Eq.(??). The inset inside shows the deviations of the respective fits.	77

- 5.4 Zero field resistivity data against temperature have been plotted for $\text{Ni}_{83.1}\text{Fe}_{6.0}\text{Mo}_{10.9}$ alloy. The solid lines give the best fits (a) using Eq.(??) and (b) using Eq.(??). The insets inside (a), (b) show the deviations of the respective fits. 78
- 5.5 (The normalized resistance r [$R(T)/R(290\text{K})$] is plotted against temperature for all the samples of B-series. The minima look very prominent because the resolution of the resistivity data ($\Delta\rho/\rho$) was better than a few parts per million. 82
- 5.6 (T_{min} and T_C vs. Cr concentration in samples B2, B3, and B4. 84
- 5.7 The conductivity σ vs. temperature data of all the samples of B-series till 10 K along with the fits (solid lines) to Eq. $\sigma(T) \sim \sqrt{T}$ till 5 or 10 K (well below T_{min}). The inset is a plot of the deviations (%) of the data from the best-fitted curves vs. T for sample B3 for both $\ln T$ and \sqrt{T} fits. The curves for samples B5, B3, and B2 are respectively shifted along σ axis by $+1.075 \times 10^5 (\Omega m)^{-1}$, $-0.07 \times 10^5 (\Omega m)^{-1}$, and $+0.01 \times 10^5 (\Omega m)^{-1}$ with respect to B4. 85
- 5.8 The conductivity σ vs. T data for sample B5 along with the best-fitted curves (solid lines) to Eq. $\sigma = \sigma_0 + \beta T^2$. The insets show the same for samples B3 and B2. 87
- 5.9 The conductivity σ vs. temperature data of all the samples of B-series from 200 to 300 K along with the fits (solid lines) to Eq. $\sigma = \sigma_0 - \gamma T - \eta T^2$ for all the samples but without the T^2 term for B4. The curves for samples B5 and B4 are respectively shifted along σ axis by $+1.15 \times 10^5 (\Omega m)^{-1}$ and $-0.04 \times 10^5 (\Omega m)^{-1}$ while B3 and B2 have their true values. 89
- 5.10 (a): A cross-sectional STEM-Z image, (b) its expanded view, (c) high-resolution STEM-Z contrast image of textured Ni nanocrystallites with triangular morphology, and (d) with rectangular morphology, all embedded in TiN matrix.(from ref. [140]) 91
- 5.11 Zero-field resistivity is plotted against temperature from 10 to 300 K. The solid line is the best fit of the data between 60 and 300 K to Eq.(??). The inset shows the temperature dependence of the deviations of the data from the fits to Eqs. (??), with and without the magnetic term, $\rho_m = BT^2$. The average deviations are respectively, 0.006 % and 0.015 %. 92

5.12	Resistivity vs. temperature from 4.2 K till 60 K at fields of 0, 1, 2, and 4 tesla showing minimum at T_{min} , nearly independent of the magnetic field. The minima look very prominent because of the very high resolution of the data.	93
5.13	Fits of $\rho(T)$ data from 4.2 to 25 K (well below T_{min}) and magnetic fields from 0 to 4 tesla to $\rho(T) \sim -\sqrt{T}$. The inset shows similar fits to $\rho(T) \sim -\ln T$. The $(-\sqrt{T})$ fit is far better than the $(-\ln T)$ fit. The values of the normalized χ^2 are smaller by a factor of 13 to 53 for the $(-\sqrt{T})$ fit.	94
6.1	X-ray diffraction pattern for the three different thicknesses of thin films made from $Ni_{83.4}Fe_{10.7}Mo_{5.9}$ alloys along with that of the sapphire substrate.	100
6.2	Schematic illustration (three dimensional view) of X-ray refraction from a uniform thin layer of thickness d on top of a substrate. The amplitude of the incident, reflected, and transmitted waves are respectively, 1, R and T . The bottom panel shows the corresponding one-dimensional variation of the scattering length density (SLD) profile from air to the film and the substrate.	103
6.3	Schematic illustration of the surface or interface roughness.	104
6.4	Schematic representation of the effective three-layer model to fit the reflectivity profiles.	105
6.5	Reflectivity data (left panel) of samples of three thicknesses of $Ni_{83.2}Fe_{3.3}Mo_{13.5}$ films, the solid lines being the best-fitted curves using the tri-layer model. The scattering length density (SLD) of the structure as a function of thickness (right panel) for the same thin films.	106
6.6	Instead of normal incidence, the ion beam is incident at an angle α	110
6.7	RBS spectra for three different thicknesses of $Ni_{83.1}Fe_{6.0}Mo_{10.9}$ alloy (thickness ~ 6 nm, 16 nm, and 22 nm respectively) on Al_2O_3 substrate, recorded with a 2 MeV He^{2+} ion beam.	111
6.8	AFM images of 10 min, 20 min, and 30 min (top to bottom) films of $Ni_{80.4}Fe_{12.9}Mo_{6.7}$ alloy with a scan area of $1 \mu m \times 1 \mu m$. The r. m. s roughnesses are 2.60 nm, 3.51 nm, and 5.06 nm for 10 min, 20 min and 30 min films, respectively.	113
6.9	Grain size distribution of three different thicknesses of $Ni_{80.4}Fe_{12.9}Mo_{6.7}$ alloy films.	114

- 6.10 Scanning electron micrograph, analyzed at a resolution of 11.5 nm with 10000 X magnification, of 30 min film of $\text{Ni}_{83.4}\text{Fe}_{10.7}\text{Mo}_{5.9}$ (left) and the energy dispersive spectrum (right) measured for that particulate shown on the left. 116
- 6.11 Scanning electron micrograph of the 30 min thin film of $\text{Ni}_{83.4}\text{Fe}_{10.7}\text{Mo}_{5.9}$ alloy. The background gives the planer view while the top left inset is the cross-sectional view with platinum capping layer. The thickness of the sample is 36 nm marked in both the cross-sectional images. 117
- 6.12 Zero-field-cooled (ZFC) and field-cooled (FC) M (T) curves for the three thicknesses of the alloy $\text{Ni}_{83.2}\text{Fe}_{3.3}\text{Mo}_{13.5}$. The applied magnetic field is 200 Oe for the 10 min sample and 100 Oe for the two others. 119
- 6.13 Magnetization vs. temperature of the thickest film of $\text{Ni}_{83.2}\text{Fe}_{3.3}\text{Mo}_{13.5}$ alloy where the red curve gives the best to Blochs $T^{3/2}$ law. The spin wave stiffness constant $D = 157 \text{ meV } \text{Å}^2$ 121
- 6.14 Magnetization vs. applied magnetic field at different temperatures for the thickest film of $\text{Ni}_{83.1}\text{Fe}_{6.0}\text{Mo}_{10.9}$ alloy (top panel). H_C and M_r/M_S as functions of temperature are plotted for all the three thicknesses of $\text{Ni}_{83.2}\text{Fe}_{3.3}\text{Mo}_{13.5}$ alloy (bottom panel). 122

List of Tables

3.1	Alloy composition, lattice parameter (a), saturation magnetisation (M_S), Curie temperature (T_C), and spin-glass transition temperature (T_g).	36
3.2	Fitted relaxation time parameters ($\tau_1 < \tau_2$) for the double exponential decay of magnetization at 6 and 10 K.	48
4.1	Magnetization vs. temperature data are fitted to Eq. (??) and the coefficients B , C along with normalized χ^2 , R^2 , T_C , and D are tabulated below.	55
4.2	Alloy compositions, values of T_C and critical exponents, obtained both experimentally and from KF analysis along with those for pure Ni and those from existing theories.	63
4.3	The critical amplitudes of the alloys and those of Ni for comparison.	64
5.1	Alloy compositions, value of T_C , value of T_{min} at different applied fields and depth of minima ($DOM = [\rho(2K) - \rho(T_{min})] / \rho(T_{min})$) at 0 T and $\Delta\rho / \rho_{300}$ ($\Delta\rho = \rho_{300} - \rho(T_{min})$).	71
5.2	Alloy compositions, values of ρ_0 , B , C , m_σ ($m_\sigma = C / \rho_0^2$), R^2 , and normalized χ^2 found from the fit of the data till 10 K using $\rho(T) = \rho_0 + \rho_{e-e} + \rho_{e-m}$.	75
5.3	Alloy compositions, values of A , Θ_D , B , C , R^2 , and normalized χ^2 found from the fits to Eq.(??) or Eq.(??)	79
5.4	Sample ID, T_C , T_{min} , fitting range, fitting equations and parameters, normalized χ^2 , and R^2 for the region well below T_{min} .	83
5.5	Sample ID, fitting range, fitting equations and parameters, normalized χ^2 , and R^2 for the region well above T_{min} but much below T_C .	86
5.6	Sample ID, fitting range, fitting equations and parameters, normalized χ^2 , and R^2 for the region $T \geq \theta_D$ but below T_C .	88

- 6.1 Target composition, deposition time, 2θ corresponding to the (111) plane of the alloy, inter-planer distance d , lattice constant a , the integral breadth of reflection β , volume weighted crystallite size D , and ε_{str} 101
- 6.2 Target composition, deposition time, thickness d , density ρ , and r.m.s roughness σ of three layers determined using Parratts fitting. 108
- 6.3 Target composition, their T_C , M_S , film deposition time, M_S at 10, 100, 200, and 300 K and $\Delta M/M(\%) = [M(10) - M(300)] \times 100/M(10)$ 123

Chapter 1

Introduction

One of the most revisited topics of condensed matter physics, both theoretically and experimentally is disordered systems because of their fascinating physical properties. Disorder in such systems is of different kinds. We shall discuss a few of them in this thesis.

- Amorphous alloys have received considerable attention because of their technological applications and the wide variety of rich physical phenomena they offer. The atomic structure of amorphous alloys is characterized by structurally disordered networks. Structural disorder, in turn, leads to changes in electronic and magnetic properties as compared to those of their crystalline counterparts where lattice periodicity plays important roles in determining these basic properties.
- Alloys with an underlying regular lattice, but the sites are randomly occupied by different constituent atoms, form the second category. This kind of disorder is called substitutional disorder. These alloys are often prepared by arc/induction melting followed by annealing the solid ingots near the melting point of the alloy and finally quenching them to preserve the high temperature random arrangement of atoms.
- Chemical disorder, inherent in substitutional or structural disorder, results in a distribution of magnetic moments and exchange interactions. This affects the magnetic and transport properties of the alloys. The random electrostatic fields due to random atomic arrangements create local anisotropies via spin-orbit coupling, giving rise to a variation in the orientation of magnetic moments. This leads to magnetic disorder. Such disorder is found to introduce new non-collinear spin structures. The exis-

tence of positive and negative exchange interactions leads to spin-glass behaviour in many amorphous and substitutionally random alloys. Transport properties of such systems also differ considerably from the corresponding ordered alloys.

- New age technology insists on size reduction which enhances the application potential due to increased portability. Magnetic thin films and nanoparticles have attracted serious attention because of their use in memory devices. These thin films and nanoparticles are also a class of disordered systems. The disorder in these systems arises from the size distribution of the nanoparticles and different structural disorders originating from impurity atoms, strain due to lattice mismatch with the substrate, surface morphology and roughness, etc. Such disorder in thin films and nanoparticles leads to substantially different magnetic and electrical transport properties as compared to their bulk counterparts.

Our focus will be on magnetism in disordered systems.

1.1 Effects of Disorder on Magnetic Properties

The basic requirements for magnetic order in a solid are (i) the existence of magnetic moments associated with unpaired electrons on atoms or ions in a solid and (ii) an interaction which couples these microscopic moments. These requirements are sufficient for a vast majority of metallic and insulating magnetic materials whose magnetic moments are localized on the atomic sites. However, these concepts do not hold for certain class of materials known as itinerant magnetic systems in which magnetic electrons are itinerant and magnetic moments arise from the exchange splitting of spin-polarized d -bands. In the latter case, the density of states (DOS) at the Fermi level, $n(E_F)$, plays a crucial role in deciding the type of magnetic order. A few important effects of disorder on electronic and magnetic properties are discussed below.

1.1.1 Density of States

In ordered systems, lattice translational symmetry of the effective Kohn-Sham potential seen by the valence electrons leads to the Bloch's theorem. This theorem predicts the

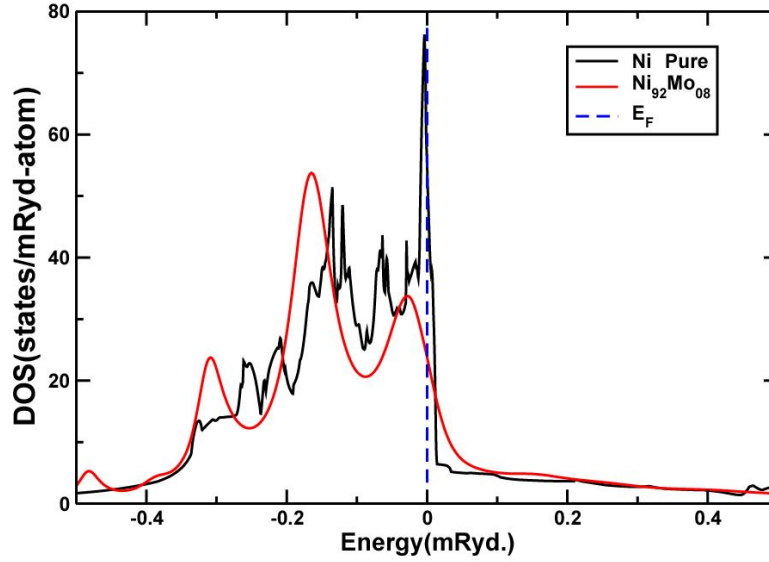


Figure 1.1: Comparison of pure Ni total DOS with partial DOS of Ni in disordered $\text{Ni}_{92}\text{Mo}_8$ alloy.

existence of Van Hove singularities in the electronic structure, resulting in fine structures in the DOS. However in disordered systems Bloch's theorem is violated. The random fluctuations in the potential about the crystalline order leads to scattering of Bloch states. Scattering induced self-energy washes out fine structures in the configuration averaged DOS. As an example, the total DOS of Pure Ni and the partial DOS of Ni in the disordered $\text{Ni}_{92}\text{Mo}_8$ binary alloy are shown in Fig.1.1. Both the DOS curves are of two broad peak-structure resulting from the splitting of the quasi atomic-like electronic energy levels into bonding and anti-bonding bands. The shape and width of electronic bands, from which DOS curves are computed, are basically controlled by the overlap of electronic wave functions on the neighbouring sites (which, in turn, depends on the inter-atomic spacing). In ordered solids the bands are sharp because the Bloch label \vec{k} is a good quantum number. In disordered solids, disorder scattering makes \vec{k} complex leading to a smearing of the bands. Since the nearest-neighbour (NN) atomic configurations in the disordered system resemble that of their nearest ordered counterparts and the average NN

distance is close to that of the corresponding ordered system, the predominant effect of disorder is to smear out the sharp features of the DOS curve and the consequent change in $n(E_F)$ depends on the degree of disorder. In the present example of $\text{Ni}_{92}\text{Mo}_8$, we can see a rather large change in the DOS of Ni at E_F in the presence of Mo.

1.1.2 Magnetic Moments

Unpaired electrons of an atom give rise to a magnetic moment and the persistence of such a moment in ions or solids, or even in metals, depends on the degree of overlap of the wave functions of electrons in different shells on neighbouring ions/atoms. For example, considerable overlap of valence electron wave functions on neighbouring ions, particularly in a metal, leads to a spread of atomic levels into energy bands of delocalized states. The overlap of the d -shell electron wave functions for neighbouring ions in a metal is weak and hence d -band is much narrower than s -band in transition metal-based alloys. In metals, (particularly in transition metals) the delocalized s electrons complicate the situation since they are not only an extra source of itinerant magnetic moments (leading to Pauli paramagnetism) but also their hybridization with the magnetic d electrons renders the atomic concept of fixed local moments meaningless. The appropriate theoretical framework for the transition metals is provided by the Stoner band model in which the energy states of the itinerant magnetic electrons on a given ion are split into spin-up and spin-down bands due to the exchange interaction. In this model, the magnetic moment is proportional to the population difference in the spin-up and spin-down d sub-bands. In disordered systems, the fluctuation in nearest neighbour (NN) distance and the degree of overlap of electronic wave functions on neighbouring sites as well as exchange splitting change from site to site giving rise to variation in local moments.

1.1.3 Interaction Between Moments

The magnetically ordered structure, like a ferromagnet, builds up due to the interactions coupling the magnetic moments. The classical dipolar interaction of the form [1]

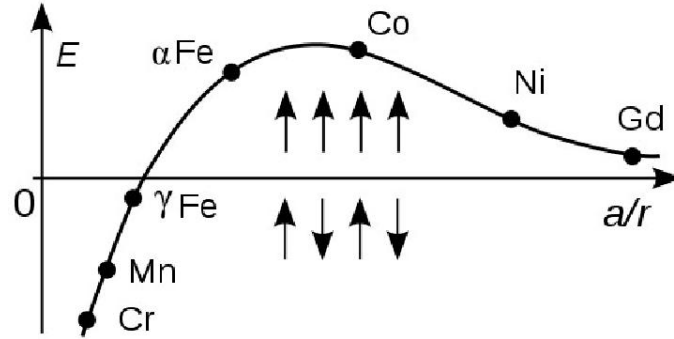


Figure 1.2: Variation of exchange coupling with the distance between spins of 3d transition metals.

$$\mathcal{H}_{ij}^d = \frac{\vec{\mu}_i \cdot \vec{\mu}_j}{r_{ij}^3} - \frac{3(\vec{\mu}_i \cdot \vec{r}_{ij})(\vec{\mu}_j \cdot \vec{r}_{ij})}{r_{ij}^5} \quad (1.1)$$

tends to align the moments μ_i and μ_j parallel to the line joining the sites i and j . Dipolar interactions are weak, long-ranged, and anisotropic since they depend on the orientation of the moments relative to r_{ij} . The net dipolar field is identically zero at sites in a lattice with cubic symmetry. However, in disordered systems, it may have distribution in both magnitude and direction. The quantum mechanical exchange interaction is much stronger. The exchange interaction is an effective electrostatic interaction between two electrons which depends on the relative orientation of their spins. This isotropic Heisenberg interaction is given by [1]

$$\mathcal{H}_{ij}^{ex} = -2J_{ij}\vec{S}_i \cdot \vec{S}_j, \quad (1.2)$$

where J_{ij} is the exchange coupling constant between spins at sites i and j . J_{ij} is positive for ferromagnetic coupling and negative for anti-ferromagnetic coupling.

The Bethe-Slater curve [2] shown in Fig. 1.2 indicates roughly how the exchange constant varies with distance between magnetic shells in 3d transition metals. It is clear from Fig. 1.2 that the inter-atomic separations in disordered systems lead to a distribution of exchange interaction which may sometimes include interactions of either sign. Apart from direct exchange, there are a few other exchange mechanisms like superexchange via

ligands and indirect exchange via conduction electrons also known as the Ruderman-Kittel-Kasuya-Yosida (RKKY) interaction, which can be written as

$$J(r) = -\frac{J_0 \cos(2k_F r)}{(2k_F r)^3} \quad (1.3)$$

where k_F is Fermi wave vector. This interaction, $J(r)$, is oscillatory in nature, i.e., it becomes positive and negative depending on the separation between the spins/moments. A distribution in the inter-atomic separations gives rise to a distribution of indirect exchange also. For instance, superexchange is negative for 180° metal-ligand-metal bonds and weakly positive for 90° bond angles [1]. The RKKY interaction arises when the magnetic electrons of one atom induce a spin polarization in the conduction electrons which overlaps another atom and affects its magnetic electrons. The long-range and oscillatory nature of RKKY interaction is not only responsible for the spin-glass behaviour in many dilute magnetic alloys but also leads to helical spin structure in many crystalline rare earth metals and compounds.

1.1.4 Magnetic Anisotropy

Exchange energy depends strongly on the details of the physical interaction between orbitals in neighboring atoms with respect to one another; hence changing the positions of these atoms will affect that interaction. In other words, strain on a crystal will alter its magnetic behavior. Similarly, changes in the magnetization can change the shape of the crystal by altering the shapes of the orbitals. This is known as magnetostriction. The local magnetic anisotropy that results from spin-orbit interaction or the anisotropy of local crystal field has strong influence on the nature of magnetic order in the ground state and coercivity of disordered magnetic materials [3]. Magnetic thin films are often found to behave diversely due to the magnetic anisotropy created by the structural disorder.

1.2 Magnetic Order in Disordered Systems

A wide variety of magnetic order [4–6] exists in disordered systems in the presence of various kinds of disorder. The most commonly known among them are ferromagnetism,

paramagnetism, diamagnetism, ferrimagnetism, and antiferromagnetism. Except diamagnetism, all other magnetic properties can be understood classically by the molecular field theories. Some more possible magnetic ordering/states in disordered systems apart from conventional ferromagnetic and antiferromagnetic orderings are spin-glass, cluster-glass, re-entrant spin-glass, etc. A few atomic percent of magnetic impurity in noble metal host or vice versa can give rise to a new magnetic phase known as spin glass, where randomness invokes a competition between the impurity spins/moments when it comes to ordering. Below some characteristic temperatures, known as spin-freezing/glass transition temperature (T_g), these spins are found to be frozen or locked in random orientations and hence the name spin-glass (SG) state. Several arrangements are possible where different sets of spin-disordered states with equivalent energy, give rise to frustration [7]. Randomness and frustration are two most basic prerequisites for the formation of a spin-glass phase. The interaction between the spins in this phase is of RKKY type [Eq.1.3] and the coupling $J(r)$ is ferromagnetic or antiferromagnetic depending on the separation between the spins. The direct interaction, however, is negligibly small. Some of the most exciting experimental features of spin glasses are sharp peaks in ac-susceptibility [8–10] at T_g , hysteresis and remanence in dc-magnetization below T_g [11–13], time-decay of remanent magnetization [14], rounded peak in Hall resistivity near T_g [15, 16], knee in molar heat capacity at T_g [17], etc. Not only the experimental work but also there was an explosion of theoretical activities to explain the numerous behaviour of the spin-glass phase. Properties and the associated phenomena exhibited by spin glass systems have formed the subject of several books and review articles [8], [18–27]. Now if we increase the probability of impurity atoms to come closer and have each other as nearest or next nearest neighbour by increasing impurity concentration than in spin glass, a new phase is formed, known as cluster glass. Unlike the spin glass the probability of direct exchange is increased, depending on the nature of the impurity and the neighbouring position, the short-range intra-cluster interaction can be both ferro- as in $\text{Au}_{100-x}\text{Fe}_x$ ($16 \leq x \leq 24$) [28] as well as antiferromagnetic as in $\text{Cu}_{100-x}\text{Mn}_x$ ($72 \leq x \leq 84$) [29]. However, the inter cluster interaction will remain of RKKY type. Hence, cluster moments are randomized in the long range. In cluster glass, values of magnetization and saturation remanence are enhanced compared to those in dilute spin-glass alloys. Further increase in the impu-

rity concentration results in formation of impurity clusters where the interactions are a combination of RKKY as well as direct exchange interactions. In this kind of situation, a new magnetic phase emerges, where both long range and spin-glass ordering coexist. This is known as re-entrant spin glass (RSG). As temperature is reduced, a disordered state arises from a comparatively more ordered state. Putting it other way, a long-range magnetic order breaks up into a large number of randomly frozen clusters at low temperatures. The re-entrant spin glass is usually found in concentrated crystalline as well as in amorphous alloys. Some of the examples are $\text{Au}_{100-x}\text{Fe}_x$ [28], $\text{Cu}_{100-x}\text{Mn}_x$ [29], $\text{Fe}_{80-x}\text{Ni}_x\text{Cr}_{20}$ [30, 31], $\text{Ni}_{80-x}\text{Fe}_x\text{Cr}_{20}$ [31], $\text{Ni}_{100-x}\text{Mn}_x$ [32], $(\text{Fe}_{100-x}\text{Ni}_{100-x})_{80}\text{P}_{14}\text{B}_6$ [33], $(\text{Fe}_x\text{Ni}_{100-x})_{79}\text{Si}_9\text{B}_6$ [34], etc.

1.3 Low-lying Magnetic Excitations

Having briefly described the types of ground state (i.e., at $T = 0$ K) magnetic order prevalent in spin systems with disorder in the previous section, this section is devoted to the changes in the magnetic order (i.e., magnetic excitations) brought about by increasing temperature in disordered systems. In a crystalline ferromagnet, the local deviation from the perfect alignment does not remain confined to a microscopic region of space but propagates like a wave due to exchange coupling between the spins. These low-lying magnetic excitations are called spin waves. A spin wave can be thought of as one spin reversal coherently spread over the entire crystal. All the conventional spin-wave theories are based on localized-electron picture in which the magnetic electrons are localized on atomic orbitals. However, in metallic systems, the magnetic electrons have itinerant character. Thus, localized-electron and itinerant-electron models form two exactly opposite descriptions of the low-lying magnetic excitations.

1.3.1 Localized-electron Model

Felix Bloch [35] was the first to introduce the concept of spin waves in a ferromagnet within the framework of the localized-electron model. The spin waves are thermally excited and their energy is quantized. In analogy with a phonon, which represents the particle associated with a quantized lattice wave, the corresponding particle for a quantized spin

wave is called a magnon. The Hamiltonian that describes the Heisenberg interaction between spins localized at the neighbouring sites i and j is given by [36, 37]

$$\mathcal{H} = -\frac{1}{2} \sum_{ij} J_{ij} \vec{S}_i \cdot \vec{S}_j \quad (1.4)$$

where J_{ij} is the exchange integral. At low temperatures, the spin deviations as well as the fraction of spin reversals are small and the spin waves are independent of one another. Thus, in the linear approximation, the magnon dispersion relation for crystalline ferromagnets in which the direct Heisenberg exchange interaction is confined only to the nearest neighbours, is expressed as [36, 37]

$$E(k) = \hbar\omega_k = 2JSZ(1 - \gamma_k) \quad (1.5)$$

with $\gamma_k = \frac{1}{z} \sum_{\delta} \exp(i\vec{k} \cdot \vec{\delta})$, Z is the coordination number.

In the long-wavelength limit, i.e., $|\vec{k} \cdot \vec{\delta}| \ll 1$, the dispersion relation for a simple cubic lattice with lattice constant a takes the form

$$E(k) = Dk^2 + Ek^4 + \dots \quad (1.6)$$

where the spin wave stiffness coefficient $D = 2JSa^2$ is a measure of the exchange interaction and the coefficient E is related to the average mean square range of exchange interaction $\langle r^2 \rangle$ through the relation $E = -\langle r^2 \rangle D/20$. The spontaneous magnetization, $M(T, 0)$, at any temperature is given by

$$M(T, 0) = g\mu_B \langle S^z \rangle = g\mu_B (NS - \sum_k n_k) = M(0, 0) - g\mu_B \sum_k n_k$$

where $M(0, 0) = g\mu_B NS$ and n_k is the number of spin waves in thermal equilibrium at temperature T given by the Bose-Einstein distribution function. The final expression for $M(T, 0)$ has the form [36]

$$\begin{aligned} \Delta m &= \frac{M(0, 0) - M(T, 0)}{M(0, 0)} \\ &= \frac{g\mu_B}{M(0, 0)} \left[\zeta \left(\frac{3}{2} \right) \left(\frac{k_B T}{4\pi D} \right)^{\frac{3}{2}} + 15\pi\beta\zeta \left(\frac{5}{2} \right) \left(\frac{k_B T}{4\pi D} \right)^{\frac{5}{2}} \right] \end{aligned} \quad (1.7)$$

where $\zeta\left(\frac{3}{2}\right) = 2.612$ and $\zeta\left(\frac{5}{2}\right) = 1.341$ are the Riemann ζ functions and $\beta = \langle r^2 \rangle / 20$. The $T^{3/2}$ and $T^{5/2}$ terms in Eq.1.7 arise from the k^2 and k^4 terms respectively in the dispersion relation (Eq.1.6). The higher order terms of the form k^6 , k^8 , etc. in Eq.1.6, if retained, give rise to additional correction terms [38] to $M(T, 0)$ that are proportional to $T^{7/2}$, $T^{9/2}$, etc. Application of an external magnetic field (or in the presence of any other fields such as dipolar fields, anisotropy fields, etc.) gives rise to an energy gap in the spin-wave spectrum and the dispersion relation gets modified to

$$E(k) = \hbar\omega_k = g\mu_B H_{eff} + Dk^2 + Ek^4 + \dots \quad (1.8)$$

with $H_{eff} = H - 4\pi NM(0, H) + H_A$, where N is the demagnetizing factor, H_A is the anisotropy field and $g\mu_B H_{eff} (= k_B T_g)$ is the energy gap. Consequently, in the presence of magnetic fields, the expression for magnetization also gets modified and takes the form [36]

$$\begin{aligned} \Delta m &= \frac{M(0, H) - M(T, H)}{M(0, H)} \\ &= \frac{g\mu_B}{M(0, H)} \left[z\left(\frac{3}{2}, T_H\right) \left(\frac{k_B T}{4\pi D}\right)^{\frac{3}{2}} + 15\pi\beta z\left(\frac{5}{2}, T_H\right) \left(\frac{k_B T}{4\pi D}\right)^{\frac{5}{2}} \right] \end{aligned} \quad (1.9)$$

where the Bose-Einstein integral functions

$$z(s, T_H) = \zeta(s)F(s, T_H) = \sum_{n=1}^{\infty} n^{-s} \exp(-nT_H) \quad (1.10)$$

with $T_H = g\mu_B H_{eff} / k_B T$ allows the energy gap in the spin-wave spectrum. The spin-wave theory discussed so far assumes that the thermally excited spin waves, propagate independent of each other so that the superposition of spin waves remains a valid approximation. However, with increasing temperature, the interaction between spin waves becomes important and these interactions have to be considered carefully. Spin-wave interactions are mainly of two types: kinematic interaction and dynamic interaction [36,38]. The kinematic interaction arises due to the fact that the maximum number of spin deviations that can occur at any site carrying a spin S is $2S$. For example, if $S = 1/2$, two spin deviations cannot reside at the same site and the kinematic interaction, which prevents this situation, is repulsive in this case. The dynamic interaction arises because it costs less energy for a spin to undergo a deviation if the neighbouring spins have already

undergone such deviations. This dynamic interaction is attractive in nature. An analysis of the magnon-magnon interactions in the Heisenberg ferromagnets, due to Dyson [38], has demonstrated that at low temperatures, the kinematic interactions are negligibly small and the dynamic magnon-magnon interactions lead to a thermal renormalization of spin-wave energies [36,38], i.e.,

$$\hbar\omega_k = g\mu_B H_{eff} + D(T)k^2 + \dots \quad (1.11)$$

with

$$D(T) = D_0 (1 - D_{5/2} T^{5/2}) \quad (1.12a)$$

and

$$D_{5/2} = \pi \langle r^2 \rangle \left(\frac{g\mu_B}{M(0,0)} \right) \left(\frac{k_B}{4\pi D(0)} \right)^{5/2} \zeta \left(\frac{5}{2} \right) \quad (1.12b)$$

Moreover, the dynamic interaction gives rise to a T^4 correction [38] to $M(T,0)$. In addition to the direct Heisenberg exchange interactions between the spins on the neighbouring d shells, the d spins in the localized model interact indirectly with one another via the conduction electron s spins. This magnon-electron interaction also renormalizes the spin wave stiffness coefficient $D(T)$ according to the expression [39].

$$D(T) = D(0)(1 - D_2 T^2) \quad (1.12c)$$

However, the contribution to $D(T)$ arising from the T^2 term in Eq.(1.12c) is several orders of magnitude smaller than that due to the $T^{5/2}$ term in Eq.(1.12c) since the $s-d$ interaction is very weak compared to the direct $d-d$ interaction. Hence, for all practical purposes the spin-wave stiffness renormalizes according to Eq.(1.12c) in the localized-electron model.

1.3.2 Itinerant-electron Model

The itinerant-electron model for magnetism, first proposed by Bloch [40] in connection with the paramagnetism of an electron gas, was later developed by Slater [41] and Stoner [42] to explain the magnetic properties such as non-integral values of saturation magnetization per atom at 0 K, large coefficients of T term in low-temperature specific

heat, etc. which could not be explained in terms of the localized-electron model. The itinerant-electron model is based on the band theory of electrons in solids and regards magnetic carriers as itinerant or Bloch electrons. The interaction between Bloch electrons splits d - band into spin-up (\uparrow) and spin-down (\downarrow) sub-bands and hence gives rise to ferromagnetism. Wohlfarth, Edwards, and coworkers [43–45], while applying the Stoner theory to many ferromagnetic metals, made suitable refinements so as to make it more realistic. However, the basic ideas of Stoner theory remained the same.

Existence of spin waves could not be originally envisaged in the band model until Herring and Kittel [46] have shown spin waves in their phenomenological theory. In the band model, the collective excitations of particles with a spin reversal, but without a change in wave-vector k , are spin waves of wave-vector k whereas the individual spin-flip excitations with or without a change in wave-vector are the single-particle excitations. The spin-wave dispersion relation in the long-wavelength limit, calculated within the framework of the itinerant-electron model [39, 46, 47], has the same form as that in the localized-electron model. However, at finite temperatures, the magnon - magnon interactions and magnon - single particle interactions become important. The effect of these interactions within the itinerant-electron model is to renormalize the spin-wave energy through the renormalization of spin-wave stiffness coefficient according to the relation [39, 46, 47]

$$D(T) = D(0)(1 - D_2 T^2 + D_{5/2} T^{5/2}) \quad (1.13)$$

where the parameter $D(0)$ is the value of $D(T)$ at 0 K and it depends on the exchange splitting of spin \uparrow and spin \downarrow sub-bands and on the dispersion relation of the single-particle energies. The dominant T^2 term in Eq.(1.13) arises from magnon-single-particle interactions whereas the $T^{5/2}$ term originates from the magnon-magnon interactions and is much smaller compared to the T^2 term. Hence the $T^{5/2}$ term in Eq.(1.13) is generally neglected and the $D(T)$ varies as T^2 in the itinerant-electron model in contrast with the $T^{5/2}$ variation of $D(T)$ (Eq.(1.12c)) in the localized-electron model.

1.4 Thermal Critical Phenomenon

In zero external magnetic fields, the ferromagnetic (FM)-to-paramagnetic (PM) phase transition at the critical point, T_C is a second-order phase transition. The spontaneous

magnetization, which is the order parameter in this case, goes continuously to zero at T_C with a critical exponent β . The zero-field susceptibility, magnetic part of specific heat, and the spin-spin correlation length diverge at T_C with the critical exponents γ , α and Δ , respectively. These critical exponents are universal in the sense that they depend only on the lattice dimensionality, d , and the order parameter dimensionality, n , and possess exactly the same values for widely different systems if all of them are described by the same values of d and n [48, 49]. From the scaling arguments and using renormalization group (RG) ideas, the total free energy density, $f(T, H)$, consisting of the singular, $f_{sing}(T, H)$, and non-singular, f_0 , parts, can be written as [50–52]

$$f(T, H) = f_0 - f_{sing}(\varepsilon, H) = f_0(T) - |\varepsilon|^{2-\alpha} F_{\pm}(H/|\varepsilon|^{\Delta}) \quad (1.14)$$

where the prefactor $|\varepsilon|^{2-\alpha}$ in Eq.(1.14) accounts for the shrinkage in volume under the scale transformation which leaves the total free energy invariant, α is the specific heat critical exponent, $\varepsilon = (T - T_C)/T_C$, H is the ordering field, Δ is the gap exponent and the plus and minus signs refer to temperatures above and below T_C . If the macroscopic volume is set equal to unity, i.e., $V = 1$, the physical quantities such as magnetization, susceptibility, and specific heat are straightaway obtained from the field and temperature derivatives of $f(T, H)$. Thus, the zero-field specific heat, $C(T, 0)$, magnetization, $M(T, H)$, and the 'in-field' susceptibility, $\chi(T, H)$, are given by the expression [48–52]

$$C(T, 0) = -T(\partial^2 f / \partial T^2)_{H=0} = (1 - \alpha)(2 - \alpha)T_C^{-1} F_{\pm}(0) |\varepsilon|^{\alpha} (1 + f) \quad (1.15)$$

$$M(T, H) = -(\partial f / \partial H)_T M(\varepsilon, H) = |\varepsilon|^{\beta} f_{\pm}(H/|\varepsilon|^{\Delta}) \quad (1.16)$$

$$\chi(T, H) = \partial M(T, H) / \partial H = (|\varepsilon|^{\gamma} \partial f_{\pm}(H/|\varepsilon|^{\Delta}) / \partial H) \quad (1.17)$$

where $\beta = 2 - \alpha - \Delta$, $\gamma = 2 - \alpha - 2\Delta$, and $f_{\pm} = (\partial F_{\pm} / \partial H)_T$. The zero-field quantities such as spontaneous magnetization, $M(T, 0)$ and the zero-field susceptibility $\chi(T, 0)$, are then obtained by taking the limit $H \rightarrow 0$ and expanding $f_{\pm}(H/|\varepsilon|^{\Delta})$ in Taylor series around $H = 0$ as

$$f_{\pm}(H/|\varepsilon|^{\Delta}) \simeq f_{\pm}(0) + (H/|\varepsilon|^{\Delta}) f'_{\pm} + \dots \quad (1.18)$$

Hence one gets

$$M(T, 0) = M_0 |\varepsilon|^{\beta} \quad \varepsilon < 0 \quad (1.19a)$$

$$C(T, 0) = (M_0 / H_0) |\varepsilon|^{-\gamma} \quad \varepsilon > 0 \quad (1.19b)$$

where $M_0 = f_{\pm}(0)$ and $M_0/H_0 = f'_{\pm}(0)$ are the asymptotic amplitudes for spontaneous magnetization and initial susceptibility, respectively. As $\varepsilon \rightarrow 0$, $|\varepsilon|^{\Delta}/H \rightarrow 0$ and the scaling equation of state (SES) represented by Eq. (1.16) can be rewritten in a more convenient form [52], i.e.,

$$M(\varepsilon, H) = H^{(\beta/\Delta)} f_0(|\varepsilon|/H^{1/\Delta})$$

where f_0 is analytic at $|\varepsilon| = 0$ and can be directly related to f_- and f_+ . In the limit $(|\varepsilon|/H^{1/\Delta}) \rightarrow 0$, the function $f_0(z)$ can be expanded in Taylor series around $z = 0$ with the result

$$M(\varepsilon, H) = H^{\beta/\Delta} [f_0(0) + (|\varepsilon|/H^{1/\Delta}) f'_0(0) + \dots]$$

Thus, the critical M versus H isotherm at $|\varepsilon| = 0$ is described by the expression

$$M(0, H) = f_0(0) H^{1/\delta} \quad (1.20a)$$

or

$$H = D M^{\delta} \quad (1.20b)$$

with $\Delta = \beta\delta$ and $D = f_0^{-\delta}$. Furthermore, at $|\varepsilon| = 0$ and in the absence of external magnetic fields ($H=0$), the spin-spin correlation function, defined as $G(r) = \langle (S(r) - \langle S \rangle)(S(0) - \langle S \rangle) \rangle$, varies with distance r as [48, 49, 51, 53]

$$G(r) = N |T|^{-(d-2+\eta)} \quad \text{large } |r|; \quad \varepsilon = H = 0 \quad (1.21a)$$

where d is the dimensionality, η is the correlation function critical exponent, while the spin-spin correlation length, related to $G(r)$ through the expression $G(r) = \exp(-|r|/\xi(T))/|r|$ as $r \rightarrow \infty$, varies in the critical region as [48, 49, 51, 53]

$$\xi(T) = \xi(T)_0^{\mp} |\varepsilon|^{\nu^{\mp}} \quad (1.21b)$$

Note that in all the foregoing equations H denotes the field that is obtained by correcting the external magnetic field for the demagnetizing field.

It is customary to determine the critical exponents β and γ from the bulk magnetization data taken in external magnetic fields by using a specialized form of the general scaling equation of state, Eq. (1.14), proposed by Arrott and Noakes [54], i.e.,

$$(H/M)^{1/\gamma} = a\varepsilon + bM^{1/\beta} \quad (1.22)$$

where the coefficients ‘a’ and ‘b’ are temperature-independent. According to the Arrott-Noakes SES (Eq.(1.20)), the $M(T,H)$ data taken in the critical region, when plotted in the form of $M^{1/\beta}$ vs. $(H/M)^{1/\gamma}$ (known as the modified Arrott plot) isotherms with the proper choice [53] of β and γ , fall on a set of parallel straight-line isotherms (especially in the high-field region) with the critical isotherm at T_C passing through the origin. The high-field linear portions of these isotherms when extrapolated to $H \rightarrow 0$ yield intercepts on the ordinate and abscissa from which $M(T,0)$ and $\chi(T,0)$ are computed. The $M(T,0)$ and $\chi(T,0)$ data so obtained are analyzed in terms of Eqs.(1.19a) and (1.19b). The “zero-field” quantities such as $C(T,0)$, $M(T,0)$, and $\chi(T, 0)$, when analyzed in terms of single power law expressions (1.15), (1.19a), and (1.19b) yield only the average values for the exponents since these expressions are strictly valid for temperatures in the close proximity to T_C whereas the experimental data for such quantities are generally taken over a wide temperature range in the critical region. The exponents obtained in this way not only depend on the temperature range used but also could significantly differ from the true asymptotic values [52, 53, 71]. The expressions for the quantities $C(T,0)$, $M(T,0)$, and $\chi(T,0)$ must, therefore, include both analytic and non-analytic “correction-to-scaling” (CTS) terms [49–52, 56, 71] arising from the nonlinear relevant and irrelevant scaling fields, respectively.

1.5 Electrical Transport in Disordered Alloys

Detailed investigations of transport properties of solids provide valuable information about the electronic structure and various scattering processes that are responsible for the electronic transport. Disordered systems show a spectrum of anomalies in their electronic behaviour. In disordered systems the random incoherent scattering of conduction electrons by the impurities and defects is the origin of high resistivity. In 3d transition metals and alloys, the 3d bands are much narrower in energy compared to the s and the p bands;

as a result, the density of states of 3d electrons is much higher than those of the s and p conduction electrons. Hence the conduction electrons will have much higher velocity than the d electrons. As a result, the comparatively static d electrons act as additional source of scattering for the conduction electrons giving rise to various anomalies in the electrical resistivity. The interpretation of electrical resistivity in 3d metals and alloys is quite difficult and rather controversial. A few salient features of the resistivity data taken for a large number of disordered systems are

- (i) The considerably high residual resistivity (ρ_0) of disordered systems is generally considered as a measure of disorder in any alloy [57].
- (ii) The temperature coefficient of resistivity (TCR) is small [58,59] and usually positive for alloys with $\rho_0 < 150\mu\Omega$ cm and negative for alloys with $\rho_0 > 150\mu\Omega$ cm, known as the Mooij correlation [60].
- (iii) In a number of alloys, resistivity as a function of temperature goes through a minimum at a temperature T_{\min} and resistivity saturates at high temperatures at a value $\sim 150\mu\Omega$ cm.

A number of theoretical models have been proposed to explain the resistivity minimum, and the corresponding low-temperature resistivity anomaly and other characteristic features of resistivity behaviour in disordered materials, but none of these models, on its own, can describe the variation of resistivity in the entire temperature range. Matthiessen's rule which states that the contributions to total resistivity of a solid arising from different scattering mechanisms are additive, is also considered to be valid in disordered materials. Therefore, one needs to take into account of all possible known scattering mechanisms to explain the observed resistivity behaviour as a function of temperature, magnetic field, etc.

1.5.1 Electron Phonon Scattering

In crystalline solids, one of the major contributions to resistivity comes from the scattering of conduction electrons by lattice vibrations (i.e., phonons). Long back, a single band

phonon scattering using the Bloch theory [61] was proposed where ρ_{phonon} is given by

$$\rho_{phonon} = A \left(\frac{T}{\Theta_D} \right)^5 \int_0^{\Theta_D/T} \frac{z^5 dz}{(e^z - 1)(1 - e^{-z})}, \quad (1.23)$$

where A is a constant and θ_D is the Debye temperature. This is known as the Bloch - Grüneisen relation.

In transition metals and alloys, Mott [62] had first proposed that s-d transition has to be incorporated in the electron - phonon scattering. For transition metals and alloys, the current is carried by nearly free s electrons which are scattered by the lattice phonons into the vacant states above the Fermi level in the d-band, resulting in high resistivity. Later Wilson [63] had included s-d transition in calculating the phonon contribution for 3d metals and their alloys. This is known as Bloch - Wilson relation, which is written as

$$\rho_l = A \left(\frac{T}{\Theta_D} \right)^3 \int_0^{\Theta_D/T} \frac{z^3 dz}{(e^z - 1)(1 - e^{-z})}. \quad (1.24)$$

This expression takes in account phonon contribution to the resistivity for the whole range of temperatures.

1.5.2 Ziman-Faber Diffraction Model

This model considers the effect of scattering of conduction electrons from the potential of a disordered lattice. Originally proposed by Ziman [64] for simple liquid metals, this theory is based on the following assumptions [58, 59, 64, 65] :

- (a) The electronic transport properties can be described by the Boltzmann transport equation.
- (b) The interaction between the conduction electrons and ions can be described by a pseudo potential.
- (c) The conduction electrons are assumed to be nearly free (i.e , $k_F \cdot l \ll 1$, k_F is the Fermi wave vector, l is the electron mean free path) and the scattering potential is weak enough to be treated by first-order perturbation theory (Born approximation is valid).

Evans et al. [66] extended the Ziman theory to include liquid transition metals in the transport properties of metallic glasses by using the muffin-tin potential and arrived at the following expression for resistivity [58, 59, 66–68]

$$\rho = \frac{30\pi^3\hbar^3}{me^2k_F^2E_F\Omega} \sin^2[\eta(E_F)]S_T(2k_F) \quad (1.25)$$

where k_F and E_F are the Fermi wave vector and Fermi energy, respectively. Ω is the atomic volume, $\eta(E_F)$ is the d partial-wave phase shift describing the scattering of the conduction electrons by the ion-cores which carry a muffin-tin potential centered around each ion position and $S_T(2k_F)$ is the structure factor at $k = 2k_F$. The temperature dependence of ρ comes from the temperature dependence of $S_T(2k_F)$. The temperature dependence of the structural factor $S_T(k_F)$ goes as

$$S(k_F) = \int_{-\infty}^{\infty} S(q, \omega) z(e^z - 1)^{-1} d\omega \quad (1.26)$$

where $z = \hbar\omega/k_B T$. At very low temperatures ($T \ll \theta_D$), the structure factor goes as T^2 and at high temperatures ($T \gg \theta_D$) as T [68]. Later, with the introduction of a new idea of ‘phonon-ineffectiveness’ [68, 69], the low temperature T^2 dependence is found as a manifestation of phonon scattering in the disordered state. This is not limited to amorphous alloys only, but it is a feature of disordered alloys.

1.5.3 Spin-Disorder Resistivity

The spin-disorder model, applicable to ferromagnetic materials, deals with the scattering of conduction electrons by spin-waves. The spin-disorder model for amorphous ferromagnets developed by Richter et al. [70], considers a Heisenberg spin system in which spins are localized at the sites of an amorphous network and conduction electrons get scattered from these localized spins (moments) through the s - d exchange interaction. Using the nearly free-electron concept, the magnetic part of resistivity in the spin-wave

approximation is given by [70, 71]

$$\rho_{SD}(T) = \rho_{SD}(0) \left\{ 1 + \frac{\Omega_C}{(2\pi^2)S} \Gamma\left(\frac{3}{2}\right) \xi\left(\frac{3}{2}\right) \left(\frac{k_B T}{D_{SW}}\right)^{3/2} + \frac{1}{J_S(2k_F)} \left[\frac{\pi^2}{3S} \left(\frac{k_B T}{D_{SW}}\right)^2 - F(T) \right] \right\} \quad (1.27)$$

with

$$\rho_{SD}(0) = \frac{2\Omega_C}{3\hbar^3} [\Omega/N_c e] m S J_{sd}]^2 J_S(2k_F) \quad (1.28)$$

where N_c is the number of electrons, Ω_C and Ω are the atomic and sample volumes, respectively, S is the spin of the local atomic magnetic moment, D_{SW} is the spin-wave stiffness coefficient, Γ and ξ are the gamma and Riemann zeta functions, respectively, J_{sd} is the exchange coupling constant and $J_S(2k_F) = \int_0^{2k_F} k^3 S_m(k) dk$; $S_m(k)$ is the static magnetic structure factor. The $T^{3/2}$ term in Eq.(1.27) is the net result of a partial cancellation of two competing $T^{3/2}$ terms; one arising from incoherent (momentum non-conserving) electron-magnon scattering and increasing with increasing temperature, and the other originating from the elastic scattering of conduction electrons from randomly oriented temperature-dependent local moments and decreasing with increasing temperature, whereas the T^2 term in Eq.(1.27) is the coherent electron-magnon scattering term. The function $F(T)$, arising because of structural disorder, constitutes only a minute correction to the T^2 term indicating thereby that the coherent electron-magnon scattering is not significantly altered by the presence of quenched disorder. $\rho_{SD}(0)$ and the $T^{3/2}$ term both go to zero for crystalline ferromagnets but possess finite values in the case of amorphous ferromagnets. In addition, the coefficient of the $T^{3/2}$ term in amorphous magnets is expected to be roughly two orders of magnitude [99] larger than that of the T^2 term. Thus, the spin-disorder model predicts that at low temperatures, $\rho_{SD}(T)$ should vary as T^2 in crystalline systems in contrast with the $T^{3/2}$ variation in amorphous ferromagnets [70, 71].

1.5.4 Kondo Spin-Flip Model

This model was originally conceived by Kondo [72] to explain the resistivity minimum in dilute crystalline alloys consisting of a non-magnetic host containing a few ppm of

magnetic impurities. The scattering of conduction electrons of the host from the localized spin of local magnetic impurities gives rise to spin-dependent increase in the resistivity at low temperatures, which in combination with the contribution to resistivity arising from the usual electron-phonon scattering at high temperatures produces a minimum in the total resistivity of these alloys [72]. Using the perturbation theory in the second Born-approximation, Kondo calculated the spin-dependent part of resistivity with the result [61, 72]

$$\rho_K(T) = \rho_M[1 + Jc \ln(T/T_K)] \quad (1.29)$$

where c is the magnetic impurity concentration, J is the local exchange and T_K is the Kondo temperature defined as $k_F T_K = D \exp[2/3JN(0)]$, where D is the conduction band width, $N(0)$ is the DOS of conduction electrons. When J is negative, the resistivity increases at low temperatures giving rise to a negative TCR. The unphysical logarithmic divergence in the original expression for $\rho_K(T)$, Eq.(1.29), was later removed by introducing the concept of spin compensation which asserts that the effective local moment decreases with decreasing temperature and finally vanishes at $T \rightarrow 0$ K. Taking this aspect into account, Hamann [73] obtained a modified expression for the Kondo contribution to resistivity as

$$\Delta\rho/\rho(0) = 1 - \frac{\ln(T/T_K)}{[\ln^2(T/T_K)S(S+1)\pi^2]^{1/2}}. \quad (1.30)$$

The above expression ensures that the resistivity saturates at a finite value at low temperatures. Although the Kondo model is strictly applicable to dilute crystalline materials only, it has been employed to explain the resistivity minimum in a number of amorphous alloys including concentrated magnetic systems with reasonable success.

1.5.5 Weak Localization and Quantum Interference Effects

In highly disordered systems in which the electron mean free path is of the order of atomic spacing, motion of electrons at low temperatures is diffusive rather than ballistic [58, 59] and this realization has prompted many workers [57, 74–76] to propose quantum corrections to the normal Boltzmann conductivity, arising from quantum interference (QI) or weak localization (WL) effects and enhanced electron-electron interaction (EEI) effects.

Electrons in disordered systems undergo multiple scattering when the electron mean

free path is of the order of the inter-atomic spacing. At low temperatures, these collisions are elastic, and hence the electron wave-functions retain their phase over large distances. Therefore, there exists a finite probability for the two partial waves of the electron, originating from a point (origin) and propagating in opposite directions on a given path, to return to the origin in phase and interfere constructively. In other words, multiple elastic scattering leads to phase coherence between the partial waves scattered from nearby ions and hence enhances the probability for an electron to return to its origin, hence of 'localization' [58, 59]. The result of this electron localization process is that the electrical resistivity in the presence of such scattering in disordered materials is higher than that calculated from the quasi-classical Boltzmann approach. If the disorder is strong enough, the electrons can get completely localized leading to a transition from metallic to the insulating state. However, if the disorder is not sufficiently strong, the weak localization or quantum interference effects leads to a relatively higher resistivity. Since phase coherence is responsible for the weak localization, this also means that any process, which destroys the phase coherence of the two electron partial waves will reduce the additional resistivity (due to localization). A process, which is known to destroy the phase-coherence, is inelastic scattering. As the temperature is increased from absolute zero, the inelastic electron-phonon scattering sets in which tends to destroy the phase coherence and thereby leads to an increase in conductivity or a decrease in the resistivity, a result opposite to the normally observed behaviour in metals in which the resistivity should increase with rise in temperature due to electron-phonon scattering. The second process which destroys the phase coherence is the application of a magnetic field which produces a negative magnetoresistance. The third one is the electron-electron interaction which causes a decrease in resistances as T increases. The enhanced electron-electron interaction can be expressed as [75]

$$\begin{aligned} \Delta\sigma_{EEI}(T) &= [\sigma(T) - \sigma(0)]_{EEI} \\ &= \frac{e^2}{4\pi^2\hbar} \left(\frac{1.294}{\sqrt{2}} \right) \left(\frac{4}{3} - \frac{3}{2}\tilde{F}_\sigma \right) \left(\frac{k_B T}{\hbar D} \right)^{1/2} \end{aligned} \quad (1.31a)$$

$$\tilde{F}_\sigma = \frac{32}{3F} \left[\left(1 + \frac{1}{2}F \right)^{3/2} - \frac{3}{4}F - 1 \right] \quad (1.31b)$$

where F is the average static screened Coulomb interaction potential over the Fermi surface

and D is the diffusion constant. Eq.(1.31a) rewritten in the following form represents the EEI contribution to resistivity,

$$\frac{\rho_{EEI}(T)}{\rho_{EEI}(0)} = 1 - \rho_{EEI}(0) \left(\frac{1.294}{\sqrt{2}} \right) \left(\frac{4}{3} - \frac{3}{2} \tilde{F}_\sigma \right) \left(\frac{k_B T}{\hbar D} \right)^{1/2} \quad (1.32)$$

The contribution of electron-electron interaction to the total resistivity is thus proportional to $-\sqrt{T}$. It turns out that the effect of this Coulomb anomaly is dominant only at low temperature, say, below 20 K.

1.6 Aim and Scope of the Thesis

Magnetic phases of alloy systems with both ferromagnetic and antiferromagnetic exchange interactions are studied in details by many groups including ours. Ni-rich Ni-Fe-Cr and Ni-Fe-V alloys [77, 78] have shown exotic magnetic phases and have been studied rigorously by our group. Compositions near Ni80%-Fe20% have been widely investigated in bulk form not only for their rich magnetic phases but also for the unique quality of low magnetostriction and high initial permeability and they are ideal components for making magnetic cores for light electrical equipment applications as well as magnetic shielding materials. Application being one of the main motivations of science and technology of materials, permalloy and recently their thin films are still attractive systems to study. High permeability in these alloy systems is expected to result either from domain rotation against weak crystalline anisotropy or from boundary displacements where the opposing force is small [79]. In permalloys, Fe is often substituted with many transition metals for the enhancement of permeability and it is found that molybdenum enhances the permeability of the materials even if it is added in a small amount. In fact 5 % Mo substituted Ni-Fe alloy shows the highest permeability and is known as supermalloy. Not many works have been reported substituting Fe by 4d or 5d elements for substitution like Mo, or W, partly due to their high melting temperature which is a practical problem in getting homogeneous alloys. Recently many works have been reported on the thin films of Ni-Fe-Mo alloys as they have useful application in micro-electro-mechanical systems (MEMS) [80]. The high permeability in these alloys can be achieved using proper annealing technique and baking temperature. A high permeability can also be obtained

if the amount of Ni is reduced. Molybdenum at the same time increases the electrical resistivity of permalloys and hence reduces the eddy current loss. In this work we are concerned with their magnetic properties including critical exponents associated with the magnetic phase transitions as well as their transport properties. Tungsten occurs just below molybdenum in the periodic table and hence is a natural choice. Moreover, similar kind of Ni-Fe-Cr and Ni-Fe-V ternary alloy systems exhibit complex magnetic properties which are extremely sensitive to the concentration of Cr and V, respectively. This is understandable in view of the strong antiferromagnetic exchange interactions in Cr or V which lead to a competition between ferromagnetic and antiferromagnetic pair exchange interactions. Due to these conflicting pair interactions these systems have shown a host of interesting magnetic phases, like spin glass, mixed magnetic phase, etc. Therefore, these systems have generated a lot of interest and in the recent past they have been extensively studied. However, many aspects of their properties are yet to be understood completely.

Keeping the above motivation in mind, the main objective of the thesis are :

- (i) Detailed study of the magnetic phases of Ni-Fe-Mo and Ni-Fe-W alloy series to see how do 4d (Mo) and 5d (W) affect the ferromagnetic phase of Ni-Fe system.
- (ii) To make an in-depth study of low-lying magnetic excitations in Ni-Fe-Mo and Ni-Fe-W alloy series and to see the effect of Fe dilution in the systems.
- (iii) To investigate the thermal critical behaviour of Ni-Fe-Mo and Ni-Fe-W alloy series in details with reference to Fe dilution in the alloys.
- (iv) To identify the various scattering mechanisms in the electrical resistivity of Ni-Fe-V, Ni-Fe-Mo, and Ni-Fe-W alloy series and to determine their relative strengths.
- (v) To identify the various scattering mechanisms responsible for the resistivity minima of a set of Co-rich Ni-Cr pseudo-binary amorphous alloys and epitaxially grown Ni-nanocrystallites and determine their relative magnitudes.
- (vi) To compare the magnetic properties of a set of Ni-Fe-Mo alloy thin films with their bulk counterparts in the presence of various structural disorders.

In order to achieve the above mentioned objectives, experimental probes such as magnetization and electrical resistivity are chosen. The details will be discussed in the following chapters.

Chapter 2

Sample preparation and experimental details

In this chapter a brief overview of sample preparation and some basics of measurements are presented. Magnetic and electrical transport properties are measured in several disordered systems like arc-melted bulk alloys of three different series Ni-Fe-Mo, Ni-Fe-W, and Ni-Fe-V, a set of Pulsed LASER Deposited (PLD) thin films made from Ni-Fe-Mo alloy targets, self-assembled Ni nano-crystallites, and a series of melt-spun amorphous ferromagnets $\text{Fe}_{7.8}\text{Co}_{31.2}\text{Ni}_{39-x}\text{Cr}_x\text{B}_{14}\text{Si}_8$ ($x = 5, 10, 15$), and $\text{Fe}_{7.8}\text{Co}_{31.2}\text{Ni}_{24}\text{Mn}_{15}\text{B}_{14}\text{Si}_8$. For magnetic property measurements Quantum Designs Magnetic Property Measurement System (MPMS) magnetometer and for transport property measurements Quantum Designs Physical Property Measurement System (PPMS) and in a few cases home-made liquid He 4 cryostat with an automated data acquisition system are used.

2.1 Sample Preparation

2.1.1 Bulk samples

Samples of both Ni-Fe-Mo (six samples) and Ni-Fe-W (six samples) alloy series are prepared by arc melting, in ultra-pure argon atmosphere, of the required amount of 99.999 % pure constituent elements obtained from JohnsonMathey Inc. (England). The samples of Ni-Fe-V [81] (five samples) are prepared by induction melting in ultra-pure argon atmosphere of 99.999 % pure Ni, Fe, and V from Johnson-Mathey, Inc (England). Then the shiny buttons have been sealed in quartz tubes, flushed with ultra-pure argon gas, and then homogenized at 1300°C for 48 hours and quenched in water at room tem-

perature. The quenching is very important for these kinds of alloys for retaining their high-temperature crystallographic gamma phase as well as the random substitutional disorder without chemical clustering [81,82]. The alloy buttons are then swaged, cold rolled and cut into various shapes for different measurements. A final annealing was done in argon atmosphere at 1100° C to reduce strain due to cold rolling. This is especially important for electrical transport measurements. The amorphous ribbons were prepared by melt quenching onto the surface of a rotating wheel. The typical sample size used for transport measurements are $\sim 2 \text{ mm} \times 2 \text{ cm} \times 27 \mu\text{m}$.

2.1.2 Thin film samples

Contemporary technological applications have a bend towards compactness, making thin films an imperative requirement for integrating various circuit components. Moreover, thin films are immensely important for studying their properties primarily because compared to the synthesis of bulk single crystals, thin films can be easily produced in single crystal forms.

Various deposition techniques are available for synthesis of metallic thin films, such as pulsed laser deposition (PLD) [83–89], DC and RF sputtering [90–92], molecular beam epitaxy (MBE) [93], thermal evaporation [94], etc. PLD has emerged as an important growth technique since not only can it be used to deposit a spectrum of materials starting from metals to complex oxides but also it offers far-from-the-equilibrium growth conditions (the absorption of energy and ablation take place in a very short time before thermodynamic equilibrium is reached) not readily accessible by conventional thermal deposition techniques such as molecular beam MBE [83,84]. It has been already established that high quality epitaxial and nearly single-crystal-like thin films of superconducting high T_C cuprates, metallic, ferroelectric, ferromagnetic, dielectric oxides, and their multilayers have been successfully grown by this method [86]. Conceptually the basic process involved in almost all the thermal evaporation techniques is the same. The target material is evaporated to provide atomic or molecular species of sufficient background pressure to carry them forward to the properly heated substrate to get crystalline films. The choice of substrate is crucial for thin film deposition. The main deciding parameters are lattice

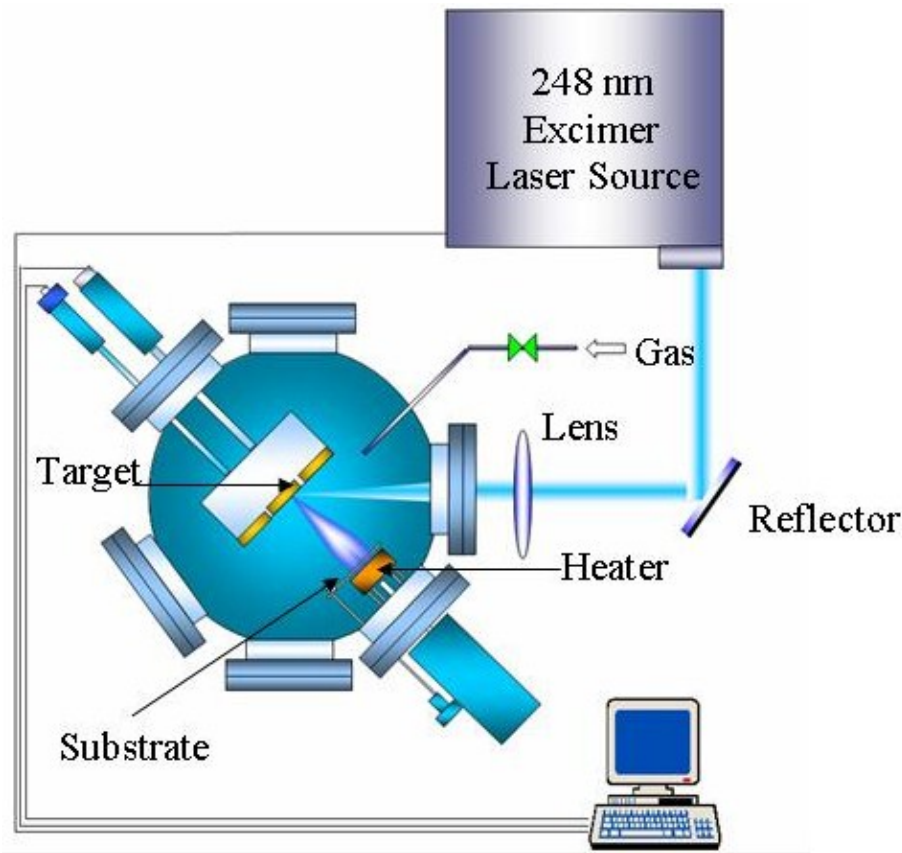


Figure 2.1: A schematic view of the pulsed laser deposition technique.

structure and lattice parameter of the target and the substrate, and also the orientation of the substrate. Propagation of the target stoichiometry to the thin film is the key to the success of the PLD technique which is found to be rather difficult for other conventional thermal evaporation processes. Excimer lasers such as XeF ($\lambda = 352$ nm), XeCl ($\lambda = 308$ nm), KrF ($\lambda = 248$ nm), KrCl ($\lambda = 222$ nm), ArF ($\lambda = 193$ nm), and F₂ ($\lambda = 157$ nm) are commercially available and can be used for thin film deposition. The typical duration of the laser pulse is 20–30 nanoseconds and the energy density is 1–5 J/cm². In such a short duration of a pulse, tremendous power (~ 100 –250 mW/pulse) is delivered to the target. For the current research work, thin films of Ni-Fe-Mo alloys are deposited by the PLD technique.

Typical schematic of the pulsed laser deposition technique is shown in Fig. 2.1. The laser beam of desired energy density is incident on the target at an angle of 45° with the

target surface. The target is rotated with the help of a stepper motor in order to avoid crater formation on the target due to repetitive ablation. The desired energy density is obtained by focusing the laser beam with the help of a quartz lens to a proper spot size. For the present work laser pulse energy is maintained at ~ 250 mW. The substrate is mounted in front of and parallel to the target at a distance of 4.5 cm on a resistive heater with the help of a thin conducting silver layer or clamp. The heater could go up to a temperature of 850° C. The temperature of the substrate is measured using a calibrated thermocouple placed on the substrate or on a separate small piece of the substrate itself. Before mounting the substrate, it is properly cleaned by the standard route in the sequence of acetone, methanol, and trichloroethylene in an ultrasonicator, each for five minutes and then the surface was blow-dried using nitrogen gas.

In order to start ablation, the energy density has to cross a certain critical value depending on the target material. A huge amount of energy is delivered in a few hundred-nanometer depth from the surface over a very short time. This transient way of energy transfer raises the temperature of the surface layers to a sufficiently high value (higher than the melting temperature of the material) and thus the material at the surface starts melting in a very short time. This causes a rapid ejection of the laser-induced plasma of materials (plume) at right angle from the surface of the target in the forward direction towards the substrate. The plasma plume contains various excited atoms, molecules, ions, and neutral particles. This plasma quickly expands away from the target towards the substrate where an adiabatic expansion of plasma at the surface of the heated substrate takes place leading to the growth of the desired thin film.

There are several parameters which influence the growth and properties of thin films. These parameters are laser energy density falling on the surface of the target, ambient background pressure during and after deposition, pulse repetition rate, temperature of the substrate, choice and orientation of the substrate itself, target to substrate distance, etc. Laser energy density is a vital factor which seriously affects the properties of films. If the energy density is low, the complex target molecules do not evaporate congruently; if very high, droplet kinds of particles are deposited on the substrate.

In spite of being the most successful growth techniques for the deposition of complex or multicomponent materials PLD suffers from certain drawbacks, such as difficulty in

large area film deposition due to narrow angular distribution of the plasma plume. To overcome this problem, the substrate can be scanned vertically/horizontally or the laser beam can be scanned over a large area of the target. Another major disadvantage is the splashing effect causing large particulates to nucleate on the film. This causes significant surface roughness. Sanding the target before deposition and continuous scanning of the target during deposition can minimize this effect.

The present samples are prepared at UGC-DAE Consortium for Scientific Research, Indore, India. The home-made deposition chamber is used with a KrF excimer laser (Lambda Physik, LPX200) having 248 nm wavelength. The details of the other parameters for preparing the films will be discussed in chapter 6.

2.2 Experimental set-up and measurements

2.2.1 Magnetic measurements

The study of magnetism of Ni-Fe-Mo and Ni-Fe-W alloys as well as their thin film counterparts is an integrated part of this thesis. All magnetic measurements are carried out using Quantum Designs Magnetic Property Measurement System (MPMS) magnetometer which is basically a Superconducting Quantum Interference Device (SQUID) magnetometer. A SQUID magnetometer consists of a superconducting ring containing one or more Josephson junctions. A brief description of the superconducting ring with two junctions is given below as shown in Fig.2.2 taken from ref. [95].

If a current I is passed through this circuit, current $I/2$ flows through each junction. Now if a magnetic field of gradually increasing flux density B is applied perpendicular to the plane of the ring, then a circular current i is induced within the ring. This means that current $i + (I/2)$ and $i - (I/2)$ flow through the right-junction and the left-junction of the ring, respectively. The phase change of an electron around any closed superconducting circuit is $2\pi n$, where n is an integer. Let us assume the phase difference of the tunneling current passing through the Josephson junctions in the right and left sides of the ring to be α and β , respectively, and the phase difference caused by magnetic field to be $\Delta\eta(B)$.

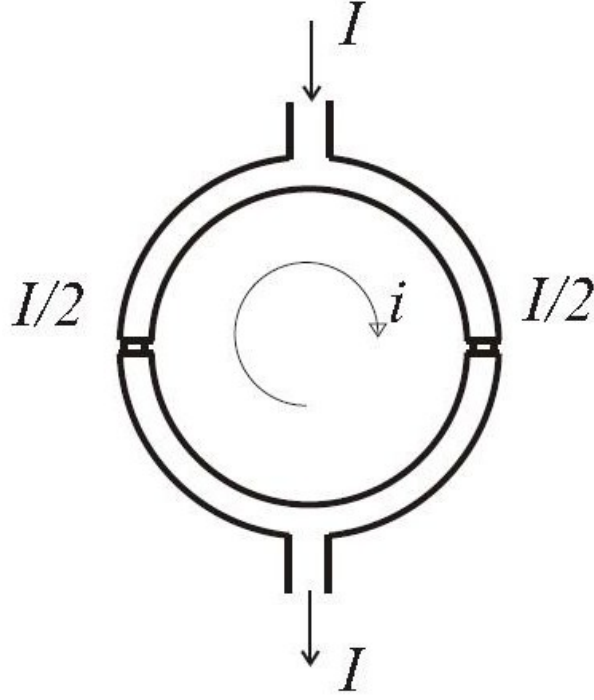


Figure 2.2: The superconducting ring with two junctions.

So

$$\alpha + \beta + \Delta\eta(B) = 2\pi n \quad (2.1)$$

Now the phase difference due to the magnetic field can also be written as

$$\Delta\eta(B) = 2\pi\left(\frac{\phi_a}{\phi_0}\right) \quad (2.2)$$

where ϕ_a is the magnetic flux passing through the ring and ϕ_0 is the quantum magnetic flux ($= h/2e = 2.0678 \times 10^{-15} \text{ T m}^2$). In the absence of any measuring current, $\alpha = \beta = \pi[n - (\frac{\phi_a}{\phi_0})]$. Now in the presence of a measuring current I , $\alpha \neq \beta$. Since $\alpha + \beta = \text{constant}$, we can write

$$\alpha = \pi\left[n - \left(\frac{\phi_a}{\phi_0}\right)\right] - \delta \quad (2.3)$$

$$\beta = \pi\left[n - \left(\frac{\phi_a}{\phi_0}\right)\right] + \delta \quad (2.4)$$

where δ depends on the magnitude of the measuring current I . Also,

$$i \mp I/2 = i_c \sin\pi\left[n - \left(\frac{\phi_a}{\phi_0}\right)\right] \mp \delta \quad (2.5)$$

This gives

$$I = 2i_c \cos\left\{\pi\left[n - \left(\frac{\phi_a}{\phi_0}\right)\right]\right\} \sin\delta \quad (2.6)$$

Since $\sin\delta \leq 1$,

$$I \leq 2i_c \cos\left[\pi\left(\frac{\phi_a}{\phi_0}\right)\right]. \quad (2.7)$$

Therefore the critical measuring current is found to be $I_c = 2i_c \cos\left[\pi\left(\frac{\phi_a}{\phi_0}\right)\right]$, which is an oscillating function with a period ϕ_0 and whenever the magnetic flux ϕ_a becomes a multiple of ϕ_0 , there is a maximum. Hence, the magnetic flux passing through the ring can be measured as multiples of ϕ_0 . The measurement of such a digitized quantity can be made very accurately, particularly since the magnitude of ϕ_0 is extremely small. This is the reason why a very weak magnetic field can be measured by using a SQUID magnetometer [95].

The MPMS magnetometer does not directly detect the magnetic field created due to the sample. A measurement is performed by moving a sample through the superconducting detection coils which are located at the center of the magnet provided with a constant dc magnetic field required during measurements. The sample moves along the symmetry axis of the detection coil and the magnet. Moving sample induces an electric current in the detection coils which are connected to the SQUID input coil with superconducting wires, allowing the current from the detection coils to inductively couple to the SQUID sensor. The thin film SQUID device is located approximately 11 cm below the magnet which provides a magnetic field to the sample for all measurements and is also properly magnetically shielded. The SQUID functions as a highly linear current-to-voltage converter so that variations in the current in the detection coil circuit produce corresponding variations in the SQUID output voltage. Under ideal conditions, the magnetic moment of the sample does not change during the transport through the detection coil. The detection coil is basically a second-order-gradiometer detection coil. It is a single piece of superconducting wire wound in a set of three coils. In this configuration, the upper coil is a single turn wound clockwise, the center coil comprises of two turns wound counter-clockwise, and the bottom coil is a single turn wound clockwise.

Figure 2.3 shows the calculated output (in arbitrary unit) of the SQUID electronics as a function of sample position. The x-axis shows the sample position, when $x = 0$, the

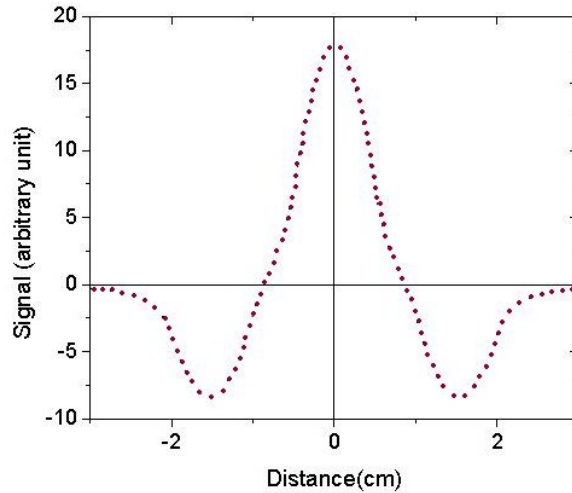


Figure 2.3: Sample position in SQUID detection coil and the corresponding signal.

sample is at the center of the detection coils. In this figure the single turn upper and bottom coils are 1.5 cm from the central coil. For our magnetic measurements, in case of bulk samples, we have used straw packing to fit the sample in the sample holding straw but in the case of thin films we have mounted the sample without any straw packing in order to avoid the paramagnetic contribution of the packing materials. Quantum Design provides two standard transport options to be used with the MPMS. The DC transport and RSO transport. The RSO transport is primarily used for samples with small magnetic moments. For the thin film sample all the measurements are done in the RSO mode.

2.2.2 Electrical Transport Measurements

The electrical transport measurements, namely, the electrical resistivity and the magnetoresistance, have been done using Quantum Design's Physical Property Measurement System (PPMS) [96].

The resistivity of the samples has been measured down to 2 K and magnetic fields up to 5 T using standard dc four-probe method. Figure 2.4 shows the schematic diagram of the 8 T PPMS system along with the pucks used for resistivity measurements. The system works down to 2 K in general and down to 300mK with ^3He insert. Fields up to 8 T is achieved using hybrid NbTi and Nb₃Sn magnets. The field homogeneity is better

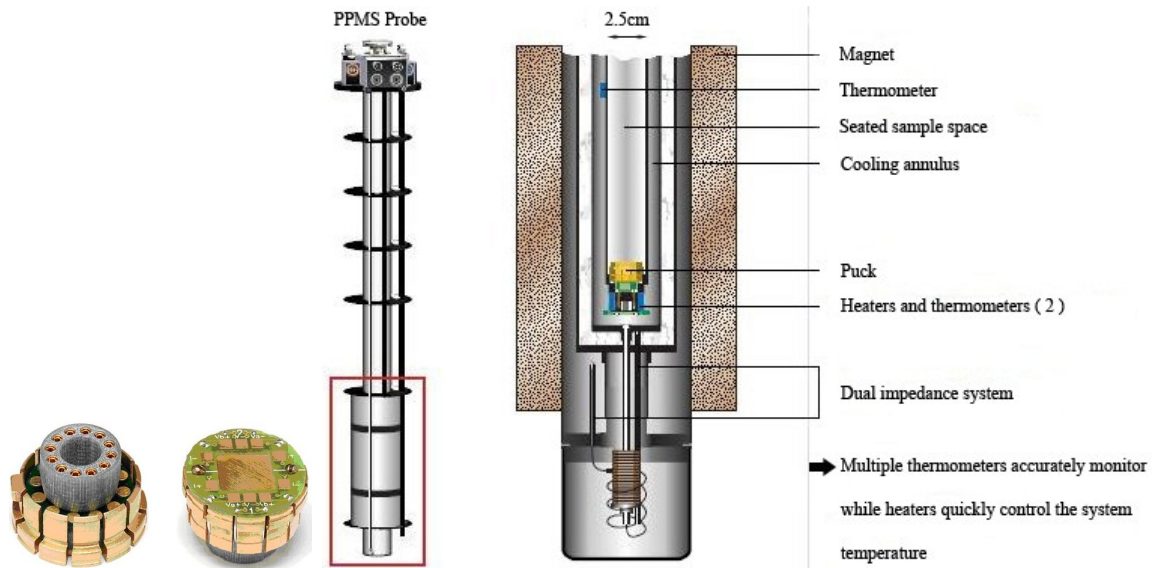


Figure 2.4: Schematic diagrams of QD-PPMS system and the photograph of pucks used for mounting samples.

than 0.1% over 1cm DSV. The temperature can be controlled better than 10 mK. PPMS uses lock-in technique to detect the signal (higher signal to noise ratio) this requires an oscillating current. The drive type is DC 8.3Hz square wave for measuring both in +ve and -ve cycle to eliminate the thermo e.m.f. The data averaging is done over specified user defined time to enhance signal to noise ratio.

Typical sample dimensions are $1 \text{ cm} \times 3 \text{ mm}$. They are pasted on the sample holder by using GE varnish (good thermal conductor but bad electrical conductor). Samples are connected to the puck using silver wires. The connections are made with silver paste. Care has been taken to make the contacts on the sample as close to a point contact as possible. After making the contacts the samples are kept under IR lamp for drying. The contacts could not be made using pure indium, as indium becomes superconducting around 3.6 K and our measurements were down to 1.5 or 2 K. In case of the amorphous alloys current and the voltage contacts with the sample were made with a nonsuperconducting Zn-Cd solder.

The home-made set-up used for resistivity measurements of amorphous alloys and Ni-nanocrystallites is already described in another thesis work [82,97].

Chapter 3

Magnetic phases of Ni-rich NiFeMo and NiFeW alloys

In this chapter, we present detailed experimental investigation and analysis of the magnetization behaviour of two series of disordered ternary Ni-Fe-Mo and Ni-Fe-W alloys. Here our primary aim is to observe the effect of increasing Mo (4d) and W (5d) on the magnetization of these alloys. We have studied the variation of magnetization with temperature (at low external fields) and magnetic field (at different temperatures). Compositions of the alloys are confirmed by Energy Dispersive X-ray Spectroscopy (EDS) using scanning electron microscope. X-ray diffraction measurements have been done in order to identify the crystallographic phase of the alloys. They show paramagnetic to ferromagnetic transitions across the composition range. However, we do find in one composition of Ni-Fe-Mo alloy with 13.5 at. % Mo, the presence of a mixed ferro-spin-glass phase. The absence of similar complex magnetic phase in Ni-Fe-W series is justified in view of the lack of samples near the critical concentration. All these and a few more detailed findings are discussed below.

3.1 Structural Characterizations

3.1.1 X-ray diffraction

The crystallographic phase of both the Ni-Fe-Mo and Ni-Fe-W alloy series are found by standard X-ray Diffraction (XRD) method using Phillips XPert PRO Diffractometer. The XRD measurements revealed that all the alloys are of single FCC phase. The measured

lattice constants differ by only 1.5 to 2 % from that of pure nickel and are given in Table 6.1 with a few other important parameters. Higher the concentration of Mo or W, lower is the corresponding 2θ values; but only by very small amounts implying that the lattice parameters do not differ significantly. A typical lattice constant for Mo10.9 alloy is $a = (3.565 \pm 0.004) \text{ \AA}$ and for W10.5 alloy, $a = (3.576 \pm 0.007) \text{ \AA}$. Figure 3.1 shows typical XRD patterns for $\text{Ni}_{83.1}\text{Fe}_{6.0}\text{Mo}_{10.9}$ and $\text{Ni}_{82.6}\text{Fe}_{6.9}\text{W}_{10.5}$. It is very difficult to make powders from these alloys and the XRD measurements are done with rolled pieces only. This has affected the normal intensity ratio of the lines, e. g., making (111) line less intense compared to (200).

3.1.2 Energy dispersive X-ray spectroscopy

The nominal compositions of all the alloys of Ni-Fe-Mo and Ni-Fe-W series are found by energy dispersive X-ray spectroscopy (EDS) using Phillips scanning electron microscope. The composition is checked at several places on the sample in order to get accurate results; this is also essential in ensuring that the alloys are homogeneous. In Table 6.1, the actual alloy compositions are given as found from the EDS measurements.

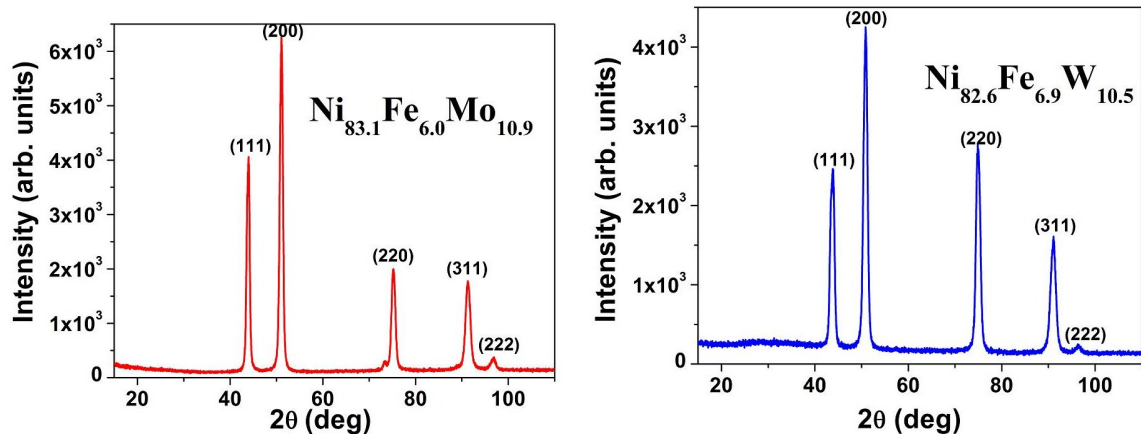


Figure 3.1: X-ray diffraction patterns of $\text{Ni}_{83.1}\text{Fe}_{6.0}\text{Mo}_{10.9}$ and $\text{Ni}_{82.6}\text{Fe}_{6.9}\text{W}_{10.5}$ alloys.

Table 3.1: Alloy composition, lattice parameter (a), saturation magnetisation (M_S), Curie temperature (T_C), and spin-glass transition temperature (T_g).

Alloy Composition	a (Å)	M_S (emu/g)	M_S (μ_B)	T_C (K)	T_g (K)
Ni _{81.0} Fe _{16.7} Mo _{2.3}	3.558	80.5	0.85	720	-
Ni _{80.4} Fe _{12.9} Mo _{6.7}	3.565	53.6	0.56	495	-
Ni _{83.4} Fe _{10.7} Mo _{5.9}	3.568	51.3	0.54	470	-
Ni _{83.5} Fe _{7.6} Mo _{8.9}	3.561	32.5	0.34	320	-
Ni _{83.1} Fe _{6.0} Mo _{10.9}	26.5	26.5	0.28	182	-
Ni _{83.2} Fe _{3.3} Mo _{13.5}	3.571	7.9	0.80	45	10
Ni _{78.9} Fe _{18.1} W _{3.0}	3.560	80.4	0.85	775	-
Ni _{79.4} Fe _{14.1} W _{6.5}	3.562	54.2	0.57	530	-
Ni _{81.0} Fe _{11.8} W _{7.2}	3.567	50.0	0.53	515	-
Ni _{83.5} Fe _{7.6} W _{8.9}	3.573	28.6	0.30	305	-
Ni _{82.6} Fe _{6.9} W _{10.5}	3.576	23.0	0.24	191	-
Ni _{86.6} Fe _{3.1} W _{10.3}	3.575	10.4	0.11	57	-

3.2 Magnetic Characterizations

3.2.1 DC magnetization

The first step towards knowing the magnetic phase of any alloy is to find its Curie temperature (T_C) (if any) using any standard dc or ac method. In this section we will discuss dc magnetization behavior of all the alloys. We have cooled the sample to the lowest desirable temperature in zero applied magnetic fields, applied a small field ~ 20 or 50 Oe, and then measured while heating the magnetization till T_C is found. This is known as the zero field cooled (ZFC) method. Next the sample is cooled again

keeping the same field ~ 20 or 50 Oe to the lowest required temperature and the magnetization was measured in the heating cycle only. This is the field cooled (FC) method. In general, for ferromagnetic alloys the FC and ZFC curves coincide provided the measuring field is higher than the coercive field of the alloy. In case of alloys with complex magnetic phases, a bifurcation between the FC and ZFC curves is found. The

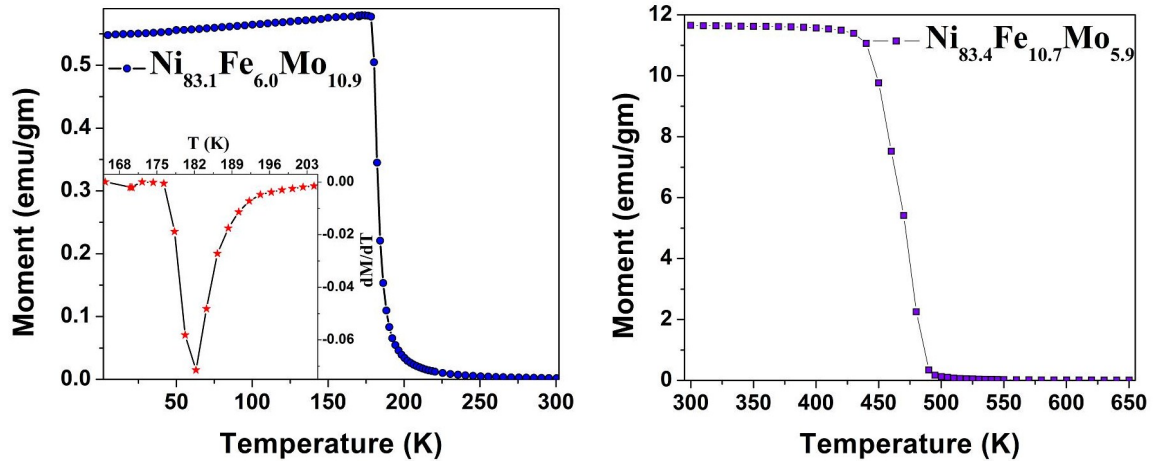


Figure 3.2: Magnetization (ZFC) vs. temperature for two compositions: (left) Mo10.9 with a lower T_C and (right) Mo5.9 with a higher T_C .

dc magnetization measurements of Ni-Fe-Mo and Ni-Fe-W alloy series are done using QDMPMS (discussed in Chapter 2). In all the samples except Mo13.5, ZFC and FC curves are coincident and we do find that their coercive fields (~ 0.1 Oe) are much less than the measuring field. Figure 3.2 shows the magnetization vs. temperature (ZFC) curves for

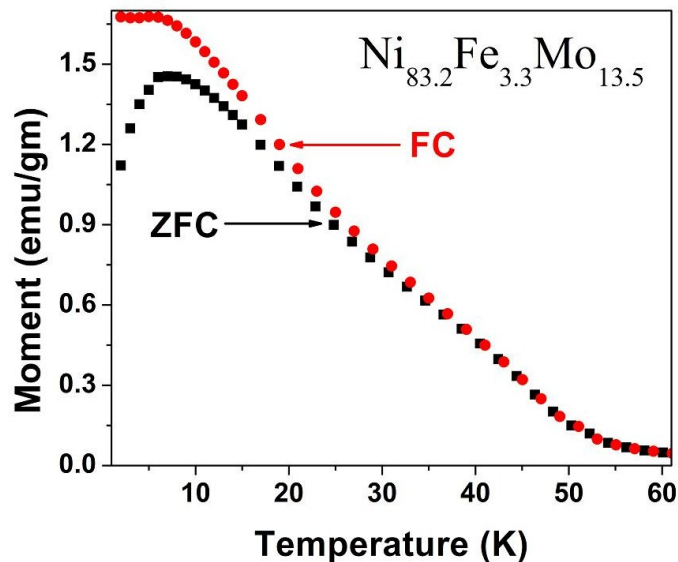


Figure 3.3: Magnetization as a function of temperature for Mo13.5 for both field-cooled and zero field-cooled situations at an applied field of 20 Oe.

two representative samples: one with a higher Mo concentration Mo10.9 measured at 20 Oe and the other with a lower Mo concentration Mo5.9 taken at 50 Oe. As shown in the inset, the critical temperature T_C is obtained from the dip in dM/dT which corresponds to the point of inflection in the M vs. T curves. The higher the Fe concentration the higher is the T_C , while the reverse trend is seen with increasing Mo concentration.

The sample Mo13.5 shows a different behavior. Figure 3.3 shows its M vs. T plot for both field-cooled and zero field-cooled cases at applied fields of 20 Oe. Unlike all other samples they now bifurcate at low temperatures around 30 K. The ZFC curve show two magnetic transitions quite clearly, once at $T_C = 44$ K (inflection point) and then a peak at 10 K, the latter is a signature of memory effects characteristic of a spin-glass transition. We shall discuss in details the magnetic measurements made to confirm the spin-glass phase of this particular alloy later in this chapter.

Similar kinds of dc magnetization measurements are carried out for the W alloys as well. Figure 3.4 displays the magnetization variation with temperature for three different compositions. The left panel is for a sample with low Fe content W10.3 measured at 20 Oe field. The critical temperature T_C is obtained, as shown in the inset, by a sharp dip in dM/dT vs. T . The right panel shows M vs. T for two compositions with higher

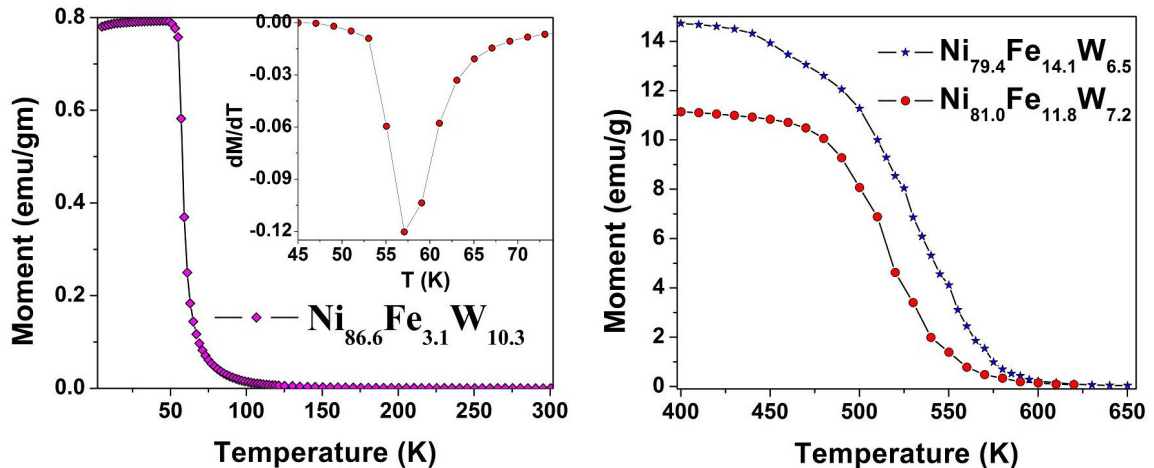


Figure 3.4: Magnetization vs. temperature for three compositions: (left) low Fe content of 3.1 at %, also showing dM/dT vs. T in the inset and (right) higher Fe content of 11.8 and 14.1 at %.

Fe content W7.2 and W8.6, both measured at an external field of 50 Oe. We note that T_C increases with Fe content for all the samples. Unlike the case of Ni-Fe-Mo, at no composition there is any sign of glassy behaviour with different FC and ZFC response, at least till W concentration of 10.5 at %.

To complete the dc magnetic characterization of the systems, magnetization is measured as a function of applied fields at 5 K, 80 K, and 300 K. Figure 3.5 shows the M vs. H curves at 5 K till 5 T for three representative samples of each alloys series, Mo8.9, Mo10.9, and Mo13.5 in the left panel and W8.9, W10.5, and W10.3 in the right panel. Samples with lower content of Mo and W, measured till 0.6 T, shows similar behavior as those shown in Fig. 3.5.

The saturation fields are very small in all cases. In the case of 80 and 300 K measurements, only the moments are low but the other characteristics of the M - H loop remain unaltered. None of the samples show appreciable hysteresis with very small coercive fields of ~ 0.1 Oe. The saturation magnetization decreases with increasing Mo and decreasing Fe concentrations. The moment in the W series is lower than that of the Mo series. The saturation magnetization for both the alloy series is given in Table 6.1.

In order to consolidate the dc results, we have plotted in Fig. 3.6 T_C vs. concentration

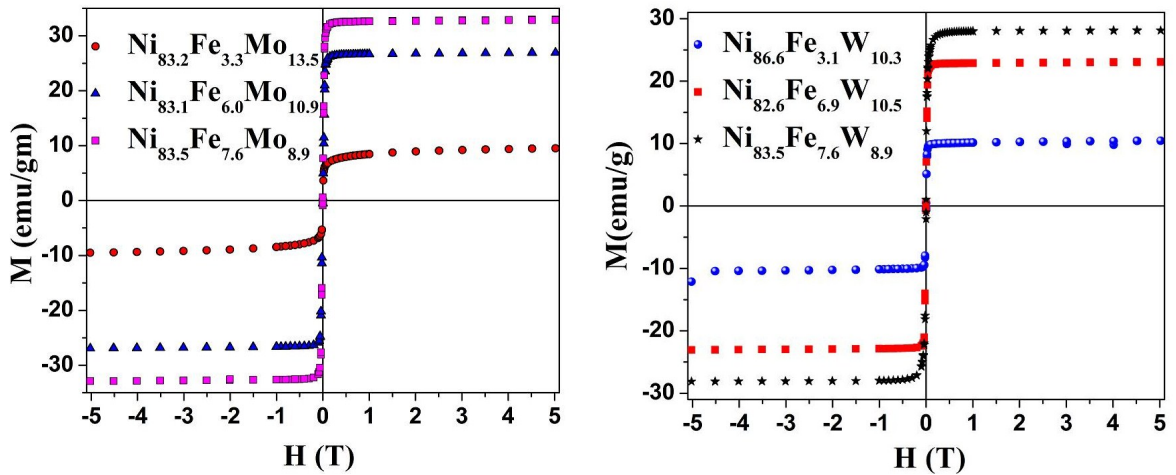


Figure 3.5: M vs. H are shown for three representative samples of each series: Mo8.9, Mo10.9, and Mo13.5 (left panel) and W8.9, W10.5, and W10.3 (right panel) at 5 K till applied fields of 5 T.

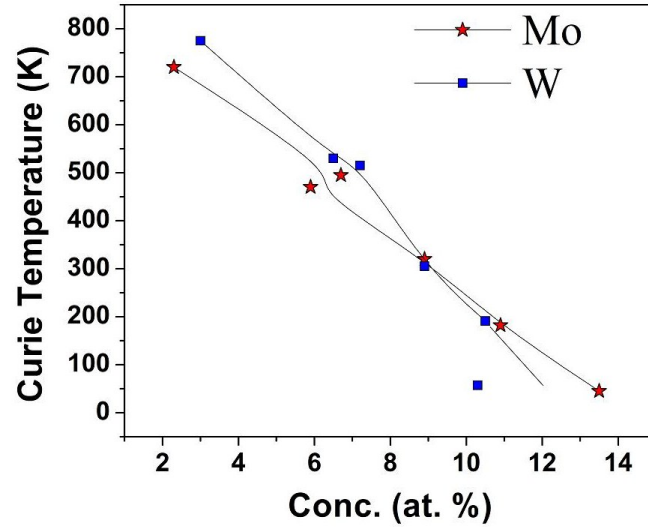


Figure 3.6: Curie Temperature (T_C) is plotted as a function of Mo and W content in the respective alloy systems.

(%) and find that for the Mo system, T_C extrapolates to 0 K for 14.2 at. % Mo. The Slater-Pauling curve [98] gives $T_C \sim 0$ K for 18 % Cr in Ni. The split-band model of Berger [99], however, gives the same critical concentration of ~ 12 % for Cr, Mo, and W, since they belong to the same column in the periodic table although belonging to 3d, 4d, or 5d rows. In the W alloy series, the W content is nearly the same in the two samples W10.3 and W10.5 but due to different Ni/Fe content, T_C s are widely different. The Ni/Fe content of W10.5 is closer to those of the rest of the alloys than that of W10.3. So in Fig. 3.6 we have disregarded W10.3. The critical concentration is found to be 13 at. % for W system.¹

Theoretical analysis of both the alloy systems are also carried out in our group, using the first-principles tight-binding linear muffin-tin orbital (TB-LMTO)-based augmented space recursion (ASR) method clubbed with mean-field phase analysis to supplement the experimental findings. The gist of the theoretical analysis is as follows:

- (i) In case of Ni-Fe-Mo alloy series there is a possibility of a spin-glass phase around 13–15 at. % of Mo, as Fe boosts though Mo depletes the fragile moments of Ni creating

¹This part of the chapter has been published in *Physica B* **405** (2010) [for Mo alloys] and *J. Magn. Magn. Matl.* **322** (2010) [for W alloys].

frustration in the system.

- (ii) In case of Ni-Fe-W alloy series, even at low Fe concentrations, not only frustration decreases, but Ni also loses its moment, confirming that spin-glass transition may not take place in this system even at low Fe concentrations.

The detailed discussion of the theoretical work is the subject matter of another thesis work from our group.

3.2.2 AC Susceptibility

Along with the dc measurements we have performed ac susceptibility measurements of the alloys having $T_C \leq 300$ K in both the series. The dc magnetic measurements determine

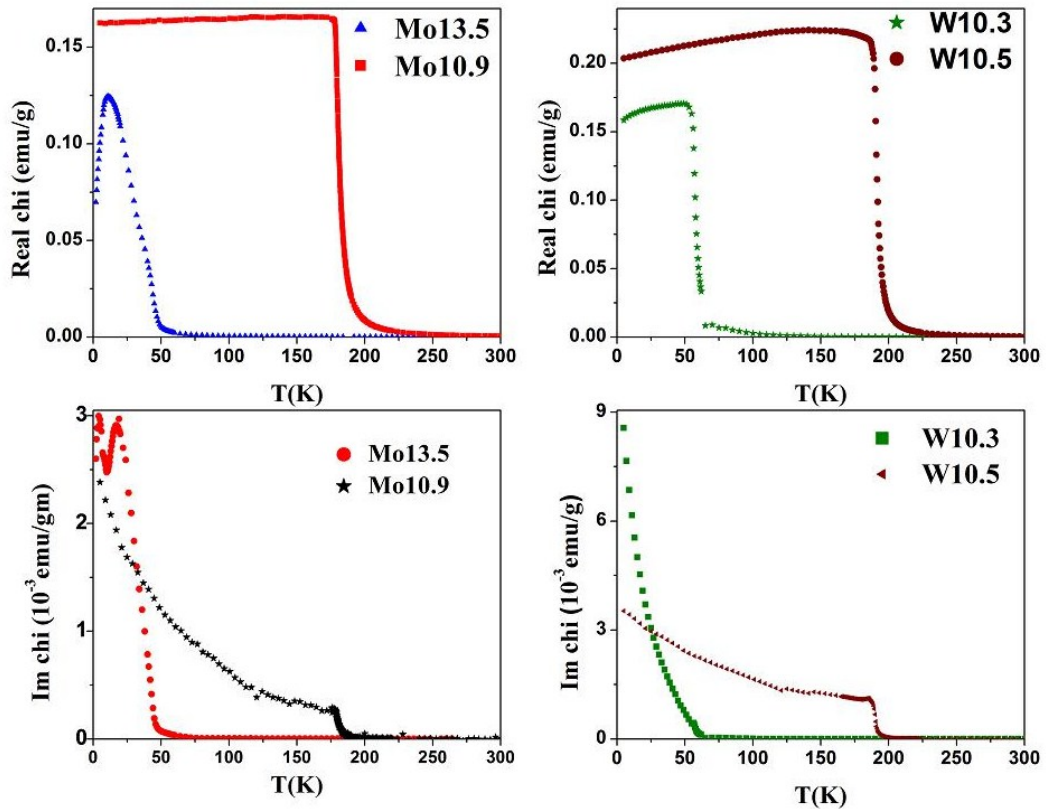


Figure 3.7: Temperature variation of real (upper panel) and imaginary (lower panel) parts of ac susceptibility measured at 33 Hz for samples Mo13.5, Mo10.9, W10.3, and W10.5.

the equilibrium value of the magnetization in a sample and ac susceptibility (χ) provides information about its magnetization dynamics. The ac susceptibility has two components, namely the real part (χ') and the imaginary part (χ''). The real part of ac susceptibility at low frequencies is more or less equivalent to the dc magnetization but at higher frequencies, due to dynamic response of the sample, it does not follow the dc magnetization curve. In case of systems with complex magnetic phases like spin glass, etc. the real part of the ac susceptibility shows distinct frequency dependence. The imaginary part of the ac susceptibility indicates dissipative processes in the sample. In conductive samples, the dissipation is due to eddy currents. In ferromagnets, a non-zero χ' might indicate irreversible domain wall movement or absorption due to a permanent moment [100]. The imaginary part of the ac susceptibility is the Fourier transform of the two-spin correlation function which characterizes the dynamics of the magnetic system and is expected to show some anomalous behavior in case of systems with complex phases. Relaxation and irreversibility in spin glasses give rise to a non-zero χ'' . Also, both χ' and χ'' are very sensitive to thermodynamic phase changes, and are often used to measure transition temperatures.

The temperature dependence of the real and imaginary parts of ac susceptibility is shown in Fig. 3.7 for two Ni-Fe-Mo and two Ni-Fe-W compositions, measured at 33 Hz. The T_C found here from both χ' and χ'' are in good agreement with those found from dc magnetization measurements. Only one sample Mo13.5 shows a peak in χ' which is a signature of a spin-glass-like state. We also observe for this sample that there is a bifurcation in the peak of χ'' ; the dip is just around the temperature where χ' has its peak. This could be very well an experimental artifact as the signal for the imaginary part is quite small as compared to the real part of the ac susceptibility. Detailed ac measurements have been done in this particular sample in order to confirm the magnetic phase of this alloy which is close to the percolation concentration. This is discussed with some other more specific measurements in the following section.

3.3 Low-temperature Complex Phase of $\text{Ni}_{83.2}\text{Fe}_{3.3}\text{Mo}_{13.5}$ Alloy

Unlike other transition metals alloyed with a non-magnetic metal, alloys of Ni behave rather differently. This is because of the fragility of the local magnetic moment on Ni. NiMo does not show any spin-glass phase. However, addition of Fe can bolster the moment on Ni. In this section we will discuss specific experiments carried out in details to understand the low temperature magnetic phase of the alloy $\text{Ni}_{83.2}\text{Fe}_{3.3}\text{Mo}_{13.5}$. This particular composition is near to where mean-field estimates suggest that there could be a spin-glass phase.

Alloys in a complex spin-glass phase show many distinct features like [101]:

- (i) A peak in both the dc and ac magnetization/susceptibility data. The temperature at which this peak occurs is known as the glass transition temperature (T_g).
- (ii) Bifurcation between FC and ZFC curves till some relatively higher applied magnetic fields.
- (iii) Highly non-saturating M-H curve with a fat hysteresis loop at temperatures around T_g .
- (iv) Shift in the peak position of χ' towards higher temperatures as well as lower peak height with increasing applied frequency.
- (v) Magnetic relaxation follows a logarithmic or a Kohlrausch stretched exponential decay.

Keeping in mind all these signature effects of the spin-glass phase, we have measured field dependence of the FC and ZFC $M(T)$ curves, M-H curves below and above T_g , ac susceptibility vs. T at several frequencies, and the time dependence of the remanent magnetization of this particular sample.

Figure 3.8 shows the magnetization variation with temperature for both field-cooled (FC) and zero-field-cooled cases (ZFC). For ZFC measurements, the sample was cooled down from 100 K ($\gg T_C$ and T_g) to 2 K in zero magnetic fields. After cooling, an external magnetic field of 20/50/100 Oe is applied and held constant while the magnetization was

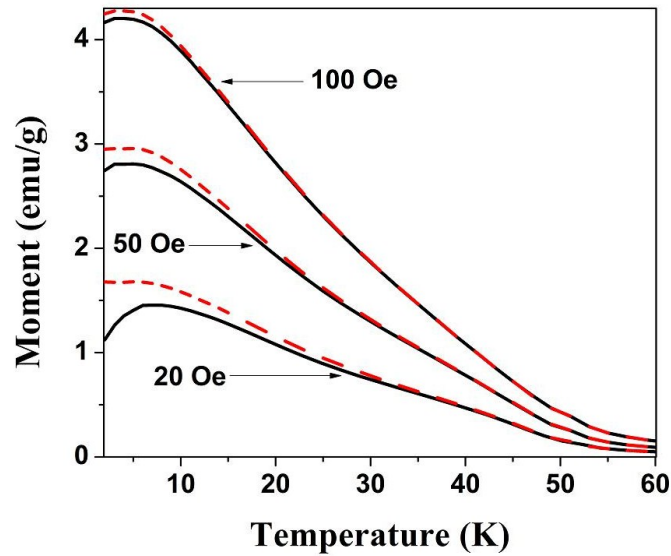


Figure 3.8: Magnetization vs. temperature under FC and ZFC conditions at three different external fields.

measured as the temperature is raised slowly (1 K min^{-1}) up to 60 K. Subsequently, the temperature is lowered again down to 2 K with the field kept on and the field-cooled (FC) magnetization data are taken with the temperature raised quasi-statically till 60 K at the same heating rate. For the low external field of 20 Oe, the ZFC and FC diverge from each other at low temperatures around 30 K. With increase of external field to 50 Oe, the ZFC and FC curves bifurcate around 20 K, and at 100 Oe, the two coincide at almost all temperatures. The T_g has changed from 12 K to 7 K and then to 6 K for applied fields of 20, 50, and 100 Oe.

The above behavior can be explained as follows: When we cool the sample to 2 K in zero-fields, it undergoes spin-glass freezing. Now if we turn on a very small field it cannot unfreeze (or melt) the spins and M is small. Now when we start to heat the sample, thermal fluctuations begin to gradually unfreeze the spins, which then align because of the magnetic field and the magnetization increases. Finally, when all spins are unfrozen at T_g we get a maximum. Further heating causes thermal fluctuations to randomize the spins (destroy any ordering) and the magnetization decreases as in a paramagnet. The ZFC state is a metastable one, while the FC state is an equilibrium state. Now if we cool down to 2 K in the presence of the magnetic field, it aligns the moments more and more

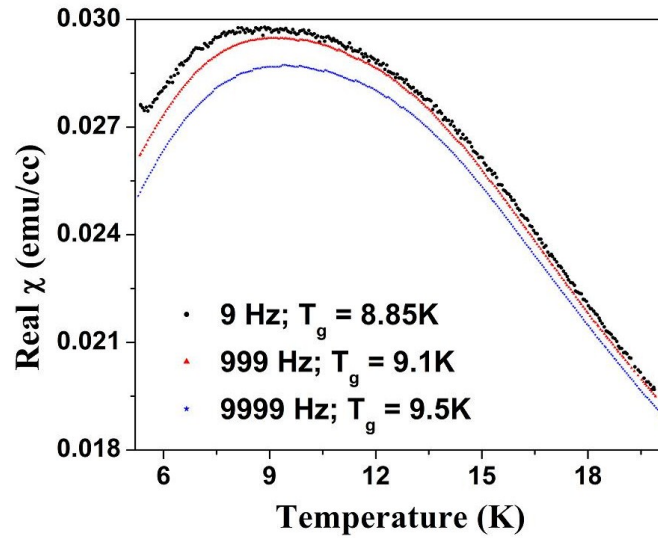


Figure 3.9: Variation of the real part of ac susceptibility with temperature for different frequencies.

so that at the lowest temperature we get the highest magnetization. Now as we heat the sample and measure magnetization, it can only decrease. The two heating curves meet at the irreversibility temperature T_{irr} . On the other hand, when we first cool down to 2 K in zero fields and turn on a relatively higher field ($\sim > 100$ Oe), the spin-glass ordering is destroyed by the field and with raising of temperature the magnetization decreases like a paramagnet. Cooling down in the presence of the large field means even at 2 K, there is no spin-freezing and subsequent heating produces a curve almost identical to the ZFC case. Since such a behavior is observed, this is a clear signature of memory effects characteristic of a spin-glass transition.

Figure 3.9 shows the variation with temperature of the ac susceptibility at different frequencies, all showing rounded maxima. The temperature, at which the maximum occurs, increases with frequency, a typical characteristic of the spin-glass phase. Assuming there are clusters of different volumes in the alloy giving rise to a distribution of moments we can interpret the ac susceptibility data as follows. Any maximum occurs due to two competing processes. At the lowest temperatures the moments are frozen in random orientation, hence they hardly respond to the ac-field. As we raise the temperature the thermal energy gives them some freedom to respond and the susceptibility increases with

temperature till all clusters get unlocked at T_g . Further increase in the thermal energy disrupts all the alignments and so the moment starts falling as in a paramagnet. Now, the clusters of smaller size are unlocked at lower temperatures compared to those having larger moments. To unlock the bigger clusters at higher frequencies one has to increase the temperature such that their relaxation frequency ν_r ($\sim \exp(-KV/k_B T)$) \approx measuring n where V is the volume of the cluster, K is the anisotropy constant, and KV is the energy barrier. Thus T_g shifts to higher temperatures for higher frequencies. At lower frequencies moments of all size will be able to follow the magnetic field while at larger frequencies the smaller clusters respond more than the larger clusters and hence the smaller values of the susceptibility for higher frequencies. This behavior is consistent with the dynamical mean-field theory of spin glasses in a coupled-mode approximation described by Chowdhury and Mookerjee [102]. Here the dynamics described is that of coupled eigenmodes of the random exchange pair interaction (EPI). At higher temperatures the dynamics is dominated by finite sized Anderson localized eigenmodes of the random EPI. Spin-glass transitions occur when $k_B T$ crosses the mobility edge and an infinite sized extended eigenmode with infinite lifetime exhibits frozen behavior. The time scales associated with a finite frequency measurement are inversely proportional to the frequency. So at a higher frequency, susceptibility measurements will see a finite localized mode as frozen, giving a maximum at a higher temperature.

Coming back to $T_g(\nu)$, the temperature shift in terms of $(\Delta T_g/T_g) \times 100\%$ per decade of ν is $\sim 0.5\%$ in canonical spin glasses CuMn, AuMn, and AgMn [101]. Here in this alloy it has a much higher value of $\sim 2.4\%$. Figure 3.10 shows the variation of T_g with frequency of the applied ac field. The solid line is just a guide to the eye. It seems therefore from the dc and ac measurements described above, this alloy does behave like a spin-glass at low temperatures.

However, the first surprise comes with the hysteresis curves shown in Fig. 3.11. The curve for 20 K ($> T_g$) resembles that of a ferromagnet except that even at 50 kOe there is no sign of saturation. At 5 K ($< T_g$) we expected a shifted hysteresis curve with a large coercive field as found in canonical spinglasses [103]. However, the coercive field remains very small as in soft ferromagnets, but unlike a ferromagnet there is no saturation even at 50 kOe field.

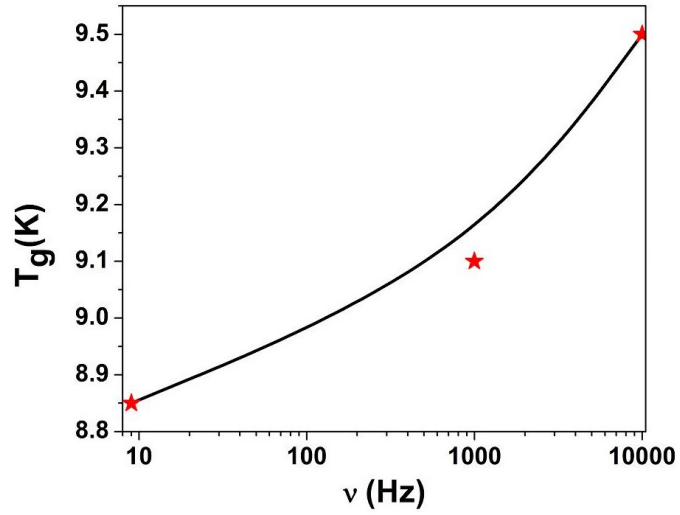


Figure 3.10: Variation of peak temperature (T_g) with frequency of the applied ac field. The solid line is just a guide to the eye.

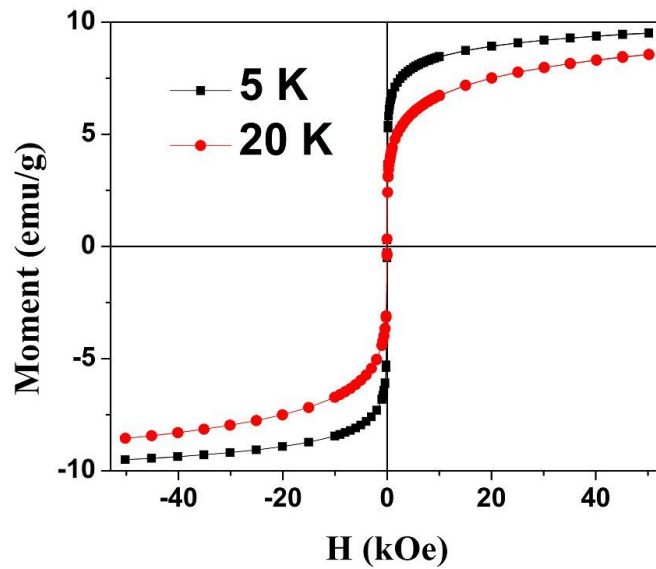


Figure 3.11: The hysteresis (magnetization vs. magnetic field) curves for temperatures above and below the spin-glass temperature.

Table 3.2: Fitted relaxation time parameters ($\tau_1 < \tau_2$) for the double exponential decay of magnetization at 6 and 10 K.

Temperature (K)	τ_1 (sec)	τ_2 (sec)
6	150	1557
10	93	913

We next focus on magnetic relaxation studies. In these experiments the sample is cooled in a magnetic field of 30 Oe from 300 K to the temperature of measurement. The field is then turned off and the relaxation of magnetization is studied as a function of time. Figure 3.12 shows the relaxation results. At high temperatures (80 K) we essentially observe noise around $m \simeq 0$. At these high temperatures magnetization cannot be sustained. At the lower temperatures we observe a double exponential relaxation:

$$m(t) = m_{eq} + A \exp(-t/\tau_1) + B \exp(-t/\tau_2), \quad (3.1)$$

an initial relatively fast relaxation followed by a slower one, but still an exponential decay. Table 6.2 shows the short and long relaxation times τ_1 and τ_2 at 6 and 10 K. As expected, both the fast and the slow relaxations speed up with temperature. The double exponential fits are shown in the bottom panel. Again, this is an unexpected result if we believe that this alloy is in a pure spin-glass state at low temperatures. This the second surprise. There is no signature either of a logarithmic or a Kohlrausch stretched exponential decay even at long times. Therefore it appears that the alloy, at low temperatures, has characteristics of both spin glasses and random ferromagnets.

The magnetic relaxation of this particular alloy has been analyzed theoretically by our group using atomistic approach, based on the quantum description of solids, as proposed by Skubic et al. [104]. This approach provides a study of magnetization relaxation from first-principles, appropriate for systems with complex chemical compositions. This theoretical approach also concludes a similar kind of double exponential relaxation of magnetization as found in our experiments. Again, the detailed theoretical study is the subject matter of another thesis work from our group; so the gist of that analysis is

presented above.

In summary, we are faced with the fact that in some aspect the alloy $\text{Ni}_{83.2}\text{Fe}_{3.3}\text{Mo}_{13.5}$ behaves like a spin-glass; e.g., the bifurcation between ZFC and FC curves and the variation of the maxima in the ac susceptibility with frequency. On the other hand, the hysteresis curves and magnetic relaxations resemble those of a random ferromagnet. Our understanding from some theoretical work [105, 106] and experimental data on other materials [107–111] suggests that the alloy $\text{Ni}_{83.2}\text{Fe}_{3.3}\text{Mo}_{13.5}$ in all probability is in a ferro-

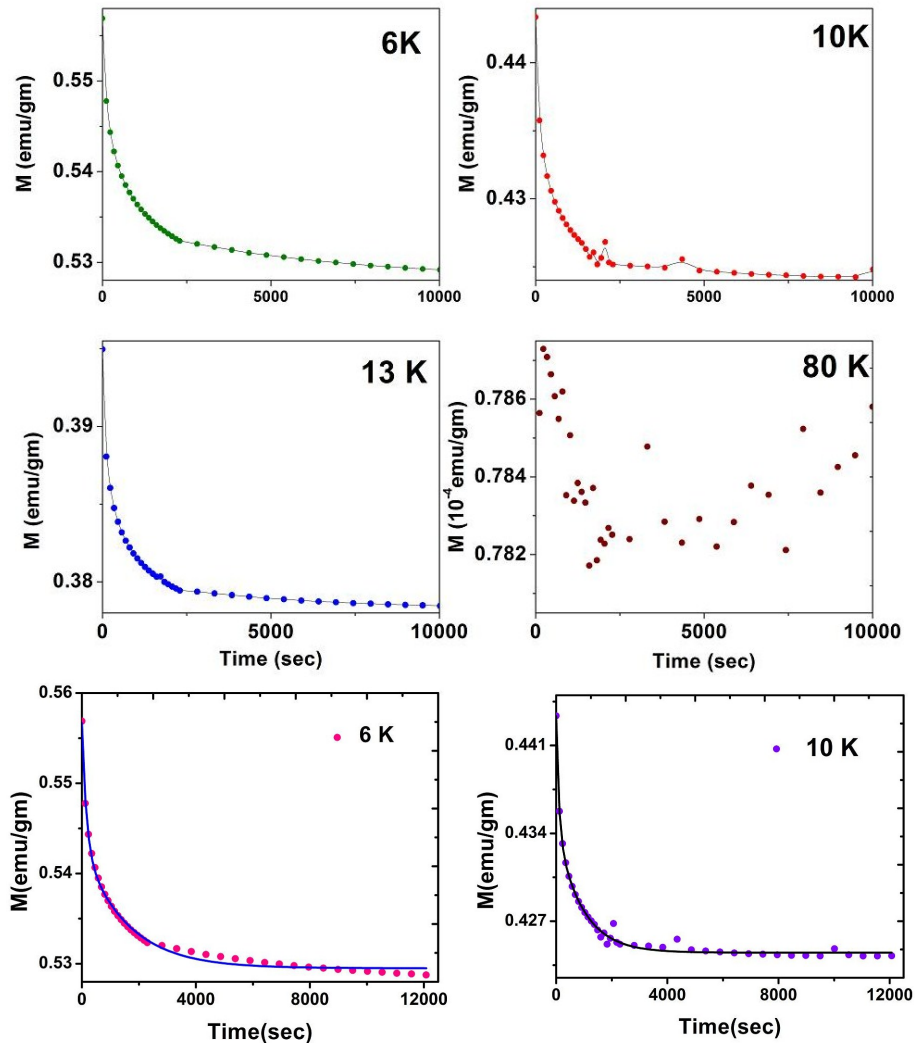


Figure 3.12: (Top panel) Relaxation of magnetization at different temperatures. (Bottom panel) Double exponential decay at 6 and 10 K.

spin-glass mixed phase at low temperatures.²

3.4 Conclusions

To conclude, the magnetization studies of both Ni-Fe-Mo and Ni-Fe-W alloys have shown that with increasing Mo and W and decreasing Fe in the alloys, the T_C as well as the saturation magnetization M_s decrease indicating the presence of competing ferro- and antiferromagnetic interactions in these alloys. The M-H loops of all these alloys hardly show any hysteresis, which is similar to that of the parent composition, Ni80Fe20 permalloy. We find that one of the alloys with 13.5 at. % of Mo in the Ni-Fe-Mo series shows a low temperature mixed ferro-spin-glass phase. We did not find any such behavior in any of the Ni-Fe-W alloys. The absence of any complex magnetic phase in W alloys can very well be due to the lack of enough samples in the critical concentration region. Our experimental work has been supplemented by theoretical work from our group which predicts that there is a possibility of a spin-glass phase in case of Ni-Fe-Mo alloys as Fe boosts and Mo depletes the fragile moments of Ni creating frustrations in the system. But in case of Ni-Fe-W alloys for low Fe concentrations, not only does the frustration in the system decrease, but also Ni loses its moment, leaving hardly any scope for a spin-glass-like phase which demands competing magnetic interactions.

²This part of the chapter has been published in *J.Phys. Cond. Matt.* **23** (2011).

Chapter 4

Signature effects of spin clustering in Ni-Fe-Mo and Ni-Fe-W alloys

In this chapter, we shall continue our study of magnetization of the disordered Ni-Fe-Mo and Ni-Fe-W alloys and see the effect of Fe dilution on the magnetization of these alloys. In the previous chapter, we have discussed the magnetization behaviour of these alloys particularly at low-fields. Here we give a successful interpretation of the low-temperature and high-field magnetization data of these alloys. The spontaneous magnetization as a function of temperature is investigated for the alloys using superconducting quantum interference device magnetometry with a focus on the low- T behavior as well as the critical exponents associated with the magnetic phase transition. While the low- T magnetization is found to be well described by Blochs $T^{3/2}$ law, an extraordinary enhancement of the spin-wave parameter B and the reduced coefficient $B_{3/2}=BT_C^{3/2}$ are observed with increasing Fe dilution as compared to conventional 3d ferromagnets whereas the critical amplitudes are found to decrease systematically. Recent locally self-consistent calculations of finite-temperature spin dynamics in a generic diluted magnet provide an understanding in terms of two distinct energy scales associated with weakly coupled bulk spins in the ferromagnetic matrix and strongly coupled cluster spins. In view of similar behaviour observed in diluted magnetic semiconductors and other ferromagnetic alloys, it is proposed that these distinctive features corresponding to the three important temperature regimes provide macroscopic indicators of signature effects of spin clustering on magnetization behaviour in disordered ferromagnets. The theories used here for analysis are already

discussed in details in Chapter 1.¹

4.1 Introduction

The observation of several signatures of a spin-glass-like phase in dc magnetization and ac susceptibility studies of Ni-Fe-Mo and Ni-Fe-W alloys in the last chapter indicates presence of competing ferromagnetic and antiferromagnetic spin interactions, resulting in frustration-induced frozen spin configurations in spin clusters. Generally, a broad distribution of magnetic spin couplings would be expected corresponding to different separations and configurations resulting from the positional disorder of magnetically active Fe atoms in these alloys.

Are there any distinctive finite-temperature spin dynamics effects associated with this disorder-induced distribution of magnetic interactions in the Ni-Fe-Mo and Ni-Fe-W alloys which are observable in their macroscopic magnetization behaviour? A similar question was recently addressed in the context of squid magnetization studies [112] of diluted magnetic semiconductors $\text{Ga}_{1-x}\text{Mn}_x\text{As}$, which also exhibit strong disorder effects due to Mn positional disorder. Recent theoretical studies of finite-temperature local spin dynamics within a generic model for diluted magnets have provided fundamental understanding of macroscopic magnetization characteristics in terms of microscopic spin disorder, spin clustering, and distribution of spin couplings. [113–115]

There are three important temperature regimes in the magnetization behaviour of a generic disordered ferromagnet. The low-temperature regime characterized by the spin-wave parameter, the intermediate-temperature regime nearly upto T_C characterized by the overall shape of the magnetization decay, and the critical regime very close to T_C involving critical fluctuations, divergent spin correlation length, and characterized by the critical exponents and critical amplitudes. In this chapter we propose that the magnetization behaviours in all three temperature regimes actually provide macroscopic indicators of signature effects associated with microscopic spin dynamics of weakly coupled bulk spins and strongly coupled cluster spins. For that purpose we have made a detailed study of the temperature dependence of magnetization in Ni-Fe-Mo and Ni-Fe-W alloys and the

¹The content of this chapter has been communicated to J. Phys. Comd. Mat (2011).

critical exponents and critical amplitudes associated with the phase transition.

4.2 Low-temperature high-field magnetization of the alloys

In conventional ferromagnets, the temperature dependence of the spontaneous magnetization $M_s(T)$ far below T_C is dominated by long-wavelength spin-wave excitations. The excitation energy $E(k)$ of spin waves in the limit of small wave vectors ($k \ll a^{-1}$, a is the lattice spacing) is given by

$$E(k) = \hbar\omega(k) = g\mu_B H_{\text{int}} + Dk^2 + Ek^4 + \dots, \quad (4.1)$$

where the first term is an energy gap due to the presence of an effective internal field H_{int} , arising from the applied field, the anisotropy field, and the spin-wave demagnetizing field. D is the spin-wave stiffness constant, and E is a proportionality constant. Even in disordered ferromagnets, there is ample experimental evidence that long-wavelength spin-wave modes are a useful way to represent the low-energy magnetic excitations [116].

In the low-temperature limit, according to the Heisenberg model, the change in the spontaneous magnetization due to the excitation of spin waves can be written as: [117]

$$\begin{aligned} M(T) &= M(0) \left[1 - Bz \left(\frac{3}{2}, \frac{T_g}{T} \right) T^{3/2} \right. \\ &\quad \left. - Cz \left(\frac{5}{2}, \frac{T_g}{T} \right) T^{5/2} + \dots \right], \end{aligned} \quad (4.2)$$

where $M(0)$ is the magnetization at 0 K, $T_g = g\mu_B H_{\text{int}}/k_B$ is the gap temperature, and $z \left(\frac{3}{2}, \frac{T_g}{T} \right)$ and $z \left(\frac{5}{2}, \frac{T_g}{T} \right)$ are the correction terms which reduce to unity if the effective internal magnetic field vanishes. The two temperature terms above come from the harmonic (k^2) and anharmonic (k^4) terms in the spin-wave dispersion relation [Eq. (4.1)]. For simplicity, disregarding anharmonicity and the gap corrections, Eq. (4.2) reduces to the so-called Bloch's $T^{3/2}$ law:

$$M(T) = M(0)(1 - BT^{3/2}). \quad (4.3)$$

In conventional spin-wave theory the spin wave parameter B and the spin wave stiffness coefficient D are related through

$$D = \frac{k_B}{4\pi} \left(\frac{2.612 g\mu_B}{M(0)B} \right)^{2/3}. \quad (4.4)$$

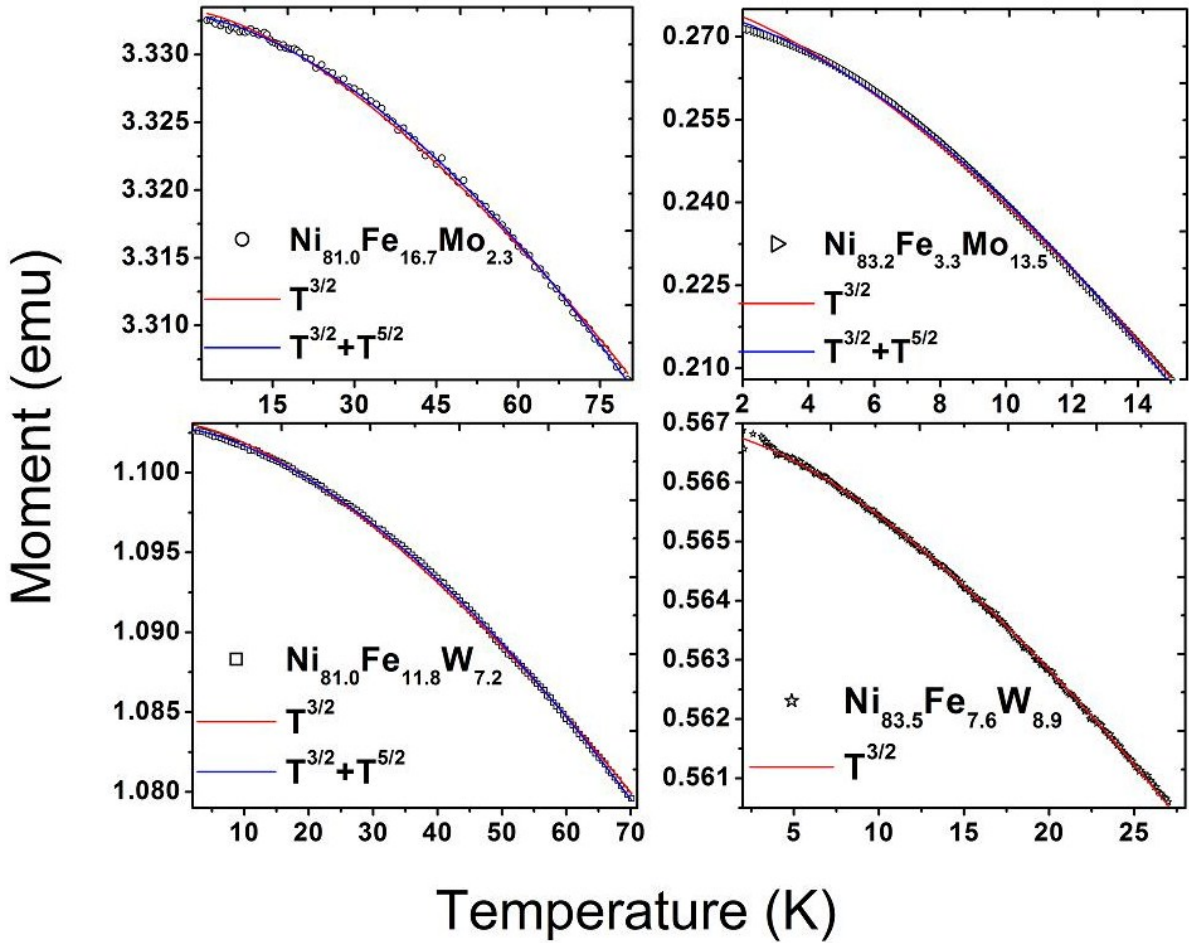


Figure 4.1: Magnetisation vs. Temperature plot for four samples are given, among them three samples fit better using Eq. (4.2) including anharmonic term another one shown fitted to Blochs $T^{3/2}$ law.

The thermal demagnetization process of ferromagnetic metals at low temperatures ($T \ll T_C$) can be explained by both localized [118] and itinerant [119] models. In the localized model, with static interactions between spins associated with localized electrons on atomic sites, spin waves correspond to coherent superposition of local spin deviations in the ferromagnetic state, and their equilibrium number density at finite temperature according to the Bose-Einstein distribution function yields the magnetization reduction according to Eq. (4.2). In the itinerant model, electrons move in the average field of other electrons/ions, and effective inter-site spin couplings are generated by exchange of

Table 4.1: Magnetization vs. temperature data are fitted to Eq. (4.2) and the coefficients B , C along with normalized χ^2 , R^2 , T_C , and D are tabulated below.

Sample Composition	$M(0)$ (emu)	B ($10^{-4} \text{ K}^{-3/2}$)	C ($10^{-6} \text{ K}^{-5/2}$)	$B_{3/2}$	T_C (K)	normalized χ^2 (10^{-7})	R^2	D meV \AA^2
$\text{Ni}_{81.0}\text{Fe}_{16.7}\text{Mo}_{2.3}$	3.33323 ± 0.00005	0.1189 ± 0.0004	-	0.23	720	0.099	0.99843	219
	3.33286 ± 0.00004	0.094 ± 0.001	0.023 ± 0.001			0.036	0.99941	
$\text{Ni}_{80.4}\text{Fe}_{12.9}\text{Mo}_{6.7}$	1.4606 ± 0.0002	0.294 ± 0.005	-	0.32	495	2.91	0.97166	144
	1.4601 ± 0.0003	0.24 ± 0.03	0.1 ± 0.06			0.036	0.99941	
$\text{Ni}_{83.4}\text{Fe}_{10.7}\text{Mo}_{5.9}$	0.79083 ± 0.00006	0.345 ± 0.003	-	0.35	470	2.08	0.99064	155
	0.79038 ± 0.00007	0.24 ± 0.01	0.19 ± 0.02			1.28	0.99439	
$\text{Ni}_{83.5}\text{Fe}_{7.6}\text{Mo}_{8.9}$	3.13870 ± 0.00002	0.864 ± 0.007	-	0.49	320	3.31	0.99981	110
$\text{Ni}_{83.1}\text{Fe}_{6.0}\text{Mo}_{10.9}$	1.20957 ± 0.00005	3.68 ± 0.01	-	0.90	182	0.75	0.99916	45
$\text{Ni}_{83.2}\text{Fe}_{3.3}\text{Mo}_{13.5}$	0.2770 ± 0.0001	42.7 ± 0.1	-	1.29	45	63.9	0.99871	20
	0.2755 ± 0.0001	36.2 ± 0.5	0.44 ± 0.03			27.7	0.99944	
$\text{Ni}_{78.9}\text{Fe}_{18.1}\text{W}_{3.0}$	4.0269 ± 0.0001	0.0982 ± 0.0007	-	0.21	775	0.52	0.99332	255
$\text{Ni}_{79.4}\text{Fe}_{14.1}\text{W}_{6.5}$	1.25119 ± 0.00002	0.302 ± 0.001	-	0.37	530	0.15	0.99945	133
	1.25098 ± 0.00002	0.275 ± 0.002	0.040 ± 0.002			0.07	0.99976	
$\text{Ni}_{81.0}\text{Fe}_{11.8}\text{W}_{7.2}$	1.10312 ± 0.00002	0.359 ± 0.001	-	0.42	515	0.31	0.99921	137
	1.10280 ± 0.00001	0.311 ± 0.002	0.070 ± 0.002			0.04	0.9999	
$\text{Ni}_{83.5}\text{Fe}_{7.6}\text{W}_{8.9}$	0.56687 ± 0.00001	0.796 ± 0.001	-	0.41	300	0.47	0.99956	120
$\text{Ni}_{82.6}\text{Fe}_{6.9}\text{W}_{10.5}$	1.66087 ± 0.00003	2.906 ± 0.004	-	0.77	191	0.22	0.99963	53
$\text{Ni}_{86.6}\text{Fe}_{3.1}\text{W}_{10.3}$	0.54141 ± 0.00001	19.6 ± 0.1	-	0.8	55	18.08	0.99825	28

the particle-hole propagator, strong correlation effects in which have been investigated recently using a systematic non-perturbative expansion scheme. [120] The presence of thermally excited long wavelength spin waves in the ferromagnetic state at low temperature allows virtual excitation of majority-spin electrons to the minority-spin band due to electron-magnon coupling, resulting in spectral-weight transfer and consequent reduction of the magnetization $\langle n_{\uparrow} \rangle - \langle n_{\downarrow} \rangle$.

The low-temperature magnetization was measured from 2 K to $0.1 T_C$ or till 15 K at ~ 6000 Oe for all the samples which is above their saturation fields of 1000-2000 Oe, although sample Mo13.5 did not actually saturate even at 6000 Oe due to its low-temperature mixed ferro-spin-glass phase. Figure 1 is a plot of M vs. T for $T \ll T_C$. The solid lines are the best-fitted curves as indicated in the legends of the figures. The gap correction [Eq. (4.2)] was tried but it was found to be negligible since the gap temperature came out to be less than 1 K.

From Fig.(4.1) as well as Table 5.1 we find that the fits for some of the 12 samples that we have studied improve significantly if we include the $T^{5/2}$ term in Eq. (4.2). Not only the values of χ^2 are smaller by a factor of 2-3 (~ 8 for W7.2), the deviation of the best-fitted curve from the data vs. T is random as against systematic when we consider only the $T^{3/2}$ term. For the other samples the improvements are insignificant. We must note that for higher T_C samples (low Mo and W), $\Delta M/M$ is only 1% and only very high resolution SQUID measurements are able to isolate the anharmonic term in the magnon dispersion relation.

The *first* significant feature emerging from the present investigation is the order of magnitude of the spin-wave parameter B . These values are found to be strongly enhanced with increasing Fe dilution in both the series of alloys, and are about 10 to 100 times larger than those found for conventional 3d ferromagnets (for bulk Fe it is $3.4 \times 10^{-6} \text{ K}^{-3/2}$). This sharp increase in the values of B with increasing Fe dilution reflects an enhancement in the density of low-energy magnetic excitations due to weakening of the ferromagnetic couplings between the bulk Fe spins forming the percolating ferromagnetic matrix. The spin-wave stiffness constants are also correspondingly reduced, as seen in Table 5.1.

4.3 Intermediate-temperature behaviour

In order to allow a qualitative comparison between the magnetization behaviour of different ferromagnetic systems over a much broader temperature scale extending nearly upto T_C , it is convenient to use the normalized coefficient $B_{3/2}$ defined through the relation: [121, 122]

$$\frac{M_s(0) - M_s(T)}{M_s(0)} = B_{3/2} \left(\frac{T}{T_C} \right)^{3/2} \quad (4.5)$$

in terms of the low-temperature magnetization (Eq. 4.3), which yields $B_{3/2} = BT_C^{3/2}$. Significantly, this reduced coefficient $B_{3/2}$ provides an effective measure of the overall shape of the magnetization decay. For crystalline ferromagnets, where the magnetization falls sharply near T_C , one obtains $B_{3/2} \approx 0.2$, irrespective of the Curie temperature. On the other hand, for reference, if the magnetization were to fall off as $M(0)(1 - BT^{3/2})$ nearly upto T_C , then clearly $B_{3/2} \approx 1$. Table 5.1 shows that with increasing Fe dilution, the $B_{3/2}$ values for both series of alloys systematically increase from ~ 0.2 to ~ 1 , indicating that the magnetization decay near T_C becomes significantly slower in the Fe-poor alloys. This is the *second* significant result which emerges from the intermediate-temperature regime.

Both these distinctive features of macroscopic magnetization behaviour observed in Ni-Fe-Mo and Ni-Fe-W alloys — strong enhancement of B with increasing Fe dilution and $B_{3/2}$ approaching unity — have also been observed in squid magnetization studies of diluted magnetic semiconductors $\text{Ga}_{1-x}\text{Mn}_x\text{As}$ [112], where they were ascribed to two distinct energy scales involved in the local spin dynamics associated with the formation of spin clusters. A brief review of the theoretical analysis of finite-temperature spin dynamics within a minimal model for diluted magnets will be helpful in understanding the observed magnetization behaviour.

Theoretical investigations in diluted magnets do yield competing ferromagnetic and antiferromagnetic interactions [122]. Within a minimal model for diluted magnets involving spin- S localized impurity spins and host band fermions (carriers), magnetic interactions between two impurity spins at lattice sites i and j were calculated from $J_{ij} = J^2(2S)\phi_{ij}$ in terms of the particle-hole propagator ϕ_{ij} evaluated in the ferromagnetic state. For the same impurity separation, the calculated magnetic couplings were found to exhibit a

broad distribution, implying that the coupling between two impurity spins is not simply a function of their separation, but actually depends on the whole disorder configuration, suggesting shades of a complex system.

The broad distribution in the calculated ferromagnetic spin couplings was ascribed to the formation of small impurity spin clusters due to positional magnetic disorder. The cluster spin couplings were found to be strongly enhanced due to preferential accumulation of carriers in impurity spin clusters, whereas the consequent depletion of carriers from the bulk resulted in weakened bulk spin couplings between the bulk spins forming the ferromagnetic matrix. [113–115]

The effects of such a broad distribution of ferromagnetic spin couplings on finite temperature spin dynamics was recently investigated in diluted magnets using a locally self-consistent magnon renormalization scheme, [113–115] in analogy with renormalized spin-wave theory in ordered ferromagnets. [123] The local magnetization $\langle S_i^z \rangle$ of each individual impurity spin at site i in a quantum spin- S disordered ferromagnet was obtained by self-consistently solving the three coupled equations:

$$\langle S_i^z \rangle = \frac{(S - \Phi_i)(1 + \Phi_i)^{2S+1} + (S + 1 + \Phi_i)\Phi_i^{2S+1}}{(1 + \Phi_i)^{2S+1} - \Phi_i^{2S+1}}, \quad (4.6)$$

where the local site-dependent boson occupation numbers:

$$\Phi_i = \sum_l \frac{|\phi_l^i|^2}{e^{\beta\omega_l} - 1} \quad (4.7)$$

in terms of the renormalized magnon energy eigenvalues ω_l and eigenfunctions ϕ_l obtained from the renormalized magnon Hamiltonian:

$$\mathcal{H}_{ij} = \sqrt{2\langle S_i^z \rangle} (J^2[\chi^0]_{ij}) \sqrt{2\langle S_j^z \rangle}. \quad (4.8)$$

The locally self-consistent magnetization $\langle S_i^z \rangle$ thus obtained clearly showed rapid thermal demagnetization and nearly paramagnetic behaviour of the weakly coupled bulk (FM matrix) spins, whereas the strongly coupled cluster spins resist thermal demagnetization and thus prolong the magnetic order near T_C . The overall picture from the averaged magnetization was that while the ferromagnetic T_C was suppressed by positional-disorder-induced spin cluster formation, the magnetization decay was distinctly stretched near T_C .

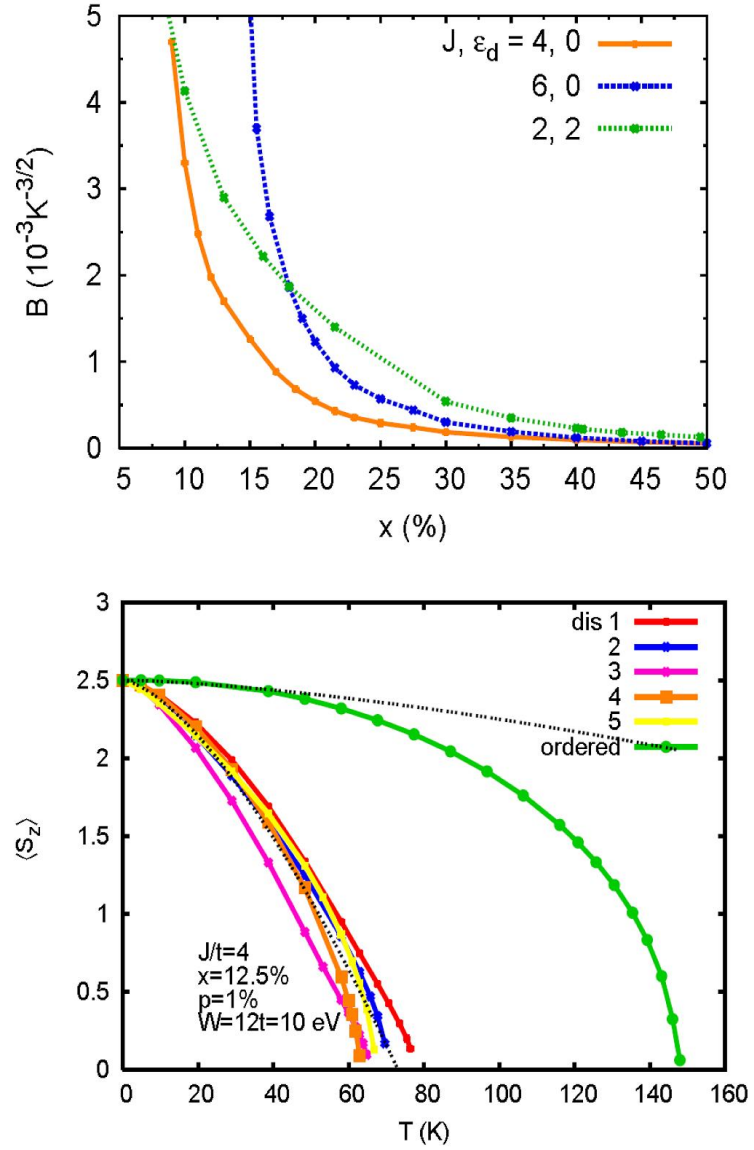


Figure 4.2: Rapid enhancement of the calculated spin-wave parameter B with dilution (upper panel), and (lower panel) nearly $T^{3/2}$ fall-off of site-averaged magnetization and stretching of magnetic order near T_C (from ref. [7]).

These distinctive features of microscopic spin dynamics behaviour in a generic diluted magnet were shown to quantitatively affect the two readily accessible characteristics B and $B_{3/2}$ of macroscopic magnetization behaviour. While the calculated spin-wave parameter B was found to be sharply enhanced with increasing dilution [Fig. 2 (upper panel)] due to weakened bulk spin couplings and softening of low-energy spin excitations, the stretching of magnetic order near T_C due to strongly coupled cluster spins resulted in enhanced $B_{3/2} \sim 1$, indicating slower thermal demagnetization approximately as $T^{3/2}$ (dashed line) over a much broader temperature range, as shown for five different disorder configurations (lower panel). In sharp contrast, the ordered ferromagnet yielded, for the same dilution and carrier concentration, a conventional magnetization decay with $B_{3/2} \approx 0.2$ and $T^{3/2}$ behaviour (dashed line) only in the low-temperature regime. Here the given notation refers to impurity concentration (x), carrier concentration (p), bandwidth (W), and host-impurity energy offset (ϵ_d).

As shown in Table 5.1, a very similar behaviour is obtained for the two magnetization (spin-wave) coefficients B and $B_{3/2}$ from our finite-temperature magnetization investigation of Ni-Fe-Mo and Ni-Fe-W alloys. While the B values are sharply enhanced with increasing Fe dilution (the spin stiffness is correspondingly sharply suppressed), the $B_{3/2}$ values approach 1 with increasing Fe dilution in both alloys, as compared to about 0.2 for ordered ferromagnets. Similar enhancements were reported recently from SQUID magnetization measurements on the diluted magnetic semiconductors $\text{Ga}_{1-x}\text{Mn}_x\text{As}$, [112] and in earlier studies on amorphous ferromagnetic alloys in comparison with crystalline ferromagnets [117, 118].

4.4 Magnetic phase transition and the associated critical exponents

We have also studied the critical exponents associated with the magnetic phase transition of the alloys containing more than 8 at.% of Mo/W. The specific reason to study the critical exponents and the amplitudes is to see the consistency of our findings with respect to the above magnetization data analysis. In the last section we have seen evidence of spin clusters with relatively strongly coupled spins in the alloys with dearth of Fe content. How

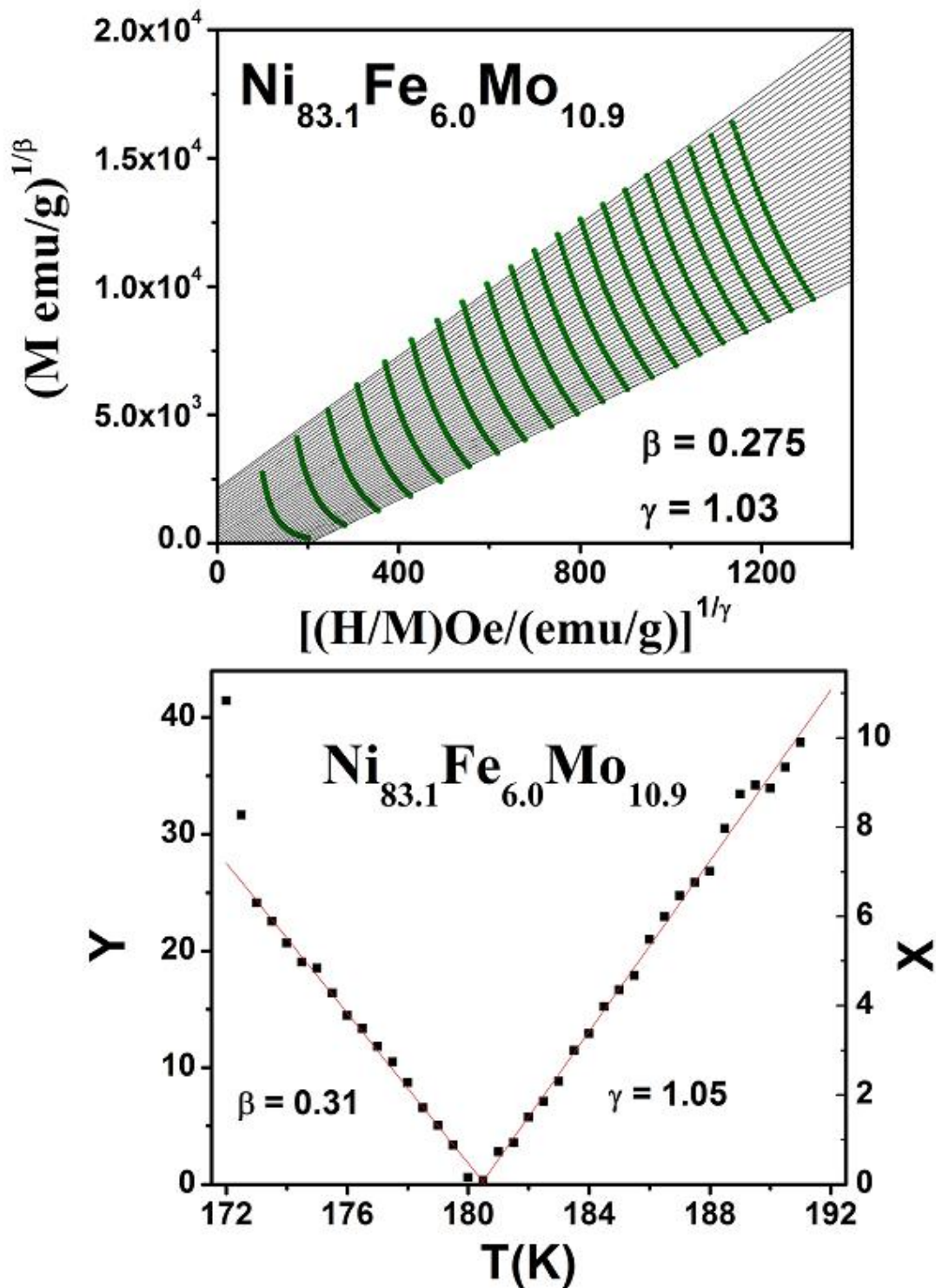


Figure 4.3: The modified Arrott-Noakes (AN) plot and $X(T)$ and $Y(T)$ vs. temperature plots for Mo10.9 alloy with values of β and γ for which the best-fitted isotherms are obtained.

does this spin clustering affect the critical exponents and critical amplitudes? As a first step, ac susceptibility has been measured in all alloys with a temperature increment of 0.2 K or less so that their T_C could be found accurately within ± 0.1 K. The magnetization was measured in fields ranging from 0 to 20 kOe at various temperatures around 2% of T_C on either side.

The critical exponent β associated with M_s , the spontaneous magnetization, is given by $M_s = B|\varepsilon|^\beta$ for $T < T_C$, where $\varepsilon = (T - T_C)/T_C$ and B is the corresponding critical amplitude. The critical exponent γ is related to χ_0 , the zero-field dc susceptibility, through the equation $\chi_0^{-1} = \Gamma^{-1}|\varepsilon|^\gamma$, where Γ^{-1} is the critical amplitude. The magnetic field dependence of M at T_C gives us the third critical exponent δ through the relation $M = DH^{1/\delta}$, D being the critical amplitude. All these three exponents follow a static scaling relationship, $\delta = 1 + \gamma/\beta$. In order to find these exponents one has to know the transition temperatures very accurately. First the isothermal magnetization M was plotted as in a simple Arrott plot (M^2 vs. H/M) which uses the mean-field exponents. However, when they did not give linear isotherms, the modified Arrott-Noakes (AN) plot was tried, i.e., $M^{1/\beta}$ versus $(H/M)^{1/\gamma}$.

To plot the AN isotherms one has to know the values of β and γ beforehand. Instead of guessing the initial values we have calculated β and γ using a simple FORTRAN code where we applied the method of least squares fitting. We have calculated the average chi-square (χ^2) for all possible combinations of β and γ , where β was varied between 0.2 and 0.6 in steps of 0.001 and γ from 0.9 to 1.5 in similar steps. Then the combination of β and γ , for which the average χ^2 is a minimum and the slopes of all the straight lines are almost equal, i.e., the set of isotherms are truly parallel to each other, are taken. Amazingly, the extrapolated isotherm at T_C indeed passes through the origin making us quite confident of the plots. Then using those values of β and γ we have plotted in Fig. 4.3 the modified Arrott-Noakes (AN) plot, a set of isotherms for 10 % Mo alloy, the y-intercepts of these straight lines give M_s and the x-intercepts χ_0^{-1} . Figure 4.3 (upper panel), a typical AN plot, also gives the values of β and γ for the best-fitted isotherms. Although γ is close to the mean-field value of 1, β is much lower than the mean-field value of 0.5. Deviations of the values of β and γ from the mean-field values have been found both in many magnetic glasses as well as in crystalline ferromagnets.

Table 4.2: Alloy compositions, values of T_C and critical exponents, obtained both experimentally and from KF analysis along with those for pure Ni and those from existing theories.

Sample Composition	T_C		β		γ		δ	
	Expt.	KF	Expt.	KF	Expt.	KF	Expt.	$1 + \frac{\beta}{\gamma}$
Ni _{83.5} Fe _{7.6} Mo _{8.9}	316.0	316.4	0.48	0.42	1.21	1.31	3.54	3.50
Ni _{83.1} Fe _{6.0} Mo _{10.9}	180.5	180.4	0.275	0.31	1.03	1.05	4.68	4.74
Ni _{83.2} Fe _{3.3} Mo _{13.5}	44.55	46.2	0.59	0.54	0.92	0.88	2.22	1.64
Ni _{83.5} Fe _{7.6} W _{8.9}	305.0	300.0	0.43	0.45	1.30	1.37	4.22	4.05
Ni _{82.6} Fe _{6.9} W _{10.5}	191.0	190.0	0.34	0.39	1.23	1.19	4.67	4.64
Ni _{86.6} Fe _{3.1} W _{10.3}	58.15	58.15	0.33	0.35	1.304	1.29	4.93	4.54
Ni ^a	627.4		0.378		1.34		4.58	
Mean-field			0.50		1.00		3.00	
3D-Ising			0.312		1.25		5.00	
3D-Heisenberg			0.378		1.405		4.76	

^a Reference [124].

There is another way of calculating β and γ , that is using the Kouvel-Fisher method. The set of equations used in this method are:

$$Y(T) = \left(\frac{d \ln M_s}{dT} \right)^{-1} = \left(\frac{1}{\beta} \right) (T - T_C) \quad (4.9)$$

and

$$X(T) = \left(\frac{d \ln \chi_0^{-1}}{dT} \right) = \left(\frac{1}{\gamma} \right) (T - T_C). \quad (4.10)$$

These equations are valid only in the critical region where temperatures are very near T_C . Here we have used the M_s and χ_0^{-1} values from the intercepts of the AN plots. In the critical region $Y(T)$ vs. T and $X(T)$ vs. T are both straight lines with slopes of $(1/\beta)$ and $(1/\gamma)$, respectively. In this method a priori knowledge of T_C is not needed and if the results are consistent, then $Y(T)$ and $X(T)$ will intersect the T axis at the same point. Figure 4.3 (lower panel) also shows the typical $X(T)$ and $Y(T)$ plots for 10 % Mo alloy. Both of them intersect the T -axis at $T = T_C = 180.5$ K.

We have used both the methods for all our samples to check the consistency of the results. Except for Mo13.5 alloy, all the other samples gave quite reasonable values of

the critical exponents. However, it is to be noted that unlike other alloys, Mo13.5 has a reentrant spin-glass phase (RSG) phase below $T_g=10$ K (T_C is ~ 44 K) which might possibly affect the critical behavior since the transition may not be a pure ferro-para one although we used $M(T, H)$ data only from $T=43-45$ K, far away from 10 K. Nevertheless, our calculated values of the critical exponents from the two methods did not match at all. More importantly, the value of β was above and that of γ was below the mean-field values. This is quite unphysical as the mean-field case is the limiting one, since it is a rather crude theory. Presence of more than one phase due to improper homogenization and/or final annealing might cause such deviations in the critical exponents. Table 5.2 below gives the values of T_C , β , γ , and δ . The critical exponent values suggest that Mo8.9 and W8.9 almost follow the mean-field model whereas the others, except Mo13.5 are close to 3D-Ising rather than that of pure nickel, which follows the 3D-Heisenberg model.

We have also calculated the critical amplitudes since they are important for a complete knowledge of the critical behavior near ferro-para transition. The magnetization above and below T_C satisfies a single scaling equation given by $m=f_{\pm}(h)$ where $m=|\varepsilon|^{-\beta}M(\varepsilon, H)$ and $h=|\varepsilon|^{-\beta\delta}H$ are called scaled magnetization and the scaled magnetic field. The above relations show that m as a function of h falls on two different universal curves $f_-(h)$ for $T<T_C$ and $f_+(h)$ for $T>T_C$. If the values of the critical exponents found here are correct, then all the data will fall on two distinct curves confirming their correct choice.

Table 4.3: The critical amplitudes of the alloys and those of Ni for comparison.

Sample composition	Γ^{-1} (kOe-g/emu)	B_0 (emu/g)	D_0
Ni _{83.5} Fe _{7.6} Mo _{8.9}	8.4	21.4	7.36
Ni _{83.1} Fe _{6.0} Mo _{10.9}	4.2	20.0	5.14
Ni _{83.2} Fe _{3.3} Mo _{13.5}	1.7	2.5	1.9
Ni _{83.5} Fe _{7.6} W _{8.9}	8.7	27.2	7.27
Ni _{82.6} Fe _{6.9} W _{10.5}	6.1	25.9	5.13
Ni _{86.6} Fe _{3.1} W _{10.3}	4.6	8.8	4.79
Ni ^a	19	83	30

^a Reference [124].

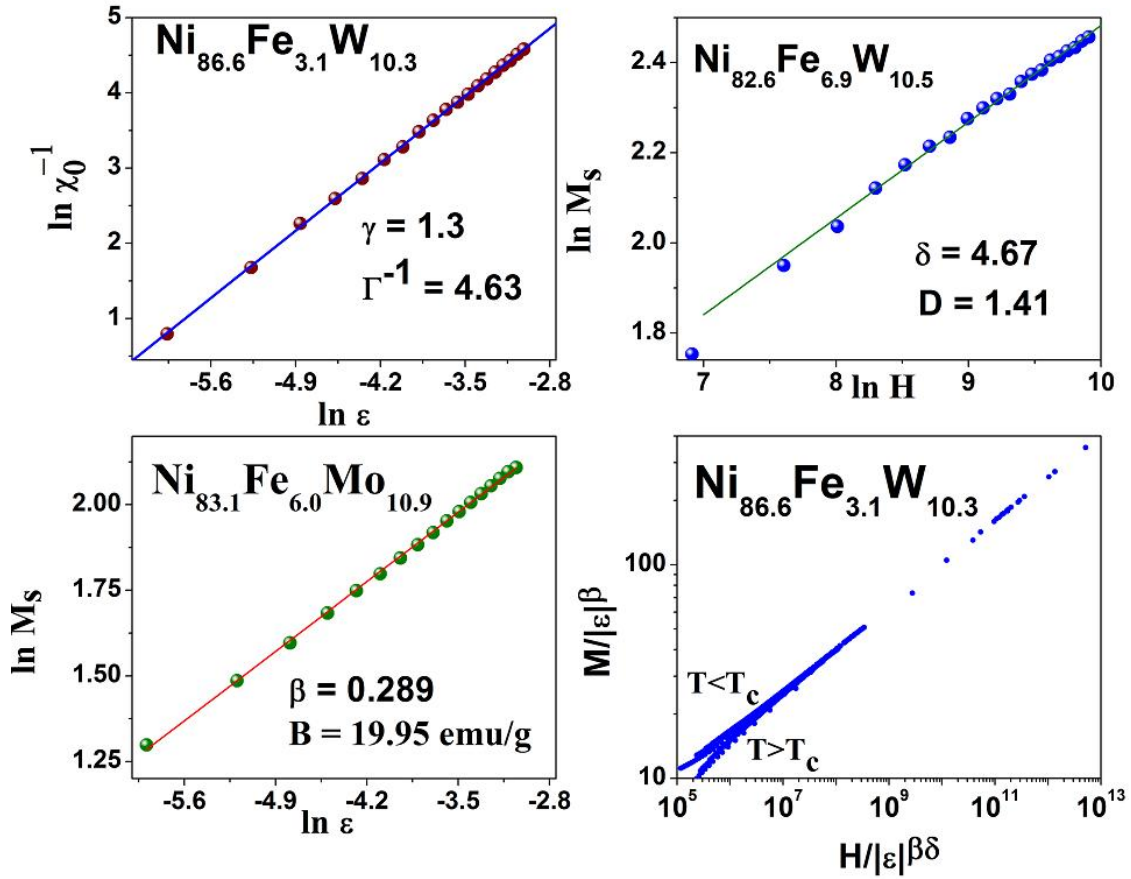


Figure 4.4: χ_0^{-1} vs. $\ln \varepsilon$ plot for W10.3 alloy, $\ln M_s$ vs. $\ln H$ plot for W10.5 alloy, $\ln M_s$ vs. $\ln \varepsilon$ plot for Mo10.9 alloy and $M/|\varepsilon|^\beta$ vs. $H/|\varepsilon|^{\beta\delta}$ plot for W10.3 alloy.

The critical amplitudes $B_0=m_0$, $\Gamma^{-1}=h_0/m_0$ and D_0 are obtained from the intercepts of the ln-ln plot of M_s vs. $|\varepsilon|$, χ_0^{-1} vs. $|\varepsilon|$ and M vs. $H(\varepsilon = 0)$, respectively. Figure 4.4 shows, respectively $\ln \chi_0^{-1}$ vs. $\ln \varepsilon$ plot for W10.3, $\ln M_s$ vs. $\ln H$ for W10.5, $\ln M_s$ vs. $\ln \varepsilon$ for Mo10.9, and $M/|\varepsilon|^\beta$ vs. $H/|\varepsilon|^{\beta\delta}$ for W10.3 including the calculated values of the corresponding critical amplitudes. Figure 4.4 (lower right panel) shows clearly the correctness of our procedure. Table 5.3 gives the critical amplitudes of some of the samples. We observe that with the increasing Fe dilution, the critical amplitudes Γ^{-1} , B_0 , and D_0 decrease systematically and all three have values lower than those for Ni. This is the *third* observable consequence of strongly coupled cluster spins, indicating significantly reduced participation by the bulk spins forming the ferromagnetic matrix in the critical

behaviour.

The locally self-consistent spin dynamics analysis shows that as the temperature falls below T_C , the cluster spins rapidly get magnetized. [113–115] A similar behaviour is expected above T_C in an external magnetic field. Thus, the cluster spins contribute dominantly to the high magnetic susceptibility of the alloys near T_C , and hence result in a suppression of χ_0^{-1} and of the critical amplitudes.

Particularly for the Mo13.5 sample, the extremely low measured values of critical amplitudes along with the unusual critical exponent values (see Table 5.2) indicates dominant finite-cluster contribution just below the percolation threshold, with no diverging spin correlation length and no true critical behaviour. This is consistent with the emergence of spin-glass behaviour at this composition due to frustrated cluster spins locked in frozen non-collinear orientations which also results in smaller spontaneous magnetization along the z-direction.

4.5 Conclusion

In conclusion, we find that all three macroscopic magnetization characteristics — the spin-wave parameter B , the reduced coefficient $B_{3/2}$, and the critical amplitudes Γ^{-1} — corresponding to the low, intermediate, and the critical temperature regimes respectively, yield distinctive spin dynamics signatures associated with strongly coupled cluster spins in these alloys.

The dilution behaviour of the two magnetization coefficients extracted from the macroscopic magnetization behaviour of finite-temperature spin dynamics in the two alloy systems is indicative of a broad distribution of magnetic spin interactions between the magnetically active Fe atoms. The sharp enhancement in the measured spin-wave parameter B accompanying the spin stiffness reduction with Fe dilution clearly indicates weakened bulk spin couplings and softening of low-energy spin-wave modes. Furthermore, the magnitude of the reduced coefficient $B_{3/2}$ rapidly approaches 1 with increasing Fe dilution, and the slower magnetization decay with temperature indicates presence of strongly coupled cluster spins which resist thermal demagnetization and stretch the magnetic order near T_C .

As also observed in diluted magnetic semiconductors and metallic glasses, this sharp enhancement with dilution is thus suggestive of the two magnetization coefficients as universal macroscopic indicators of spin clustering and disorder-induced distribution of magnetic interactions in disordered ferromagnets. The reduction of the measured critical amplitudes with Fe dilution due to significantly reduced participation by the bulk spins forming the ferromagnetic matrix in the critical behaviour is consistent with this picture. Similar suppression of critical amplitudes was observed in $\text{Fe}_x\text{Ni}_{80-x}\text{P}_{14}\text{B}_6$ alloys, [125] and was ascribed to the growth of spin clusters as T approaches T_C and the consequent reduced participation of remaining bulk (FM matrix) spins in the FM-PM phase transition.

Except for the Mo13.5 alloy, which has a spin-glass phase below $T_g = 10$ K, all the other samples gave quite reasonable values of the critical exponents. Non-universal values of critical exponents with $\beta \approx 0.55$ have also been found in recent experimental studies [126] of the ferromagnetic transition in re-entrant metallic spin-glass alloys such as $\text{Au}_{0.81}\text{Fe}_{0.19}$.

Chapter 5

Electrical transport properties of a few disordered systems

In this chapter, we present successful interpretations of the electrical resistivity for a few disordered systems. The electrical resistivity as a function of temperature and magnetic fields has been investigated for a number of disordered Ni-Fe-V, Ni-Fe-Mo, and Ni-Fe-W alloys, a set of Co-rich pseudo-binary Ni-Cr ferromagnetic metallic glasses, and PLD grown self assembled Ni-nanocrystallites using the standard four-probe method. We have focused on the different scattering processes involved in the electrical transport and finally isolated them with a careful data analysis. The observed low-temperature resistivity minima in these systems, unaffected by higher fields (~ 5 T), rule out the Kondo effect as a possible source. Instead they are due to electron - electron interactions often found in similar disordered systems with high electrical resistivity. Enhancements of electron - magnon and electron - electron scattering strength have been observed with Fe dilution in disordered Ni-Fe-Mo/W alloys. The electrical resistivity of the ferromagnetic amorphous alloys show a clear T^2 dependence well above T_C coming from both dynamical structural factor as well as coherent electron - magnon scattering instead of $T^{3/2}$, which comes from the incoherent electron - magnon scatterings. In case of Ni-nanocrystallites, the electrical resistivity well above T_{min} is interpreted in terms of electron-phonon and electron-magnon scattering. It is found that the temperature dependence of the composite Ni/TiN sample mainly comes from that of Ni and the residual resistivity from TiN. All these and a few more issues will be addressed in the following sections. The details of the theories used here have already been discussed in Chapter 1.

5.1 Introduction

The electrical resistivity gives detailed insight into the various scattering processes in materials. The disordered alloys are interesting in this regard as they have many intriguing properties making them quite fascinating for further studies. Presence of 3d-transition metals in the alloys makes the problem more attractive as well as complicated. In the last few decades, Ni-rich disordered ternary alloys have been studied in great details for such reasons. In the last chapter, we have found that Ni-Fe-Mo and Ni-Fe-W alloys with increasing Fe dilution show signature effects of clustering on magnetization, like extraordinary enhancement of the spin-wave parameter, and reduction of critical amplitudes associated with magnetic phase transitions. Here also we will try to understand if that Fe-clustering has any effect on the resistivity of these alloys. Similarly, in metallic glasses the non-crystallinity of the material affects the electronic properties. The interpretation of the electrical resistivity data from low temperatures all the way up to room temperature is a formidable task for metallic glasses which are ferromagnetic and at the same time show low-temperature resistivity minima. The metallic glasses chosen for the present study is indeed one such system. Finally, magnetic nanocrystals show size-tunable magnetic properties [127]. It is thus important to study the electrical resistivity and the effect of magnetic state on it in such nanostructured systems. For that we have prepared, nanocrystalline nickel particles embedded in a metallic TiN matrix using the pulsed laser deposition technique. The sample consists of five alternate layers of self-assembled Ni nanoparticles and TiN, epitaxially grown on Si (100) substrate and an extra TiN layer on top of the nickel nanoparticles. The choice of TiN as the metallic matrix is due to the high chemical stability, hardness, unusually high electrical conductivity and its role as a diffusion barrier for the nickel atoms to the silicon wafer. The resistivity of these three different kinds of disordered systems will be discussed in the following sections in details.

5.2 Electrical Resistivity of the Disordered Ni-Fe-V, Ni-Fe-Mo and Ni-Fe-W Alloys

A four-probe DC method was used to measure the electrical resistivity using Quantum Design's PPMS. Data were taken at 100 mK interval or less in the temperature range

below resistivity minima (T_{\min}) and 500 mK or higher above. The resolution of the present measurements ($\Delta R/R$ where R is the resistance) is almost 10 - 20 parts per million and the temperature stability is 0.01 K or better depending on the range of temperature. However, the resolution of $\Delta\rho/\rho$ where ρ is the resistivity is only $\sim 6\%$ due to the uncertainty in the measurements of the dimensions of the samples. A maximum field of 5 T was applied during measurements.

The magnetic phase of the alloys is very important for the analysis of electrical transport data, more significantly when this class of alloys is reportedly having competing ferromagnetic and antiferromagnetic interactions and complex magnetic phases. The T_C for all the compositions are given in Table 5.1 along with many other relevant quantities which will be discussed later. It is clear from Table 5.1 that increasing V, Mo and W content in the alloys lowers the T_C while increment of Fe boosts ferromagnetism as expected.

The electrical resistivity has been measured from 2 - 300 K at 0 tesla (T) and 2-100 K at three other fields of 0.1, 1, and 5 T. All the samples, except V5.1 which shows resistivity minimum only at applied field ~ 5 T, show low temperature resistivity minima at all applied fields as observed in many similar disordered, the so-called dirty systems. Application of higher fields did not affect the minimum except a small increase of T_{\min} at 5 T and in some cases minor changes in DOM. Figure 5.1 shows a typical resistivity data, here for Mo10.9 alloy, and the inset shows the resistivity minima at different applied fields for V18 alloy. There can be two possible reasons for the minimum in the resistivity of the alloys, namely (i) Kondo effect and (ii) quantum interference effects. Kondo resistance minima [128] at low temperatures, where $\rho(T) \sim -\ln T$, originate from indirect interaction of the localized magnetic impurities, far apart from each other, by polarizing the conduction electrons. The T_{\min} and DOM depend on impurity concentration and the magnetic state of the alloys. Interestingly, Kondo minima disappear in magnetic fields. In highly disordered systems, the mean free path of the conduction electrons becomes smaller, resulting in non-classical Boltzmann trajectories. The conduction electrons diffuse from site to site by multiple elastic scattering [129]. This leads to phase coherence between the conduction electron partial waves which, in turn, enhances the probability for an electron to return to its starting point. This is known as electron localization resulting

Table 5.1: Alloy compositions, value of T_C , value of T_{min} at different applied fields and depth of minima (DOM= $[\rho(2K) - \rho(T_{min})]/\rho(T_{min})$) at 0 T and $\Delta\rho/\rho_{300}$ ($\Delta\rho = \rho_{300} - \rho(T_{min})$).

Alloy	T_C (K)	ρ_{2K} ($10^{-6}\Omega\text{ m}$)	T_{min} (K)	DOM (%)	$\Delta\rho/\rho_{300}$ (%)
Composition	(K)	($10^{-6}\Omega\text{ m}$)	(0 T) (1 T) (5 T)	(%)	(%)
Ni _{80.9} Fe ₁₄ V _{5.1}	640	0.64	-	0.05	16.5
Ni ₈₃ Fe ₁₀ V ₇	486	1.03	24 24	0.10	9.7
Ni _{76.5} Fe ₁₄ V _{9.5}	462	0.86	22 23	0.10	9.3
Ni ₇₉ Fe ₅ V ₁₆	62	1.36	21 21	0.16	4.5
Ni ₇₈ Fe ₄ V ₁₈	43	1.41	19 19	0.42	1.4
Ni _{83.5} Fe _{7.6} Mo _{8.9}	320	1.28	21 22	0.13	6.4
Ni _{83.1} Fe _{6.0} Mo _{10.9}	182	1.38	22 23	0.14	4.2
Ni _{83.2} Fe _{3.3} Mo _{13.5}	45	1.33	12.5 13	0.10	4.9
Ni _{83.5} Fe _{7.6} W _{8.9}	305	1.45	20 20	0.11	8.2
Ni _{82.6} Fe _{6.9} W _{10.5}	191	0.99	13 14	0.10	5.6
Ni _{86.6} Fe _{3.1} W _{10.3}	55	1.04	8 9	0.05	6.9

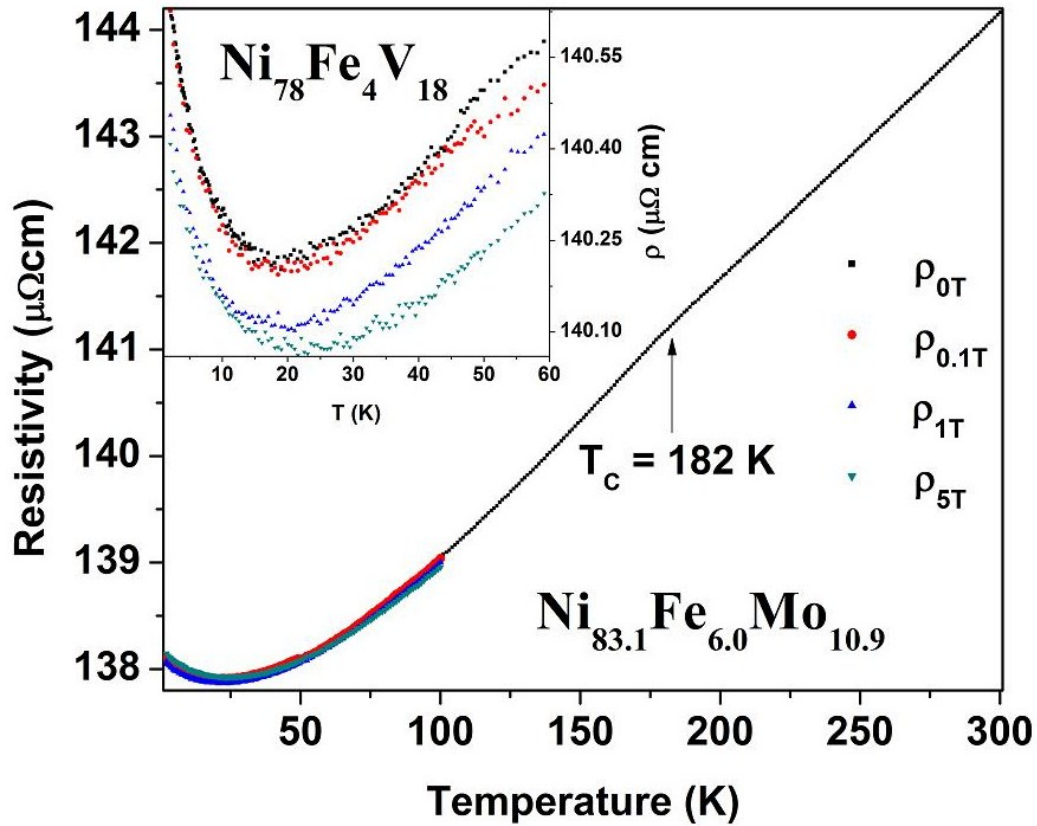


Figure 5.1: Resistivity is plotted against temperature from 2 to 300 K at four different applied fields for the $\text{Ni}_{83.1}\text{Fe}_{6.0}\text{Mo}_{10.9}$ alloy. The inset shows the low temperature resistivity minima at different applied fields for the $\text{Ni}_{78}\text{Fe}_4\text{V}_{18}$ alloy.

in a higher resistivity. Any inelastic process, like, electron-phonon, electron-magnon scattering or electron-electron interaction or the application of a magnetic field can destroy this phase coherence and hence reduces the resistivity. A minimum in resistivity occurs because there is ultimately an increase due to all inelastic processes as the temperature rises. According to Lee & Ramakrishnan [130], below the resistivity minimum $\rho(T) = -C\sqrt{T}$ due to electron-electron (ρ_{e-e}) interaction effects. In terms of conductivity it is $\sigma(T) = m_\sigma\sqrt{T}$ ($m_\sigma = C/\rho_0^2$). In case of the present alloys, the resistivity minima are ascribed to electron localization because high magnetic fields (5 T) left them almost unchanged.

In case of ferromagnetic metallic systems, there is a finite contribution to the resistivity

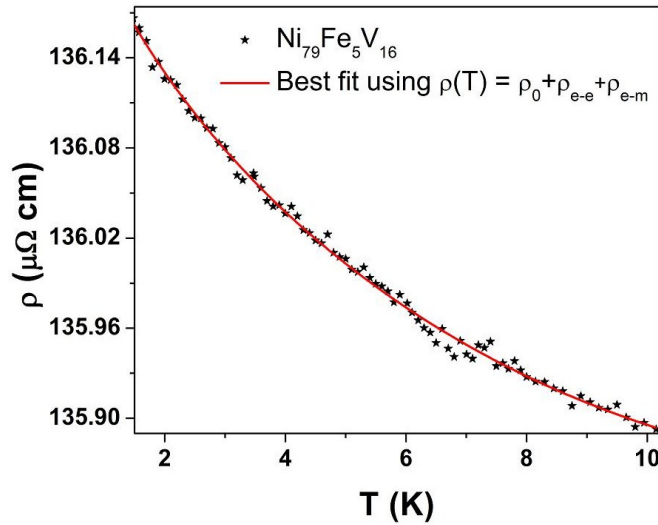


Figure 5.2: Zero field resistivity is plotted against temperature from 1.5 to 10 K for $\text{Ni}_{79}\text{Fe}_5\text{V}_{16}$ alloy. The solid line is the best fit of the data found using $\rho(T) = \rho_0 + \rho_{e-e} + \rho_{e-m}$.

(ρ_{e-m}) arising from the exchange interaction between the conduction s-electrons and the localized 3d-electrons, commonly known as s-d interaction. This spin disorder resistivity has been calculated [131–133] using more than one approach and found to be $\rho_{e-m} = B T^2$ for $T \leq 10$ K, where B includes the strength of the s-d interaction. The value of B calculated by Mannari [133] was in good agreement with the experimental data of White and Woods [134] on Ni below 10 K. With a not so pure sample as used by White & Woods, Kondorsky et al. [135] found that the T^2 gives a good fit even till 30 K. The above mentioned calculations only considered intraband s-s electron-magnon scattering. Later on it was extended by Goodings [136] with the inclusion of interband s-d electron-magnon scattering due to large d-band density of states at the Fermi level in these transition metal alloys. It was found that this interband s-d scattering is only dominant above 20 K and is an order of magnitude larger than that from the intraband s-s scattering. Direct comparison with experiments is a formidable task due to the rather complicated temperature dependence of the s-d scattering. Thus we conclude that magnetic scattering in 3d metal alloys is best interpreted at low temperatures. In crystalline alloys, be it magnetic or non-magnetic, scattering of conduction electrons by phonons contributes a significant

fraction of the electrical resistivity. In 3d magnetic metals and alloys, the s and d bands overlap at the Fermi level. So like magnetic scattering, in electron-phonon case as well, the conduction electrons might undergo s-s (intraband) and s-d (interband) transitions. The scattering of conduction electrons by lattice phonon gives the contribution [137]

$$\rho_l = A \left(\frac{T}{\theta_D} \right)^n \int_0^{\Theta_D/T} \frac{z^n dz}{(e^z - 1)(1 - e^{-z})}, \quad (5.1)$$

where Θ_D = Debye temperature and $n = 3$ (Bloch-Wilson) for magnetic metals and alloys with large d-band density of states giving rise to electron-phonon scattering involving s-d transitions.

Now keeping in mind the various scattering processes, we have analyzed the resistivity data of *eleven* alloys. The data below T_{min} are analyzed between 2 and 10 K to find out the electron-electron (\sqrt{T}) and electron-magnon (T^2) contributions to the resistivity, assuming that ρ_l is insignificant at such low temperatures. Figure 4.3 is a typical example of such a fitting till 10 K, the solid line giving the best fit. The electron-electron interaction term, $C \sim 10^{-10} \Omega \text{mK}^{-1/2}$, is of the same order as in similar types of high-resistivity alloys. Table 5.2 clearly shows that C increases with ρ_0 ; understandably increased disorder enhances e-e interaction effects. We have found, the coefficients C and B both decrease with increasing magnetic fields. Magnetic fields destroy the phase coherence of the localized electrons, hence the electron - electron interaction term decreases. Magnetic fields quench the magnons, hence electron-magnon interactions are considerably reduced. The magnon contribution or spin disorder resistivity in these concentrated high- ρ alloys, $B \sim 10^{-5} \mu\Omega \text{mK}^{-2}$, is an order of magnitude larger than that found in pure Ni [134] ($1.4 \times 10^{-5} \mu\Omega \text{cmK}^{-2}$). The poor values of R^2 in a few cases are due to very small changes in the resistivity showing up as large scattering in the data points. We have also seen in Table 5.2 that a decrease of Fe content in the alloys increases the strength of the electronmagnon (B) scattering. A similar kind of enhancement has been found in case of the electronelectron localization coefficient (C). A similar kind of sharp enhancement in the spin-wave parameter (B) was observed by us in the low- temperature magnetization and the reduced spin-wave parameter ($B_{3/2}$) steadily approached 1 in these Ni-Fe-Mo/W alloys (discussed in last Chapter). These are indicative of a broad distribution of magnetic spin

Table 5.2: Alloy compositions, values of ρ_0 , B, C, m_σ ($m_\sigma = C/\rho_0^2$), R^2 , and normalized χ^2 found from the fit of the data till 10 K using $\rho(T) = \rho_0 + \rho_{e-e} + \rho_{e-m}$.

Alloy	ρ_0 ($\mu\Omega$ cm)	B ($10^{-5}\mu\Omega$ cm/ K^2)	C ($10^{-2}\mu\Omega$ cm/ $K^{1/2}$)	m_σ (Ω cm/ $K^{1/2}$) $^{-1}$	R^2	normalized χ^2 (10^{-10})
Ni _{80.9} Fe ₁₄ V _{5.1}	63.73±0.01	5.2±0.4	0.7±0.2	1.7	0.94393	20
Ni ₈₃ Fe ₁₀ V ₇	102.59±0.01	7±3	3.2±0.1	3.0	0.85368	32
Ni _{76.5} Fe ₁₄ V _{9.5}	86.32±0.02	8±1	3.1±0.1	4.1	0.92308	19
Ni ₇₉ Fe ₅ V ₁₆	136.71±0.01	70±5	17.3±0.3	9.2	0.99662	11
Ni ₇₈ Fe ₄ V ₁₈	141.0±0.2	142±11	27.9±0.6	14	0.75361	21
Ni _{83.5} Fe _{7.6} Mo _{8.9}	128.46±0.01	3.0±0.3	6.5±0.3	4.0	0.75361	71
Ni _{83.1} Fe _{6.0} Mo _{10.9}	138.19±0.01	21±3	9.0±0.2	4.7	0.99999	3
Ni _{83.2} Fe _{3.3} Mo _{13.5}	132.82±0.01	107±12	12.4±0.7	7.0	0.93457	44
Ni _{83.5} Fe _{7.6} W _{8.9}	144.83±0.01	25±8	6.7±0.8	3.2	0.70476	162
Ni _{82.6} Fe _{6.9} W _{10.5}	99.67±0.01	28±4	5.8±0.2	5.9	0.98665	6
Ni _{86.6} Fe _{3.1} W _{10.3}	103.90±0.01	91±10	5.1±0.3	4.7	0.83391	38

interactions between the magnetically active Fe atoms as well as weakening of the bulk spin of Ni. Here also we believe that this sharp enhancement in the electron-magnon scattering with increasing Fe-dilution comes distinctively from the strongly coupled cluster spins.

The resistivity of NiFeV/Mo/W increases with the addition of V/Mo/W if Fe remains the same. This is exactly what happens in binary alloys for small concentrations at either end. If Fe content is diluted, the clusters of Fe spins break up into many strongly coupled smaller clusters serving as multiple scattering centers for the electrons, thereby increasing the resistivity. So as one goes from one composition to the next, both the contributions have to be properly taken into account. Several subtle conclusions may now be drawn from Table 5.2 above:

1. From alloy V5.1 to alloy V7, ρ_0 changes drastically from 64 to 103 $\mu\Omega\text{cm}$ because Fe is diluted and V is increased, both contributing to the increase in ρ_0 .
2. From alloy V7 to V9.5, ρ_0 changes from 103 to 86 $\mu\Omega\text{cm}$, Fe decreases ρ_0 and V increases it and there is an overall decrease of ρ_0 i.e., Fe dominated.
3. From alloy V5.1 to V9.5 only V increases by 4.4 % and so ρ_0 has increased from 64 to 86 $\mu\Omega\text{cm}$.
4. On the same token alloy V16 and V18 have nearly the same $\rho_0 = 137 \mu\Omega\text{cm}$ and 141 $\mu\Omega\text{cm}$ since their compositions are close by.
5. Similarly for Mo containing alloys Mo10.9 has a higher ρ_0 (138 $\mu\Omega\text{cm}$) than Mo8.9 (128 $\mu\Omega\text{cm}$) because of lower Fe and higher Mo. However, Mo13.5 should have still higher resistivity than Mo10.9 whereas it is only 133 $\mu\Omega\text{cm}$.
6. W-containing alloy W8.9 has a somewhat higher ρ_0 of 145 $\mu\Omega\text{cm}$ than that of the similar Mo alloy Mo8.9 (128 $\mu\Omega\text{cm}$) but those of W10.5 and W10.3 are comparatively on the much lower side $\sim 100 \mu\Omega\text{cm}$. This is difficult to understand. Finally we conclude that the resistivity of these bulk alloys can be more or less understood in terms of Fe and V/Mo/W concentrations. One must also remember that ρ_0 has an absolute error of ~ 6.5 % coming from geometrical factors.

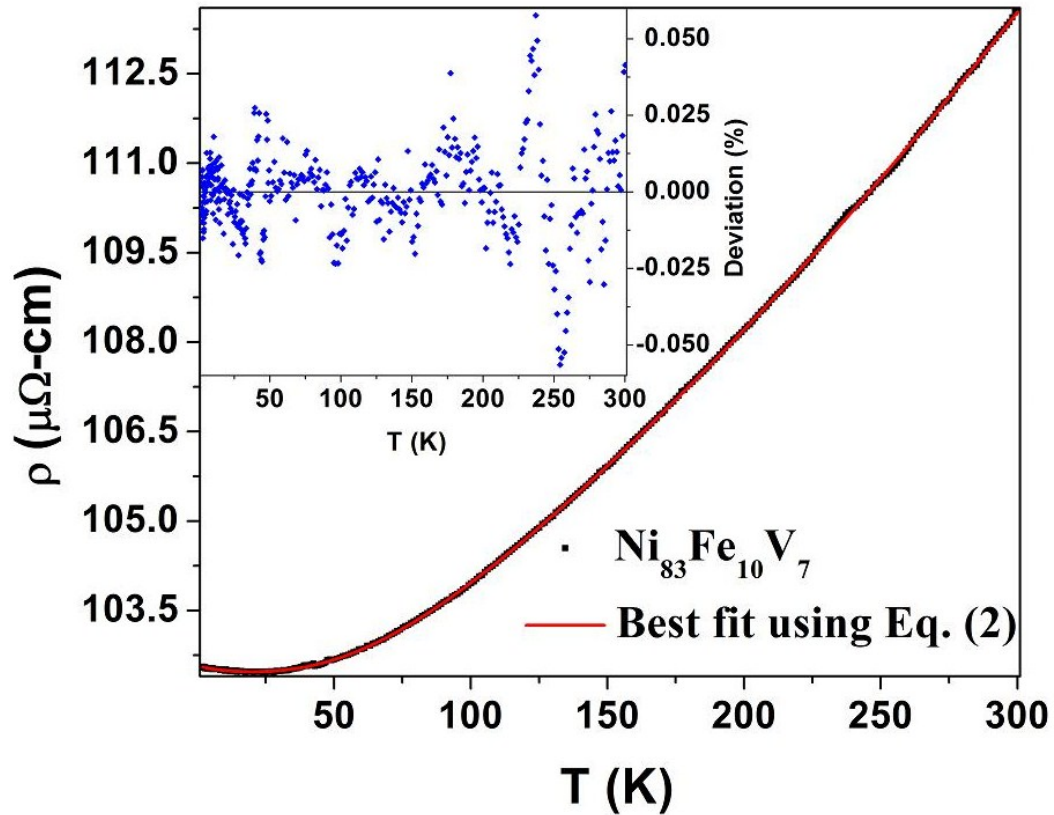


Figure 5.3: Zero field resistivity data against temperature have been plotted for (a) $\text{Ni}_{83}\text{Fe}_{10}\text{V}_7$ alloy. The solid lines give the best fit using Eq.(5.2). The inset inside shows the deviations of the respective fits.

At higher temperatures, depending on the respective T_C of the alloys, the resistivity data were fitted to

$$\rho(T) = \rho_0 + \rho_{e-e} + \rho_{e-m} + \rho_l, \quad (5.2)$$

or

$$\rho(T) = \rho_0 + \rho_{e-m} + \rho_l, \quad (5.3)$$

where ρ_0 is the residual resistivity, $\rho_{e-e} = -C\sqrt{T}$, $\rho_{e-m} = BT^2$, ρ_l is given by Eq.(5.1) as explained earlier. Above T_C , the data were fitted to only the ρ_l term since at higher temperatures ρ_{e-e} and ρ_{e-m} are not expected to be significant. Among the *eleven* samples reported here, *five* alloys have T_C above room temperature and we could get reasonably good fits for the whole range of temperature using Eq.(5.2). The fitting

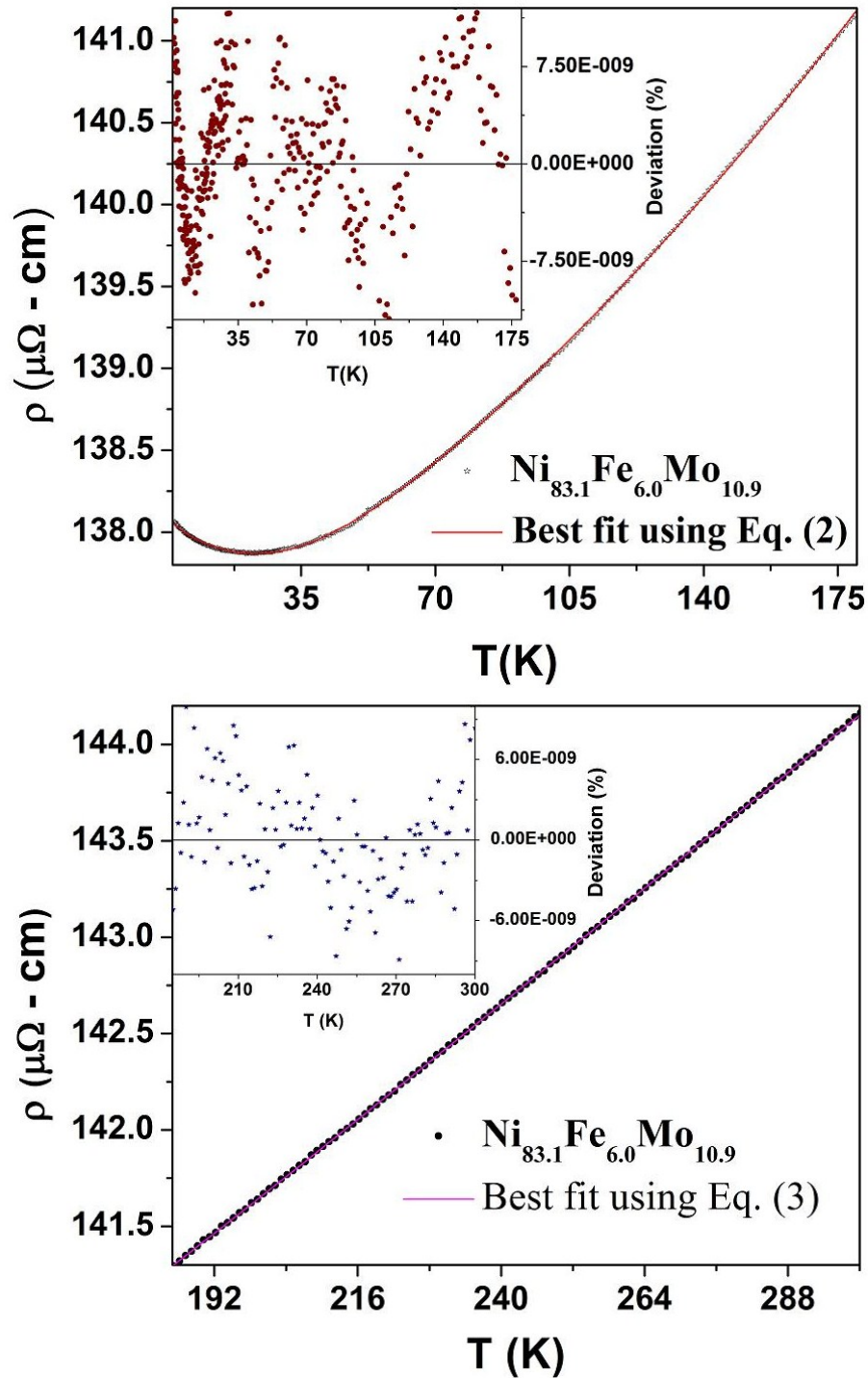


Figure 5.4: Zero field resistivity data against temperature have been plotted for $\text{Ni}_{83.1}\text{Fe}_{6.0}\text{Mo}_{10.9}$ alloy. The solid lines give the best fits (a) using Eq.(5.2) and (b) using Eq.(5.3). The insets inside (a), (b) show the deviations of the respective fits.

Table 5.3: Alloy compositions, values of A , Θ_D , B , C , R^2 , and normalized χ^2 found from the fits to Eq.(5.2) or Eq.(5.3)

Alloy	A ($\mu\Omega$ cm)	Θ_D (K)	B ($10^{-5}\mu\Omega$ cm/ K^2)	C ($10^{-2}\mu\Omega$ cm/ $K^{1/2}$)	R^2	normalized χ^2 (10^{-8})
Ni _{80.9} Fe ₁₄ V _{5.1}	17.5±0.5	449±7	6.3±0.1	-	0.999929	39
Ni ₈₃ Fe ₁₀ V ₇	22.7±0.2	468±3	5.5±0.1	3.8±0.1	0.999999	2.4
Ni _{76.5} Fe ₁₄ V _{9.5}	10.8±0.1	464±6	8.2±0.1	3.66±0.04	0.999999	2.3
Ni ₇₉ Fe ₅ V ₁₆	5.4±0.1	356±9	0.46±0.01	-	0.999999	4.8
Ni ₇₈ Fe ₄ V ₁₈	6.9±0.1	397±4	0.27±0.03	-	0.999999	1.0
Ni _{83.5} Fe _{7.6} Mo _{8.9}	18.0±0.3	401±3	3.8±0.1	5.4±0.2	0.999999	9.7
Ni _{83.1} Fe _{6.0} Mo _{10.9}	13.8±0.2	433±3	3.1±0.2	3.3±0.1	0.99999	0.01
Ni _{83.2} Fe _{3.3} Mo _{13.5}	9.5±0.2	361±5	2.6±0.4	-	0.999995	11
Ni _{83.5} Fe _{7.6} W _{8.9}	21.8±0.3	361±4	5.6±0.1	4.4±0.3	0.999999	7.7
Ni _{82.6} Fe _{6.9} W _{10.5}	10.5±0.1	423±2	2.8±0.1	2.5±0.4	0.999986	36
Ni _{86.6} Fe _{3.1} W _{10.3}	12.5±0.3	330±16	2.3±0.1	-	0.999999	15

parameters, listed in Table 5.3, match quite well with existing literature values on similar kinds of Ni-rich alloys [138]. The values of T_C for the remaining *six* alloys are well below room temperature. There are changes in the slope of the resistivity data (seen in Fig. 4.1 for Mo10.9 alloy) around their respective T_C 's, found from our earlier magnetic measurements (chapter 2). Depending on the range of temperature we have used Eq.(5.2) or Eq.(5.3) to analyze the data. Among them *two* alloys have $T_C \sim 200$ K and the remaining *four* have $T_C \sim 50$ K. Since the electron-phonon scattering is most dominant in the high-temperature region we have fitted the data just above T_C till 300 K using Eq.(5.1) in order to find θ_D . In spite of the fact that we were above T_C , a better fit and a reasonable θ_D have been found when we incorporated the electron-magnon (T^2) scattering term in addition to Eq.(5.1). The values of θ_D are pretty close to that of pure Ni (375 K). The values of A are comparable to those found for disordered CuMn alloys [139]. The parameters listed in Table 5.3 for samples Mo10.9 and W10.5 are found from the data below T_C , only the value of θ_D has been taken from the above T_C data fitted to Eq.(5.3). For these two samples, the values of A are pretty close to those found from either side of T_C but the values of B differ a lot, owing to the fact that the electron magnon scattering is expected to be small above T_C . So for these *two* samples the values of B, given in Table 5.3, are found from the data below T_C . For the remaining *four* samples, we have tried the same method as above but fixing the θ_D from the high-temperature regime to fit the data below T_C did not work. The values of T_{min} found from the fits differed from the experimental values by at least 5 K for all the samples. The reason we could not fit the data below T_C using Eq.(5.2) for these low- T_C samples, is that in this low temperature regime the contributions ρ_{e-e} , ρ_{e-m} , and ρ_l are almost of the same order of magnitude, hence even if a good fit is found, any one of the parameters A, B and C was often found to be unphysical. The most reliable fit, where all the parameters made sense, did not give the right value of T_{min} , which we suppose is due to the limited accuracy of our data. So for these *four* alloys we only fitted the data above T_C using Eq.(5.3) and listed those parameters in Table 5.3. Figures 5.3, 5.4 show the best fits for $Ni_{83}Fe_{10}V_7$ and $Ni_{83.1}Fe_{6.0}Mo_{10.9}$ alloys. The corresponding inset shows the deviation of the data from the fit to Eq. 5.2 and 5.3. Although the deviations are somewhat systematic, their values are pretty small and hence the fits are quite reasonable. In the case of low T_C alloys the

fits are better with ρ_{e-m} term since there are enough number of magnons for enhanced electron - magnon scattering around T_C . Both B and C did not change in different ranges of temperature (Tables 5.2 and 5.3) ensuring the correctness of our procedure.

5.3 Electrical Resistivity of the Ferromagnetic Amorphous Alloys

Again conventional four-probe DC method is used to measure the electrical resistivity of amorphous alloys $\text{Fe}_{7.8}\text{Co}_{31.2}\text{Ni}_{39-x}\text{Cr}_x\text{B}_{14}\text{Si}_8$ ($x = 5, 10, 15$, designated as B2, B3, B4) and $\text{Fe}_{7.8}\text{Co}_{31.2}\text{Ni}_{24}\text{Mn}_{15}\text{B}_{14}\text{Si}_8$ (B5) in a home-made liquid He 4 cryostat with an automated data acquisition system in the temperature range $\sim 1.5 - 300$ K. The current and the voltage contacts with the sample were made with a nonsuperconducting Zn-Cd solder. Typical measuring current of 15 - 30 mA has been used to minimize any heating effect in these highly resistive metallic glasses even at 1.5 K. Data were taken at intervals of 25 mK or less in the temperature range below minima and 100 mK or higher above. The resolution of the resistivity measurements $\Delta\rho/\rho$ is better than a few parts per million and the temperature stability was 3 to 50 mK depending on the range of temperature. The geometrical factors were determined from the mass, density, length, and width of the samples. The maximum error in the resistivity was $\sim 5\%$ due to the uncertainties in the geometrical factors.¹

XRD measurements confirmed the amorphous nature of the samples. ac-susceptibility (χ) measurements (at 3.3 kHz and 0.1 Oe rms field) show that there is only one transition in these metallic glasses from a high-temperature paramagnetic phase to a ferromagnetic one at the respective Curie temperatures T_C , given in Table 5.4. Except for B5, all the alloys could be thought of as a pseudo-binary Ni-Cr alloy, Cr gradually replacing Ni with Co, Fe and the metalloids remaining constant for the same series. In Fig. 5.5, the normalized resistance $r [R(T)/R(290\text{K})]$ is plotted against temperature for all the samples. All of them show minimum at a temperature of T_{min} . The minima look very prominent because of the very high resolution of the data. The ferromagnetic Curie temperature T_C decreases from 386 to 158 K and T_{min} increases systematically from 15

¹This part of the chapter has been published in J. Appl. Phys **103** (2008)

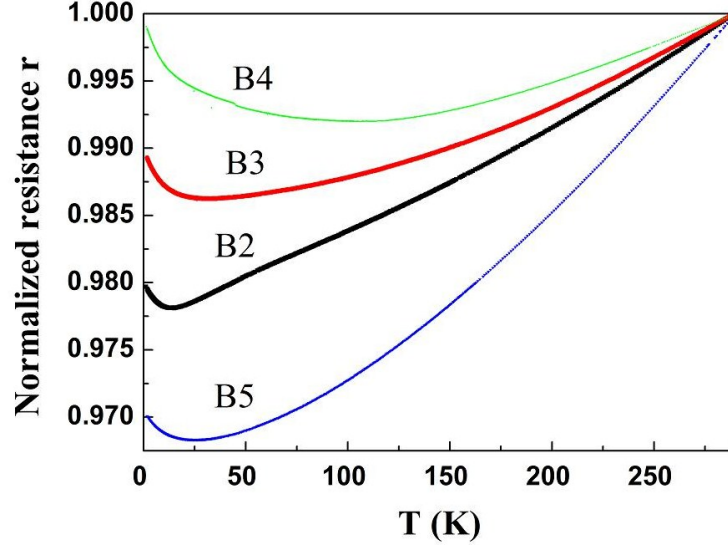


Figure 5.5: (The normalized resistance r [$R(T)/R(290K)$] is plotted against temperature for all the samples of B-series. The minima look very prominent because the resolution of the resistivity data ($\Delta\rho/\rho$) was better than a few parts per million.

to 115 K as Cr concentration increases as shown in Fig. 5.6 for B2, B3, and B4. The decrease of T_C with Cr concentration indicates weakening of the ferromagnetic exchange interaction. Therefore the phase coherence leading to weak localization is retained till higher temperatures; hence we find a higher T_{min} . For the Mn containing sample (B5), they are 368 and 39 K, respectively.

In this section we have analysed our data in terms of conductivity σ instead of resistivity ρ . The fitting equations used are:

- (i) Kondo resistance minima : $\sigma = \sigma_0 + \alpha' \ln(T)$,
- (ii) Resistivity minima due to e-e interactions : $\sigma = \sigma_0 + \alpha' \sqrt{T}$.
- (iii) Temperature dependence of dynamical structure factor : $\sigma = \sigma_0 - \beta T^2$ for $T \ll \theta_D$
and $\sigma = \sigma_0 - \gamma T$ for $T \gg \theta_D$
- (iv) Spin-disorder resistivity in amorphous ferromagnets : $\sigma = \sigma_0 - \delta T^{3/2} - \beta' T^2$ for $T \ll \theta_D$
and $\sigma = \sigma_0 - \eta T^2$ for $T \gg \theta_D$

Table 5.4: Sample ID , T_C , T_{min} , fitting range, fitting equations and parameters, normalized χ^2 , and R^2 for the region well below T_{min} .

Sample ID	T_C (K)	T_{min} (K)	Fitting range (K)	Fitting Eq : $\sigma = \sigma_0 + \alpha\sqrt{T}$			Fitting Eq : $\sigma = \sigma_0 + \alpha' \ln(T)$				
				$\sigma_0 \times 10^5$ $((\Omega m)^{-1})$	$\alpha \times 10^2$ $((\Omega m K^{1/2})^{-1})$	χ^2 (10^{-10})	R^2	$\sigma_0 \times 10^5$ $((\Omega m)^{-1})$	$\alpha' \times 10^2$ $((\Omega m \ln K)^{-1})$	χ^2 (10^{-10})	R^2
B2	386	15	1.5 - 5	7.43061 ± 0.00006	5.93 ± 0.03	0.82	0.999	7.4182 ± 0.0001	0.65 ± 0.01	9.81	0.986
B3	222	32	1.5 - 9	7.49002 ± 0.00004	8.51 ± 0.02	1.22	0.999	7.4955 ± 0.0002	8.7 ± 0.1	44.14	0.987
B4	158	115	1.5 - 10	7.4188 ± 0.0001	10.82 ± 0.05	14.35	0.998	7.4257 ± 0.0003	11.3 ± 0.2	197.7	0.974
B5	368	39	1.5 - 10	6.34973 ± 0.00004	4.43 ± 0.02	1.78	0.999	6.3524 ± 0.0001	4.71 ± 0.02	6.5	0.989

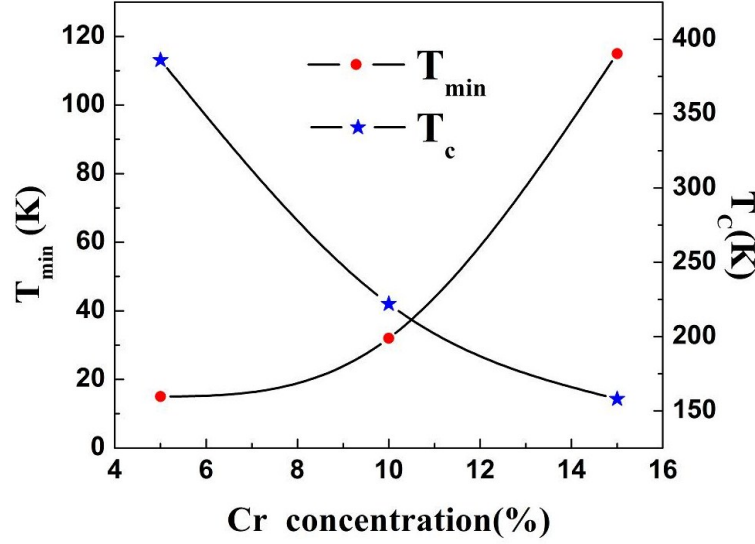


Figure 5.6: (T_{min} and T_C vs. Cr concentration in samples B2, B3, and B4.

T_{min} , the second one above T_{min} but below Debye temperature θ_D , and the other $\geq \theta_D$.

5.3.1 Low-temperature: $T \ll T_{min}$

For the region well below the minima, we have analyzed from 1.5 K to 5 K for B2 and till 10 K for the others. Here also both logarithmic and square root fits were tried. Figure 5.7 shows the $\sigma(T)$ data of all the samples till 10 K and the excellent fits to $\sigma(T) \sim \sqrt{T}$ till 5 or 10 K. The inset is a plot of the deviations (%) vs. T for sample B3 for both the fits. Not only are the values (Table 5.4) of χ^2 smaller by a factor of 9 to 30 for the \sqrt{T} fit, the deviation of the best-fitted curves from the experimental one (Inset of Fig. 5.7) is large and systematic for the $\ln T$ fit whereas it is much smaller (less than 0.001%) and more importantly quite random (crossing the x-axis several times) for the \sqrt{T} fit. Moreover, the correlation coefficients are respectively, 0.984 and 0.999 for $\ln T$ and \sqrt{T} fits. Also, the error bars of the coefficients α are a factor of 5 smaller than those of α' . The diffusion constant D , averaged over the samples is found to be $\approx 1.5 \times 10^{-5} m^2 s^{-1}$. All the above give a very clear signature of \sqrt{T} dependence of conductivity at very low temperatures in both of these Co-rich Ni-Cr pseudo-binary systems, ascribed to quantum interference

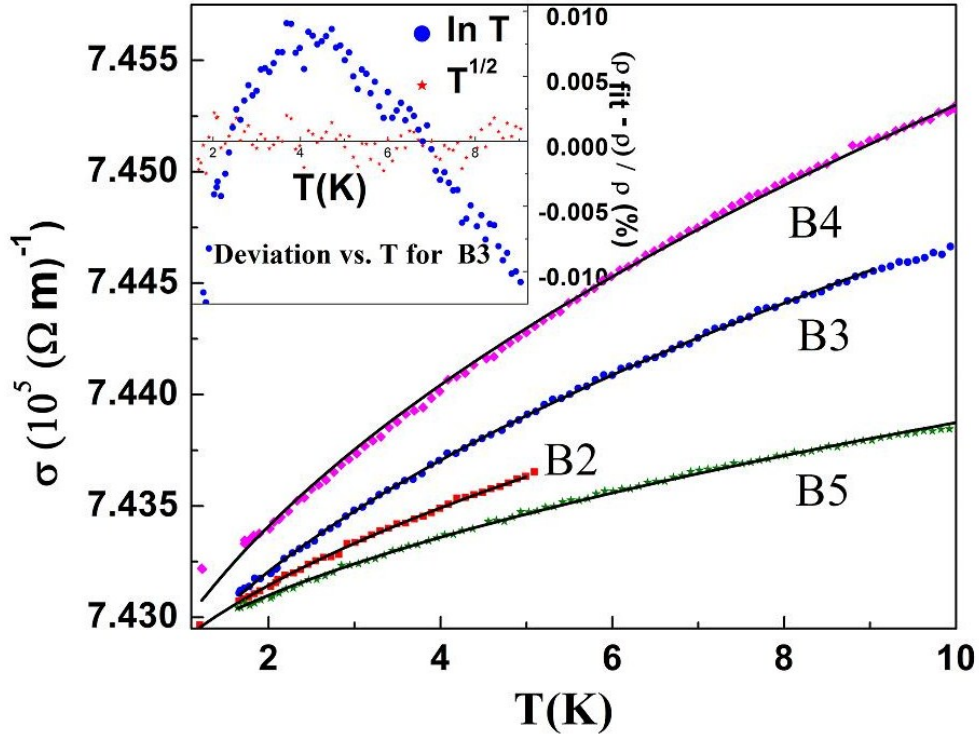


Figure 5.7: The conductivity σ vs. temperature data of all the samples of B-series till 10 K along with the fits (solid lines) to Eq. $\sigma(T) \sim \sqrt{T}$ till 5 or 10 K (well below T_{min}). The inset is a plot of the deviations (%) of the data from the best-fitted curves vs. T for sample B3 for both $\ln T$ and \sqrt{T} fits. The curves for samples B5, B3, and B2 are respectively shifted along σ axis by $+1.075 \times 10^5 (\Omega m)^{-1}$, $-0.07 \times 10^5 (\Omega m)^{-1}$, and $+0.01 \times 10^5 (\Omega m)^{-1}$ with respect to B4.

effects showing up due to their high structural disorder.

5.3.2 Intermediate temperature: $\theta_D \gg T > T_{min}$

For temperatures higher than T_{min} , but well below θ_D , both T^2 and $T^2 + T^{3/2}$ fits are tried, where the choice of the suitable temperature range depended on both T_{min} and T_C , for B2 this range is 100 to 160 K, 32 to 150 K for B3, 115 to 158 K for B4 and 40 to 90 K for B5. In the case of B4 the range was crucial ($T_C = 158$ K and $T_{min} = 115$ K) since it was too narrow to satisfy the condition that T should be above T_{min} but below T_C . Figure 5.8 and its insets show $\sigma(T)$ vs. T data for samples B5, B3, and

Table 5.5: Sample ID , fitting range, fitting equations and parameters, normalized χ^2 , and R^2 for the region well above T_{min} but much below T_C .

Sample ID	Fitting range (K)	Fitting Eq : $\sigma = \sigma_0 - \beta T^2$		Fitting Eq : $\sigma = \sigma_0 - \delta T^{3/2} - \beta' T^2$					
		$\sigma_0 \times 10^5$ $((\Omega m)^{-1})$	$\beta \times 10^{-1}$ $((\Omega m K^2)^{-1})$	χ^2 (10^{-10})	R^2	$\delta \times 10^{-1}$ $((\Omega m K^{3/2})^{-1})$	$\beta' \times 10^{-1}$ $((\Omega m K^2)^{-1})$	χ^2 (10^{-10})	R^2
B2	100 - 160	7.4084 ± 0.0001	2.099 ± 0.008	26.4	0.998	44	- 0.79 ± 0.05	0.88	0.999
B3	32 - 150	7.52592 ± 0.00001	1.367 ± 0.001	1.99	0.999	0.8	1.31 ± 0.01	1.82	0.999
B4	115 - 158	7.4946 ± 0.0001	0.69 ± 0.01	9.72	0.991	- 49 ± 1	3.84 ± 0.09	0.67	0.999
B5	40 - 90	6.37061 ± 0.00002	3.293 ± 0.004	1.60	0.999	3.9 ± 0.4	2.93 ± 0.07	1.31	0.999

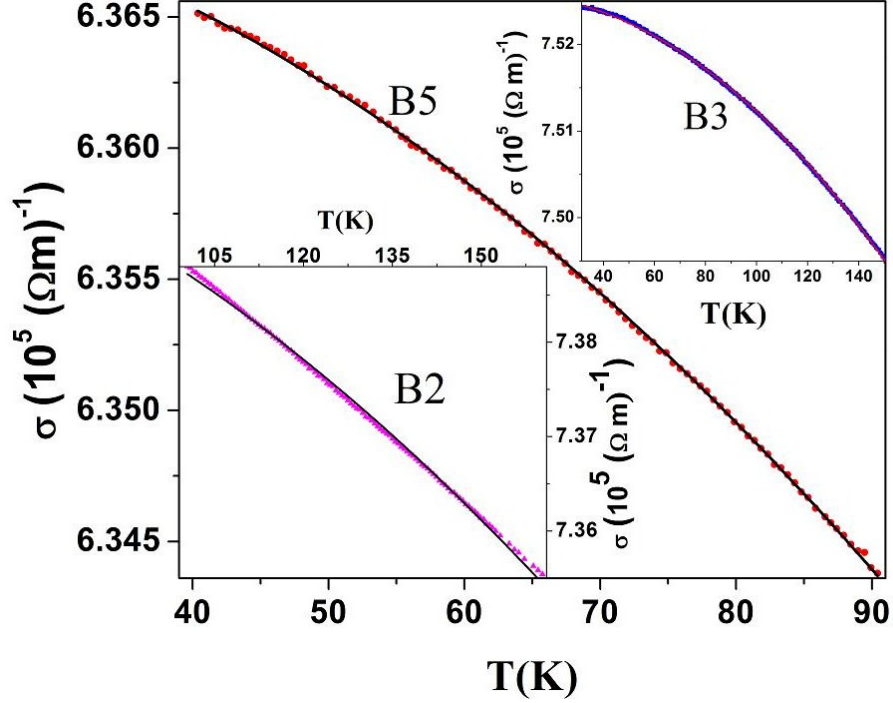


Figure 5.8: The conductivity σ vs. T data for sample B5 along with the best-fitted curves (solid lines) to Eq. $\sigma = \sigma_0 + \beta T^2$. The insets show the same for samples B3 and B2.

B2, respectively in the temperature ranges mentioned above. Also shown are the best-fitted curves to $\sigma = \sigma_0 - \beta T^2$. Table 5.5 gives sample ID, fitting range, fitting equations and parameters, normalized χ^2 , and R^2 for the region well above T_{min} but much below T_C . However, it is found from Table 5.5 that, although the best-fitted coefficients β is positive for all the samples for both the fits, δ and β' turn out to be negative for the fits to $\sigma = \sigma_0 - \delta T^{3/2} - \beta' T^2$ making them physically unacceptable for samples B4 and B2, respectively. For B3 and B5, the fits to Eq. (4) look marginally better from their lower values of χ^2 . The error bars of the coefficients β are a factor of 10 - 20 smaller than those of β' . This is a better indicator for the goodness of fits. So we find that we cannot really isolate the leading magnetic $T^{3/2}$ term [70] for these amorphous ferromagnets. The conductivity is well described by only a T^2 term which could be both magnetic and structural in origin. A closer look at Table 5.5 shows that β decreases systematically as 2.1, 1.4, and 0.7 ($10^{-1}(\Omega m K^2)^{-1}$) in samples B2, B3, and B4 with the increase in Cr concentration. Increasing Cr content gradually destroys the ferromagnetic

Table 5.6: Sample ID , fitting range, fitting equations and parameters, normalized χ^2 , and R^2 for the region $T \geq \theta_D$ but below T_C .

Sample ID	Fitting range (K)	Fitting Eq : $\sigma = \sigma_0 - \gamma T - \eta T^2$				R^2
		σ_0 ($10^5(\Omega m)^{-1}$)	γ ($10(\Omega m K^{3/2})^{-1}$)	η ($10^{-2}(\Omega m K^2)^{-1}$)	χ^2 (10^{-10})	
B2	200 - 300	7.4352±0.0007	3.99±0.05	6.1±0.1	0.75	0.99999
B3	200 - 300	7.556±0.00001	2.96±0.07	5.9±0.1	1.33	0.99997
B4	200 - 300	7.5493±0.0002	4.26±0.01	-	13.45	0.99967
B5	200 - 300	6.419±0.001	6.5±0.1	7.7±0.2	2.48	0.99998

order and hence reduces the electron-magnon scattering contribution to the resistivity without changing significantly the electron-phonon scattering. So we conclude that the T^2 term indeed contains a magnetic contribution to the electrical resistivity.

5.3.3 Higher temperature: $T \geq \theta_D$

The purpose of the analysis of $\sigma(T)$ data in this regime is as follows: At low temperatures the structural and the magnetic contributions are both proportional to T^2 and so they are indistinguishable. However, at higher temperatures the structural term goes as T while the magnetic term follows a T^2 dependence. We have chosen a wide enough range of 200 - 300 K so that if there is a magnetic contribution at all, we should be able to detect that. In this range, the magnetic contribution is hardly expected for B4 since its T_C is 158 K. So, only the structural contribution $\propto T$ is considered for its fit to $\sigma = \sigma_0 - \gamma T - \eta T^2$. The data for the other samples are, however, fitted to the full to this equation since their T_C s are mostly above the range of 200 to 300 K. Figure 5.9 shows conductivity σ vs. temperature data of all the samples of B-series from 200 to 300 K along with the good fits (solid lines) to $\sigma = \sigma_0 - \gamma T - \eta T^2$ for B2, B3, and B5 but without the T^2 term for B4. The curves for samples B5 and B3 are respectively shifted along σ axis by $+1.15 \times 10^5 (\Omega m)^{-1}$ and $-0.04 \times 10^5 (\Omega m)^{-1}$ while B4 and B2 have their actual values.

Table 5.6 gives sample ID, fitting range, fitting equations and parameters, normalized χ^2 , and R^2 for the region $T \geq \theta_D$ but below T_C . The fits are excellent as seen from Fig.

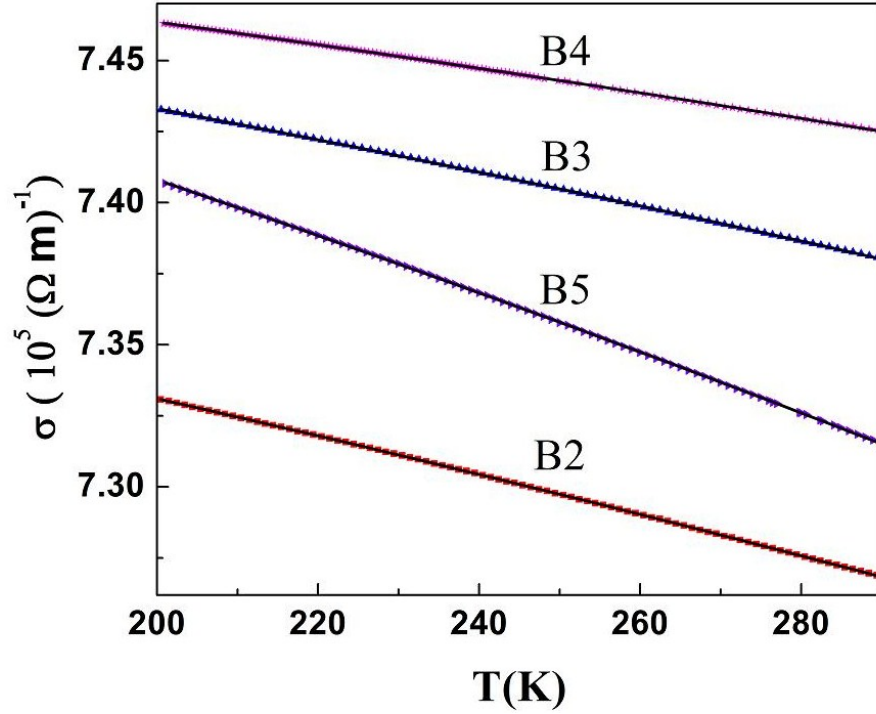


Figure 5.9: The conductivity σ vs. temperature data of all the samples of B-series from 200 to 300 K along with the fits (solid lines) to Eq. $\sigma = \sigma_0 - \gamma T - \eta T^2$ for all the samples but without the T^2 term for B4. The curves for samples B5 and B4 are respectively shifted along σ axis by $+1.15 \times 10^5 (\Omega m)^{-1}$ and $-0.04 \times 10^5 (\Omega m)^{-1}$ while B3 and B2 have their true values.

5.9 and the low values of χ^2 and the correlation coefficients being very close to 1. Using the values of the coefficients from Table 5.6, we find that the magnetic contribution ηT^2 is $\sim 33\%$ of the structural contribution γT , from which it is clear that there is indeed a magnetic contribution. From the relevant parameters from Tables 5.5 and 5.6, Debye temperature is calculated using $\theta_D \approx \left(\frac{\pi^2}{6}\right) \left(\frac{a}{b-c}\right)$, where $a = \gamma/\sigma_0^2$, $b = \beta/\sigma_0^2$, and $c = \eta/\sigma_0^2$. Here, σ_0 is taken from the respective fits. For B4 only, c is taken as zero since the T^2 term was omitted in this temperature range ($T_C = 158$ K). The values of θ_D for B2 and B5 are ~ 382 K, as found in similar ferromagnetic amorphous alloys. θ_D of 617 K for B3 is on the higher side but 1025 K for B4 is indeed unrealistic. The latter is most probably due to the very limited available range of 115-158 K (Table 5.5) which hardly satisfies the condition, “well above T_{min} , but much below T_C ”, from where one gets β

and hence b and θ_D . For B3, the magnetic contribution in the fitting range of 200-300 K (Table 5.6) is comparable to those of B2 and B5 ($T_C \sim 380$ K) which are ferromagnetic in the whole range. This is not true for B3 ($T_C \sim 222$ K). So we apprehend that although the fit was very good, the coefficients γ and η which are used to calculate θ_D , may not be very dependable. The values of θ_D , found from the above fits for B3 and B4, are no doubt unphysical. But had they been really so high, we would not have found substantial linear structural γT term between 200 and 300 K, which is so much below θ_D .

5.4 Electrical Resistivity of PLD-grown Ni-nanocrystalites in TiN matrix

Epitaxial nanocrystalline nickel particles were embedded in metallic TiN matrices using the pulse laser deposition technique described in details elsewhere [140]. The sample consists of five alternate layers of self-assembled Ni nanoparticles and TiN, epitaxially grown on Si (100) substrate and an extra TiN layer on top of nickel nanoparticles. The choice of TiN as the metallic matrix is due to the high chemical stability, hardness, unusually high electrical conductivity and its role as a diffusion barrier for the nickel atoms and the silicon wafer. Figure 5.10 shows a high-resolution STEM-Z contrast image of Ni particles in TiN matrix [140]. It is clear that the epitaxial metallic particles are well separated (~ 10 nm) from each other and the average Ni nano-dots have a typical size of (13 ± 4) nm. The Ohmic resistance was measured from 0 to 4 tesla between 4.2 and 300 K with a sample current of 10 mA using the standard four-probe dc-technique with a resolution of \sim one part per million using a home-made PPMS [97]. However, the error in resistivity was $\sim 5\%$.²

The resistivity data Ni/TiN composite sample are shown from 10 to 300 K in zero fields in Fig.5.11 and from 4.2 K till 60 K at fields of 0, 1, 2, and 4 tesla in Fig. 5.12. Similar resistivity minima have been obtained earlier but only in 2D multilayer systems of Ni, like Mo/Ni [141] and Nb/Ni [142]. Resistivity minima for samples containing isolated magnetic moments, as in the present Ni/TiN composite sample, might be interpreted as Kondo minima. Had it been so, then it should have disappeared in an applied magnetic

²This part of the chapter has been published in Appl. Phys. Lett. **92**, (2008).

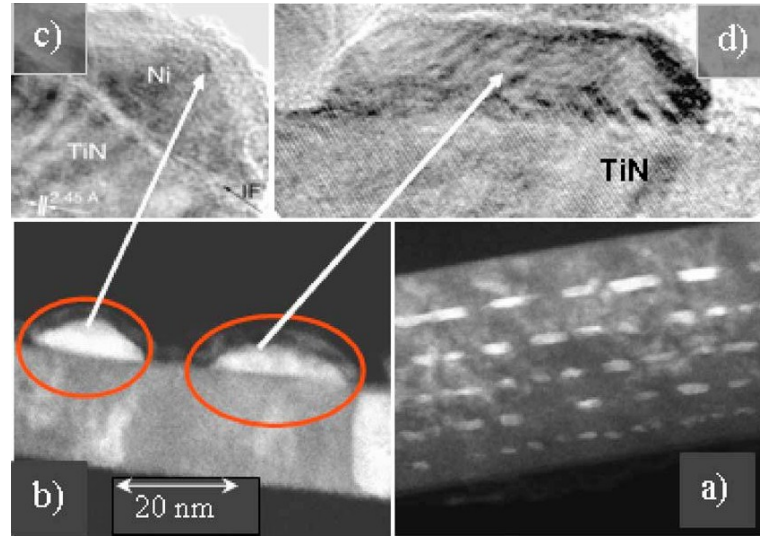


Figure 5.10: (a): A cross-sectional STEM-Z image, (b) its expanded view, (c) high-resolution STEM-Z contrast image of textured Ni nanocrystallites with triangular morphology, and (d) with rectangular morphology, all embedded in TiN matrix.(from ref. [140])

field and also shown a $(-\ln T)$ dependence of ρ . On the contrary, here T_{min} is found to be nearly independent of the magnetic field as high as 4 tesla (Fig. 5.12) varying randomly between 36.7 and 38.0 K. The depth of the minimum (DOM) is only $\sim 0.1\%$ for all fields. The minima look very prominent because of the very high resolution of the data.

We fitted the $\rho(T)$ data from 4.2 to 25 K (well below T_{min}) to both $-\ln T$ and $-\sqrt{T}$. The inset of Fig. 5.13 and Fig. 5.13 itself show respectively, the above fits for magnetic fields of 0, 1, 2, and 4 tesla. Needless to say that the $(-\sqrt{T})$ fit is far better than the $(\ln T)$ fit. Not only are the values of χ^2 larger by a factor of 13 to 53, the deviation of the best-fitted curves from the experimental one is large and systematic for the latter whereas it is much smaller and more random for the former fit. Moreover, the correlation coefficients are respectively, 0.999 and 0.987. Therefore, one can rule out the possibility of Kondo minimum in the present case. The quantity $m_\sigma = C/\rho_\sigma^2 \sim 630 (\Omega m K^{1/2})^1$ (mentioned earlier in this Chapter), averaged over all fields compares very favorably with almost an universal value of $600 (\Omega m K^{1/2})^1$ found in amorphous metallic glasses and other dirty systems interpreted in terms of quantum interference effects (QIE). Also the calculated mean-free path from the measured conductivity, Fermi velocity, and conduction

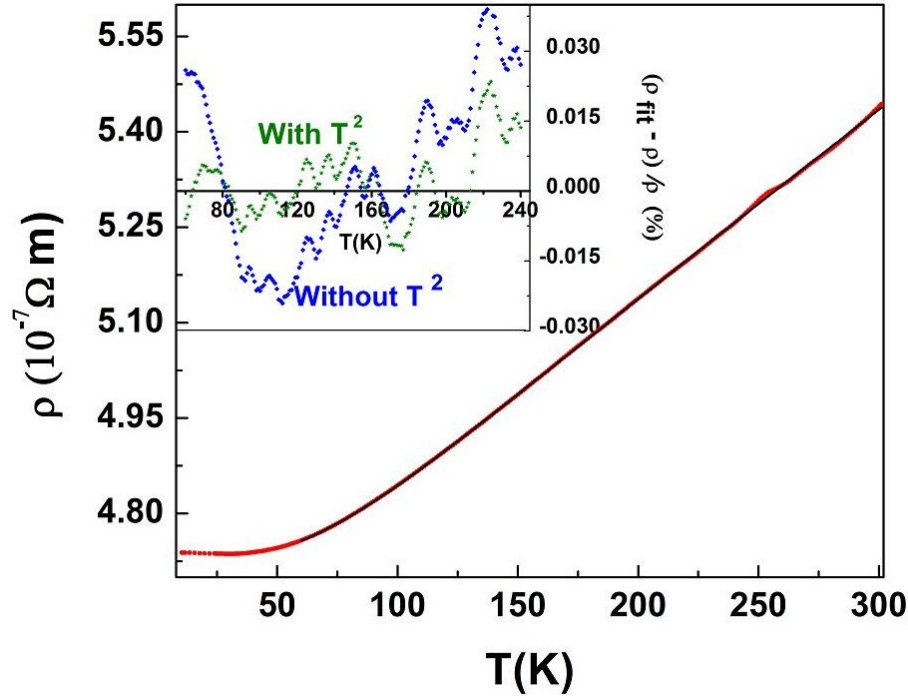


Figure 5.11: Zero-field resistivity is plotted against temperature from 10 to 300 K. The solid line is the best fit of the data between 60 and 300 K to Eq.(5.3). The inset shows the temperature dependence of the deviations of the data from the fits to Eqs. (5.3), with and without the magnetic term, $\rho_m = BT^2$. The average deviations are respectively, 0.006 % and 0.015 %.

electron density is found to be $\sim (1 - 4)$ nm. So our results strongly suggest that the low-temperature minima have their origin in the QIE where Boltzmann transport equations fail as the electrons are scattered even within the isolated Ni nanoparticles with some size distribution and positional disorder. The residual resistivity, ρ_0 of $47 \times 10^{-8} \Omega m$ for our Ni/TiN composite sample is rather on the low side for electron localization. Generally, it shows up if ρ_0 is $\sim 100 \times 10^{-8} \Omega m$. However, many bulk Ni($\sim 75\%$) alloys [138] with Fe and Cr additions and $\rho_0 \sim (58-92) \times 10^{-8} \Omega m$ do show T_{min} between 7 and 36 K.

We also interpreted the temperature dependence of resistivity well above T_{min} from 60 to 300 K in the composite Ni/TiN system. The electrical resistivity in 3d transition metals like Fe, Co, and Ni is given by (using Mathiessens rule) Eq.5.3. As already stated, Fig. 5.12 shows ρ vs. T in zero magnetic fields from 10 to 300 K. The data above 60 K

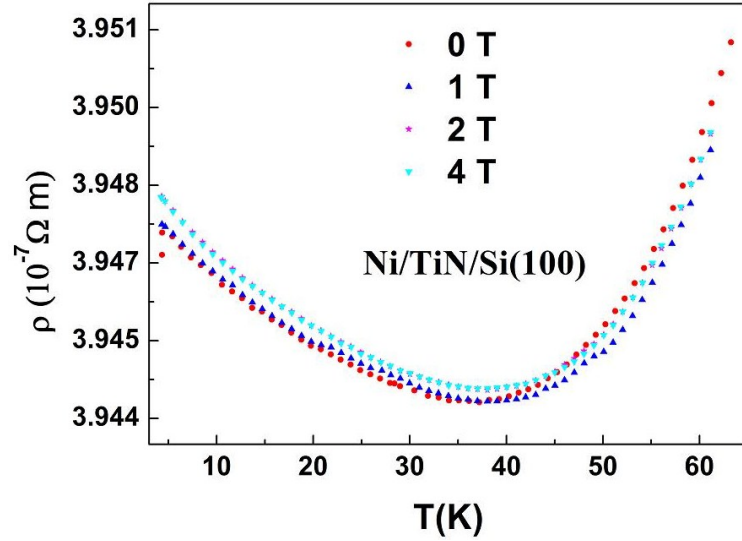


Figure 5.12: Resistivity vs. temperature from 4.2 K till 60 K at fields of 0, 1, 2, and 4 tesla showing minimum at T_{min} , nearly independent of the magnetic field. The minima look very prominent because of the very high resolution of the data.

were fitted to Eq. (5.3) with the ρ_l given by Eq. (5.1) and $\rho_m = BT^2$ using a least squares fit program which also evaluated the integral numerically at each iteration. Excellent fit, shown by the solid line in Fig. 5.12, was obtained with an average deviation of only 0.006 % and correlation coefficients of 0.99997. The inset shows the deviations of the data (from 60 to 240 K to avoid a spurious hump around 250 K) from the fits to Eq. (5.3), with and without the magnetic term vs. T . The average deviation of 0.015 % was much more without the magnetic term. Moreover, the deviations were more systematic for the latter and rather random for the former. Thus we get a convincing evidence for the magnetic T^2 term in this nanostructured Ni/TiN composite.

The best-fitted value of the Debye temperature, θ_D is (489 ± 4) K, compared to 375 K for bulk Ni. The best-fitted coefficient of the magnetic term, $B = (3.8 \pm 0.5) \times 10^{-14} \Omega m K^{-2}$ for this Ni/TiN sample agrees fairly well with that of bulk Ni [131–133], viz, $10 \times 10^{-14} \Omega m K^{-2}$. The best-fitted residual resistivity, $\rho_0 \sim 47 \times 10^{-8} \Omega m$ is nearly the same as that of TiN ($\sim 45 \times 10^{-8} \Omega m$). The resistivity of the present Ni/TiN composite sample changed from $\sim 47 \times 10^{-8} \Omega m$ to $\sim 54 \times 10^{-8} \Omega m$ from 4.2 to 300 K. The resistivity of TiN itself is $\sim 45 \times 10^{-8} \Omega m$ at 300 K and is nearly temperature independent in this

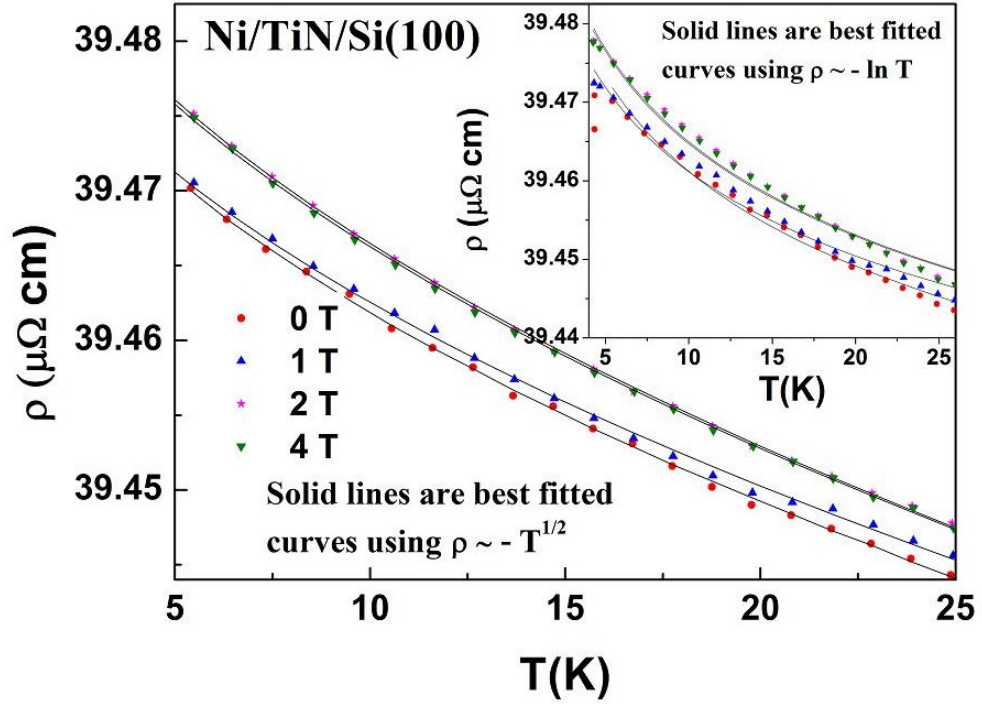


Figure 5.13: Fits of $\rho(T)$ data from 4.2 to 25 K (well below T_{min}) and magnetic fields from 0 to 4 tesla to $\rho(T) \sim -\sqrt{T}$. The inset shows similar fits to $\rho(T) \sim -\ln T$. The $(-\sqrt{T})$ fit is far better than the $(-\ln T)$ fit. The values of the normalized χ^2 are smaller by a factor of 13 to 53 for the $(-\sqrt{T})$ fit.

range. So, it is quite logical to conclude that the above change of $\sim 7 \times 10^{-8} \Omega\text{m}$ comes from the temperature dependence of resistivity of Ni, given the fact that the resistivity of 100 nm Ni nanoparticles changes by a similar amount of $7 \times 10^{-8} \Omega\text{m}$. This justifies our interpretation of ascribing the fitted values of the Debye temperature, θ_D and the coefficient of the magnetic term, B to Ni only. The best-fitted residual resistivity, $\rho_0 \sim 47 \times 10^{-8} \Omega\text{m}$ is, on the other hand, attributed to the almost temperature independent resistivity of $\sim 45 \times 10^{-8} \Omega\text{m}$ of TiN.

5.5 Conclusion

To conclude, the electrical resistivity of three completely different disordered magnetic systems namely, (i) disordered magnetic Ni-rich ternary alloys, (ii) Co-rich ferromagnetic

amorphous alloys, and (iii) Ni-nanocrystallites on TiN matrix has been studied satisfactorily.

For the Ni-rich disordered ternary Ni-Fe-M (M = V, Mo, W) alloys, we have found that the resistivity by and large increases with V, Mo, and W additions if Fe content is about the same. We have been able to extract from their $\rho(T, H)$ the electron - electron, electron - magnon, and electron - phonon contributions quite meaningfully. The electronmagnon scattering strength shows a tendency to increase with increasing Fe dilution, which we believe is due to the strongly coupled Fe spins in the alloys, as we have found in the magnetization behaviour of these alloys. The observed resistivity minima presumably come from electron - electron interactions. They are almost unaffected by applied fields till 5 T, ruling out the Kondo effect as a possible origin. The increase in the coefficient of the $-\sqrt{T}$ term (e-e interaction) in $\rho(T)$ with increasing V, Mo, and W (i.e., increasing Fe dilution) is expected from the enhanced electron localization due to increased disorder in the alloys. The derived Debye temperatures are quite reasonable when compared with those of similar ternary alloy systems.

Very high-resolution ($\Delta\rho/\rho \sim$ a few parts per million) $\rho(T)$ data of a amorphous Co-rich pseudo-binary Ni-Cr alloy system with fixed amount (28 %) of metalloids B and Si are reported between 1.5 and 300 K. The metalloids stabilize the glassy phase in these high-resistive ($120 - 160 \times 10^{-8}\Omega\text{m}$) soft ferromagnets, which are ideal for many applications. The first key result is the satisfactory isolation of contributions to resistivity from i) electron-electron interactions in the presence of weak localization, ii) the temperature dependence of dynamical structure factor, and iii) electron-magnon scattering. The task was not easy in view of the severe restrictions imposed by the relevant theories on the range of temperature that is available for analysis with respect to characteristic temperatures like Debye, Curie, and T_{min} . Various aspects of the goodness of fits, like χ^2 , correlation, and the error bars of the coefficients were given due consideration in arriving at the conclusions. The second important finding is that the conductivity data unequivocally obey the equation $\sigma = \sigma_0 + \alpha'\sqrt{T}$ very accurately in the low-temperature regime of 1.5 to 10 K, where e-e interaction effects are most unlikely to be suppressed by other faster dephasing processes.

Finally, at low temperatures in 3D Ni/TiN system, electron-electron interaction in the

presence of weak localization dominates the electrical transport giving rise to resistivity minima with T_{min} independent of the magnetic field. We argue that Ni nanoparticles with a size distribution and some positional disorder along with the high resistivity of TiN localize the electrons. Above T_{min} , the temperature dependence of $\rho(T)$ is mainly dictated by that of Ni and the residual resistivity wholly comes from the almost temperature-independent resistivity of TiN.

Chapter 6

PLD grown nanometer size Ni-Fe-Mo alloy thin films

In this chapter a detailed structural and magnetic study of Pulsed Laser Deposited (PLD) soft ferromagnetic thin films of Ni-Fe-Mo alloys on Sapphire single crystals will be discussed. Thin films of different thicknesses are grown to correlate the thickness dependence of both structural and magnetic properties. All the films are highly textured with grain size increasing with increasing thickness. The film thickness has been calculated using X-ray reflectivity (XRR) as well as Rutherford back scattering (RBS). The XRR data indicate that instead of a uniform density there are effectively three layers with density gradient across the thickness while the thickness found from RBS measurements matches fairly well with that of the middle layer found from the XRR analysis. The Atomic Force Microscope (AFM) images give the average values of the roughness that are very similar to those calculated from reflectivity measurements. Energy dispersive X-ray spectroscopy (EDXS) measurements reveal that the composition in the films is indeed very close to that of the bulk targets (discussed in Chapter 3). From the magnetization studies much higher values of the Curie temperature T_C were obtained than those of the bulk targets. Low-field zero fieldcooled (ZFC) and field-cooled (FC) magnetization show spin-glass-like features in all the films coming from both compositional and structural disorder. The spin-wave stiffness constants D , calculated from low temperature and saturation field magnetization data, are higher than their bulk counterparts. The coercive field and the saturation magnetization also increased similarly but still retaining their soft ferromagnetic character. All these will be discussed in details in the following sections.¹

¹The contents of this chapter has been communicated to J. Appl. Phys. and partly published in MRS Proceedings **1200E** (2010).

6.1 Introduction

Soft ferromagnetic materials have received a lot of attention due to their potential applications as transformer cores. Recently soft ferromagnetic thin films are widely used in sensor technology, specially the binary $\text{Ni}_{80}\text{Fe}_{20}$ because alloys close to this composition have high permeability, near-zero magnetostriction, and magnetocrystalline anisotropy constant K_1 [143]. A small addition of other transition metals, particularly molybdenum, could make the permeability [144] even higher. A number of researchers have electrodeposited NiFeMo alloy films and studied their magnetic properties as these electrodeposited soft magnetic films are critical components of hard disk write heads for magnetic recording [145]. There are many other applications like micromachined magnetic sensors [146], miniaturized inductors [147] to magnetic actuators in microelectromechanical systems (MEMS) [148]. Surface roughness of micrometer thick electrodeposited NiFeMo films and comparison of the thickness dependence of the roughness and magnetic coercivity were investigated in another work [149]. $(\text{NiFe})_{1-x}\text{Mo}_x$ thin films, with $0 < x \sim 0.1$, were sputter-deposited on single crystal silicon wafers and their magnetic properties were measured after annealing for 2 h at various temperatures up to 350°C [150]. For lower Mo content, the anisotropy field H_k decreased with annealing temperature whereas at higher Mo content H_k showed an initial decrease and then an increase above 300°C .

We have already studied single-phase soft ferromagnetic bulk Ni-Fe-Mo alloys with very small coercivity of ~ 0.1 Oe. Here we are presenting systematic studies of PLD grown, a few nm thick films of those alloys and correlated their structural and magnetic properties through a detailed analysis. Our final aim is to compare the magnetic properties of these films with those of the bulk.

6.2 Thin Film Preparation

For thin film preparation using the PLD technique, the Ni-Fe-Mo alloy buttons are used as targets; energy density, repetition rate, base pressure, and substrate temperatures are respectively 5 J/cm^2 , 5 Hz , 5×10^{-6} Torr, and 650°C . In the present work, a KrF excimer laser (Lambda Physik, LPX200) having a wavelength of 248 nm is used. The chamber is

flushed with Ar gas 3 times before every deposition to avoid oxidation. Three different thicknesses of each alloy are deposited varying the deposition time and keeping all other parameters constant. After every deposition the substrate is cooled down very slowly to avoid inhomogeneity in the films.

Thin films of three different thicknesses of five Ni-Fe-Mo alloys have been grown using the PLD technique (discussed in Chapter 2). The five alloys are $\text{Ni}_{81.0}\text{Fe}_{16.7}\text{Mo}_{2.3}$, $\text{Ni}_{80.4}\text{Fe}_{12.9}\text{Mo}_{6.7}$, $\text{Ni}_{83.4}\text{Fe}_{10.7}\text{Mo}_{5.9}$, $\text{Ni}_{83.1}\text{Fe}_{6.0}\text{Mo}_{10.9}$, and $\text{Ni}_{83.2}\text{Fe}_{3.3}\text{Mo}_{13.5}$. Arc melted alloy buttons after homogenization are used directly as targets for the deposition. Films are deposited on $\sim 5 \text{ mm} \times 5 \text{ mm}$ single crystal Sapphire (0001) substrates. The nominal thicknesses estimated from the pulse rate are respectively 10, 20, and 30 nm for 10, 20, and 30 min depositions.

6.3 Structural Characterizations

The structural characterizations of these thin films have been done by X-ray diffraction (XRD), XRR, RBS, AFM, EDXA, and cross-sectional imaging with scanning electron microscope (SEM).

6.3.1 X- ray Diffraction

X-ray diffraction patterns of all thin films are taken using Phillips diffractometer to analyze various crystalline aspects. According to the Braggs law,

$$2d_{hkl}\sin\theta_{hkl} = n\lambda. \quad (6.1)$$

The angle of diffraction θ_{hkl} is related to the inter-planer distance d_{hkl} , the X-ray wavelength λ and the order of diffraction n . d_{hkl} , in turn, is related to the lattice constant a and the Miller indices (hkl) [1]. Figure 6.1 shows a typical X-ray diffraction (XRD) pattern for the three different thicknesses of thin films made from $\text{Ni}_{83.4}\text{Fe}_{10.7}\text{Mo}_{5.9}$ alloys along with that of the sapphire substrate. The intensity is plotted in log scale to give the better visibility of the sample peak. The tallest peak comes from the sapphire substrate corresponding to the (0002) plane whereas the second taller peak corresponds to the (111)

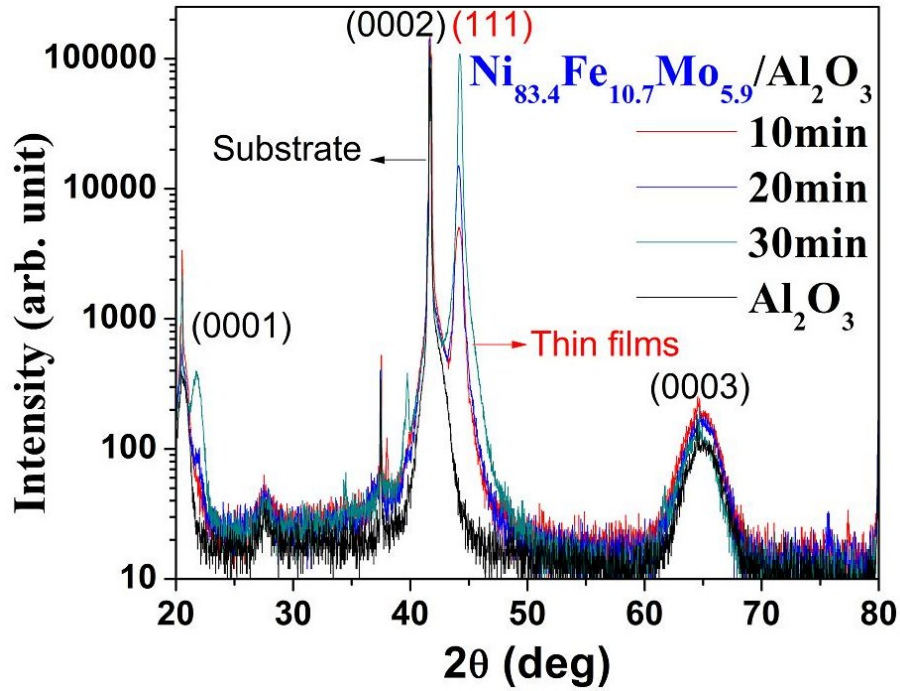


Figure 6.1: X-ray diffraction pattern for the three different thicknesses of thin films made from $\text{Ni}_{83.4}\text{Fe}_{10.7}\text{Mo}_{5.9}$ alloys along with that of the sapphire substrate.

plane of that alloy (a typical XRD of a similar bulk alloy is given in Chapter 3). The presence of a single peak in the XRD pattern corresponding to that of the alloy indicates that the films are almost single crystalline in nature. The directional growth of the crystallites perpendicular to (111) plane indicates face centered cubic structure like pure Ni with a triangular surface symmetry. The intensity of the sample peaks are observed to be greater in thicker films compared to the thinner ones. This fact indicates that the degree of crystallinity is found to be more pronounced in the films of higher thickness. The inter-planer distance (d) and the lattice parameter (a) are calculated for all the thin films from the equation for cubic crystals, viz,

$$\frac{1}{d^2} = \frac{h^2 + k^2 + l^2}{a^2} \quad (6.2)$$

Also, broadening of XRD lines indicates decrease in grain size with thickness. The sample peaks were fitted with Gaussian functions and the full width at half maxima (FWHM) Γ is found from that fitting.

Table 6.1: Target composition, deposition time, 2θ corresponding to the (111) plane of the alloy, inter-planer distance d , lattice constant a , the integral breadth of reflection β , volume weighted crystallite size D , and ε_{str} .

Target Composition	Deposition Time (min)	2θ (111) (deg)	d (\AA)	a (\AA)	β (deg)	D (\AA)	ε_{str} 10^{-3}
Ni _{81.0} Fe _{16.7} Mo _{2.3}	10	44.24	2.045	3.542	0.7025	135	7.6
	20	44.21	2.046	3.544	0.4204	225	4.6
	30	44.26	2.044	3.540	0.3142	302	3.4
Ni _{80.4} Fe _{12.9} Mo _{6.7}	10	44.16	2.048	3.548	0.7249	131	7.8
	20	44.18	2.048	3.546	0.4393	216	4.7
	30	44.22	2.046	3.543	0.3376	282	3.6
Ni _{83.4} Fe _{10.7} Mo _{5.9}	10	44.15	2.049	3.549	0.7130	133	7.7
	20	44.13	2.050	3.550	0.4632	205	5.0
	30	44.24	2.045	3.542	0.3028	314	3.3
Ni _{83.1} Fe _{6.0} Mo _{10.9}	10	44.16	2.048	3.548	0.6997	132	7.5
	20	44.13	2.050	3.550	0.4619	205	5.0
	30	44.18	2.048	3.546	0.3964	241	4.3
Ni _{83.2} Fe _{3.3} Mo _{13.5}	10	43.97	2.057	3.562	0.6529	146	7.1
	20	44.10	2.051	3.552	0.3910	244	4.2
	30	44.18	2.052	3.554	0.3393	282	3.6

The grain size is calculated using the Scherers formula,

$$D = \frac{K\lambda}{\beta \cos\theta}, \text{ (here } K = 1) \quad (6.3)$$

where λ is the wavelength of the X-ray and β is the integral breadth of reflection and is related to Γ by the following relation

$$\beta = \left(\frac{\pi}{4\ln 2}\right)^{1/2} \Gamma \quad \text{(for Gaussian curve)}. \quad (6.4)$$

The proximity of the substrate and the alloy peaks ($\sim 3^\circ$) induces some strain due to lattice mismatch. Oriented growth in these films also reflect the presence of some strain. The lattice strain also induces line broadening and can be calculated using the following

expression given by Stokes and Wilson

$$\varepsilon_{str} = \frac{\beta}{4\tan\theta}, \quad (6.5)$$

where ε_{str} is the weighted average strain.

From Table 6.1 it is found that, with increasing film thickness the grain size increases and the strain decreases quite systematically. This is attributed to the decrease of imperfections and dislocations with increasing film thickness. It is also observed that the integral breadth of reflection β and hence FWHM decreases with increasing thickness. This decrease in FWHM implies, through Eqs. 6.3–6.5, an increase in crystallite/grain size or a decrease in residual strain. The increasing strain induces magnetic anisotropy in the films which, in turn, might affect the magnetic properties to a large extent.

6.3.2 X-ray Reflectivity

In this section detailed findings from X-ray reflectivity (XRR) measurements of the thin films will be discussed. The X-ray reflectometry attracted a lot of attention as an atomic scale probe with applications in studying various surface structures such as, thin film surfaces and superlattice structures. The XRR technique is frequently employed in determining the thicknesses and electron densities and also, the root-mean-square (rms) roughness of the interfaces. Both thickness and roughness play crucial roles in the analysis of the magnetic property of the thin films. Before going straight into the present data analysis, a brief description of the method is given below.

In this section detailed findings from X-ray reflectivity (XRR) measurements of the thin films will be discussed. The X-ray reflectometry attracted a lot of attention as an atomic scale probe with applications in studying various surface structures such as, thin film surfaces and superlattice structures. The XRR technique is frequently employed in determining the thicknesses and electron densities and also, the root-mean-square (rms) roughness of the interfaces. Both thickness and roughness play crucial roles in the analysis of the magnetic property of the thin films. Before going straight into the present data analysis, a brief description of the method is given below.

Let the wave numbers in air, the film, and the substrate, as shown in Fig. 6.2, are respectively k_0 , k and k_S with $k = (k_0^2 - 4\pi\rho)^{1/2}$ and R_{12} and R_{23} represent the Fresnel

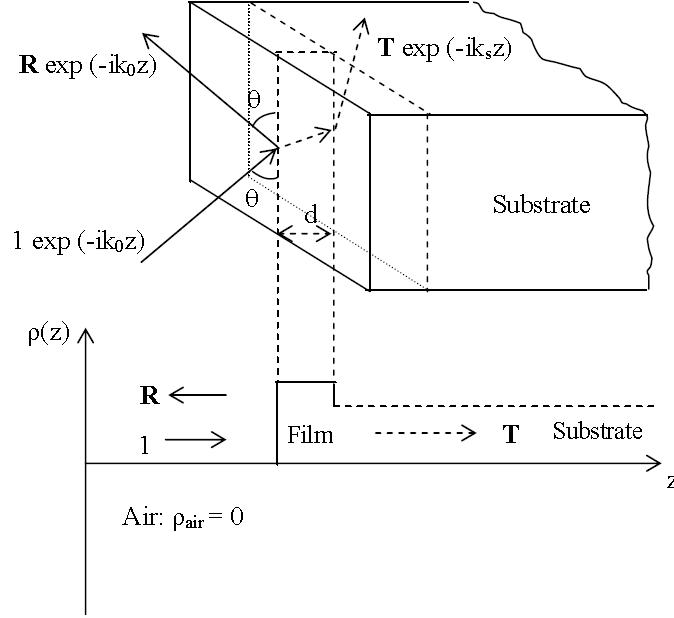


Figure 6.2: Schematic illustration (three dimensional view) of X-ray refraction from a uniform thin layer of thickness d on top of a substrate. The amplitude of the incident, reflected, and transmitted waves are respectively, 1, R and T . The bottom panel shows the corresponding one-dimensional variation of the scattering length density (SLD) profile from air to the film and the substrate.

reflectance, respectively at the air/film and film/substrate interface. The momentum is transferred along the surface normal and is given by $Q_Z = k_i - k_f = 2k \sin \theta$. Solving the wave equation for the three regions with proper boundary conditions one obtains the reflected amplitude R , given by

$$R = \exp(-2ik_0 d) \frac{R_{12} + R_{23} \exp(-2ikd)}{1 + R_{12} R_{23} \exp(-2ikd)}, \quad (6.6)$$

where $R_{12} = \frac{k_0 - k}{k_0 + k}$ and $R_{23} = \frac{k - k_S}{k + k_S}$ are the Fresnel coefficients at the respective interfaces. In this case also the critical point $k_0 = k_C$ is characterized by $k = 0$ and so $k_C = (4\pi\rho S)^{1/2}$. When $k_0 \leq k_C$, the reflectivity $|R|^2 \approx 1$. Beyond the critical point, i.e., for $k_0 > k_C$, the reflectivity falls off in an oscillatory manner, called the Kiessig Oscillation, which becomes clear from the large- Q behavior of the reflectivity. At large k_0 , the reflectivity is given by

$$|R|^2 \approx \frac{\pi^2}{k_0^2} [\rho^2 + (\rho_S - \rho)^2 + 2\rho(\rho_S - \rho) \cos(2k_0 d)], \quad (6.7)$$

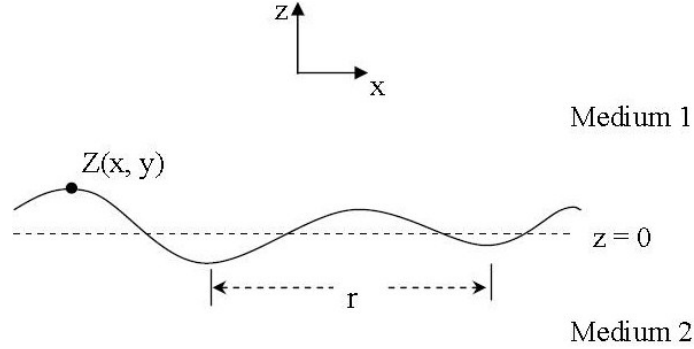


Figure 6.3: Schematic illustration of the surface or interface roughness.

with $Q_Z = 2k_0$ which implies that the reflectivity curve is oscillatory with its envelop falling off as Q_Z^{-4} . The period of oscillation actually determines the total thickness of the film. If Δk_0 is the difference between two adjacent peaks (between two successive minima or maxima), then the thickness $d \approx \frac{\pi}{\Delta k_0} = \frac{2\pi}{Q_Z}$. The intensity maxima occurs at the angular positions, θ_{im} , given by [151]

$$2d\sqrt{\sin^2\theta_{im} - \sin^2\theta_c} = m\lambda, \quad (6.8)$$

where m is an integer and it represents the order of the maxima. Since the incident angle is sufficiently small, the above equation can be reduced to the following approximate form

$$\theta_{im}^2 - \theta_c^2 = \left(\frac{\lambda}{2d}\right)^2 m^2. \quad (6.9)$$

This equation can be utilized in determining the critical angle θ_c and the film thickness from the plot of θ_{im}^2 vs. m^2 .

The roughness of the thin films reduces the reflected intensity, as the latter is highly sensitive to the structure projected to the surface normal (i.e., the electron density profile $\rho(z)$). The amount of reduction is actually a measure of the degree of roughness. The roughness for solid films can vary from a few Angstrom to a few tens of Angstroms in PLD grown samples. Thus, for proper interpretation of the X-ray reflectivity in such samples, it is very important to include the effect of roughness.

A rough interface between two homogeneous media is shown in Fig. 6.3, where $z = 0$ represents the interface with an average height Z_0 defined by

$$Z_0 = \int \int Z(x, y) dx dy. \quad (6.10)$$

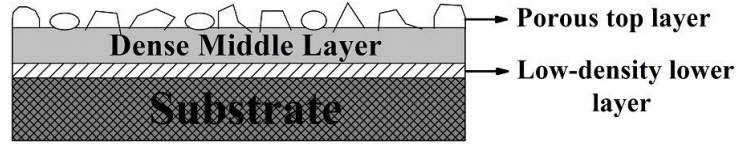


Figure 6.4: Schematic representation of the effective three-layer model to fit the reflectivity profiles.

The roughness σ is defined as the root mean square deviation of the height of the interface from the average height Z_0 and is given by

$$\sigma^2 = \int \int (Z(x, y) - Z_0)^2 dx dy. \quad (6.11)$$

For convenience, the vertical roughness is assumed to follow a Gaussian distribution with a standard deviation σ . So the scattering length density of the Gaussian interface will be an error function whose first derivative w. r. t the vertical depth z is a Gaussian function.

Depending on the growth direction, the interfacial roughness in multilayer structures can be divided into two main limiting cases as follows:

1. Correlated roughness: The roughness at successive interfaces almost mimics one another so that the roughness profiles at all the interfaces are the same.
2. Uncorrelated roughness: Interface roughnesses for successive layers are independent of each other.

Thickness, roughness, and density gradients are estimated analytically for all the thin films using XRR measurements. The XRR data are analyzed using the Parratt formalism to derive the electron density profile (EDP) across the depth of the film, their thickness and interfacial roughness. In this iterative fitting procedure, one starts with a model structure consisting of layers with different thickness, roughness, and density. If the fitting is not satisfactory one needs to refine the model by slicing the total film thickness in small sizes (Box model) [152, 153]. In this case the fit parameters, i.e., the thickness and the electron density of each layer, are allowed to vary in a controlled manner. The best fit gives the roughness convoluted electron density profile of the structure. A non-

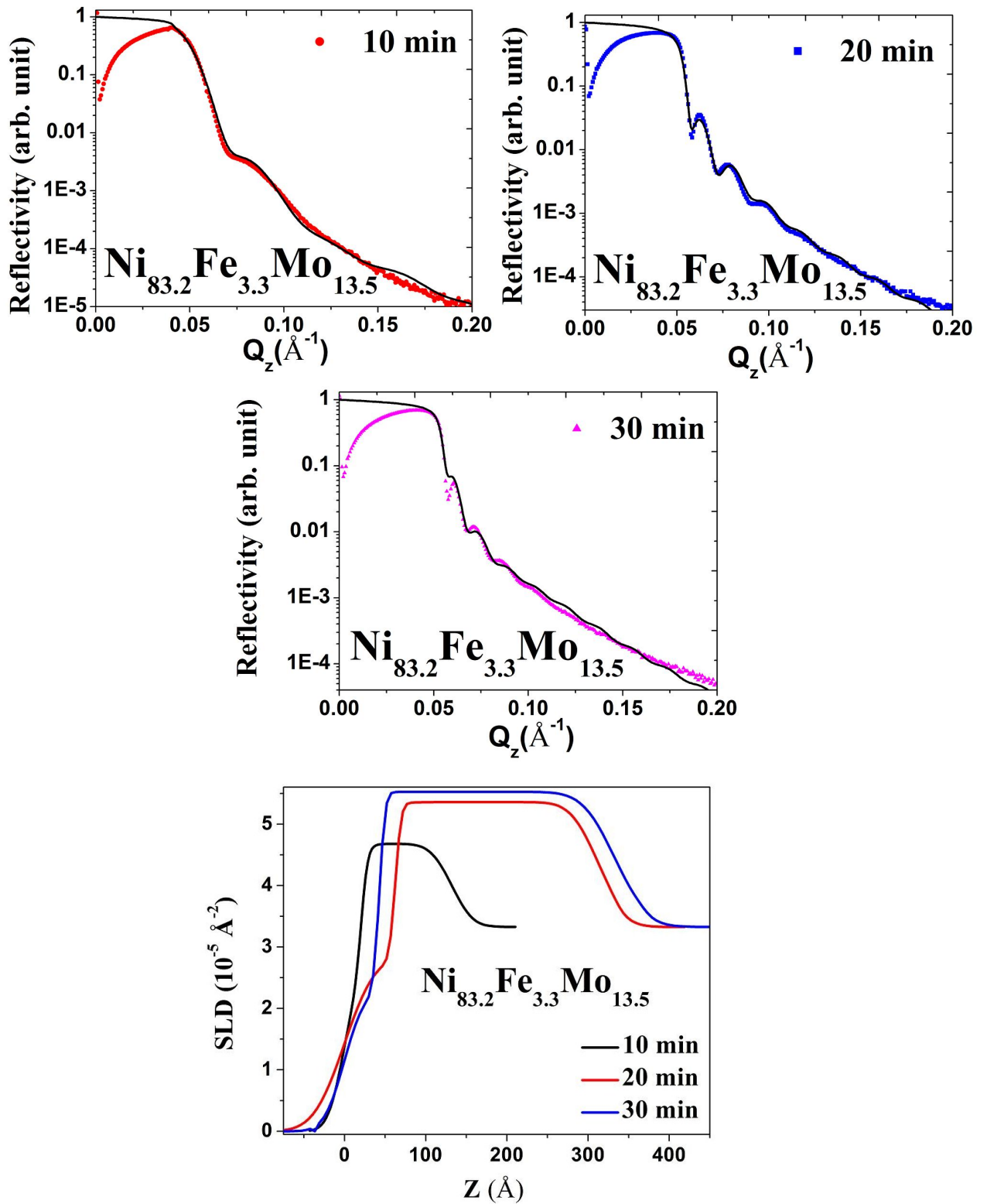


Figure 6.5: Reflectivity data (left panel) of samples of three thicknesses of $\text{Ni}_{83.2}\text{Fe}_{3.3}\text{Mo}_{13.5}$ films, the solid lines being the best-fitted curves using the tri-layer model. The scattering length density (SLD) of the structure as a function of thickness (right panel) for the same thin films.

linear least square-fitting algorithm is used to refine the electron density values by the χ^2 -minimization technique.

The best-fit model extracted by fitting the reflectivity data suggests that all films have three-layer structures consisting of one low density layer on top of the substrate followed by a thicker middle layer and again a topmost porous layer with the lowest density as shown in Fig. 6.4. It should be noted that the fitting of the reflectivity data is not possible if we remove any of the layers from the model. The best fits obtained are plotted in Fig. 6.5 for all the three films of $\text{Ni}_{83.2}\text{Fe}_{3.3}\text{Mo}_{13.5}$ alloy. It also shows the roughness convoluted scattering length density profile (SLDP) of the structure as a function of the thickness. The thicknesses derived using the Box model fits are given in Table 6.2.

Table 6.2 clearly shows nearly constant densities for the top and bottom layers, much lower than those of the respective bulk. For the middle layer the density is quite close to the bulk value with an increasing tendency for the thicker films. Whereas the average thickness of the top and bottom layers is ~ 3.5 nm, the thickness of the middle layer increases almost linearly with the deposition time. However, we believe that the exact linearity did not hold because the grains started to coalesce for the thickest film giving a thickness lower than what it should have been. The bottommost low density layer (~ 50 % of the bulk density) has high roughness due to the initial non-uniform coverage of the substrate. The density of the middle layer, having the lowest roughness, is approximately near the bulk value (~ 80 % of the bulk) and it increases with film thickness. The change in density is not due to the variation of composition; instead it is due to the variation of void densities in the layers. The topmost layer, having the lowest density (~ 30 % of the bulk) and the highest roughness, is interpreted as a porous layer which is also evident from the AFM images. The total thicknesses of the 3 films of $\text{Ni}_{83.1}\text{Fe}_{6.0}\text{Mo}_{10.9}$ are 17, 25, and 33 nm (see Table 6.2). These are not too different from the nominal values of 10, 20, and 30 nm, respectively. Earlier [154], Rai et al. found such differences for their NiMnSb films for thickness smaller than ~ 30 nm.

The thicknesses found from the present analysis will be further justified using some other techniques as well.

Table 6.2: Target composition, deposition time, thickness d, density ρ , and r.m.s roughness σ of three layers determined using Parratts fitting.

Target composition	Deposition time (min)		Low-density layer			Dense middle layer			Porous top layer		
	d (\AA)	ρ (g/cc)	σ (\AA)	d (\AA)	ρ (g/cc)	σ (\AA)	d (\AA)	ρ (gm/cc)	σ (\AA)		
Ni _{81.0} Fe _{16.7} Mo _{2.3}	10	34.2	4.39	17	98.3	6.31	4.3	36.2	2.98	19	
	20	39.7	4.36	20	176.2	6.92	5.8	22.7	4.01	10	
	30	41.3	4.38	22	254.1	7.23	7.3	31.3	3.67	13	
Ni _{80.4} Fe _{12.9} Mo _{6.7}	10	31.7	4.41	21	107.3	6.68	7.1	47.6	3.48	29	
	20	37.2	4.44	19	208.4	7.43	5.5	29.1	3.33	21	
	30	43.6	4.39	24	296.5	7.86	8.3	37.8	3.86	27	
Ni _{83.4} Fe _{10.7} Mo _{5.9}	10	25.8	4.43	12	105.2	6.74	7.2	44.5	2.87	22	
	20	42.5	4.24	32	183.7	7.13	9.1	32.1	3.71	17	
	30	22.8	4.69	7	353.1	7.39	4.0	27.3	3.46	11	
Ni _{83.1} Fe _{6.0} Mo _{10.9}	10	38.9	4.47	19	109.4	6.47	5.9	27.8	3.94	18	
	20	35.3	4.47	28	180.5	6.81	5.9	32.9	3.74	20	
	30	46.8	4.47	17	248.0	7.67	6.0	33.3	2.84	14	
Ni _{83.2} Fe _{3.3} Mo _{13.5}	10	38.3	4.47	21	111.3	6.32	6.1	20.9	3.67	16	
	20	24.0	4.66	26	248.8	7.27	5.7	62.6	3.94	30	
	30	37.2	4.58	31	289.7	7.47	5.7	42.8	3.14	20	

6.3.3 Rutherford Backscattering Spectroscopy

Conventional Rutherford backscattering spectroscopy (RBS) is a standard thin film analysis technique which offers relatively artifact-free quantitative information derived from first principles. It is extremely useful for depth profiling of multi-elemental thin films, stoichiometry and thickness determinations, impurity distributions [155], etc.

Rutherford differential scattering cross section $d\sigma(\theta)/d\Omega$, allows for quantitative determination of target composition as the amount of energy loss in the collision with the atomic nuclei depends on atomic number Z of each element present in the target material. The depth of the thin film is predicted from the average energy loss of an atom moving through a dense medium (concept of stopping cross-section). The amount of energy a projectile loses per unit distance traversed in a sample depends on the velocity of the projectile, the elements in the sample, and the density of the sample material. Typical energy losses for 2 MeV He^{2+} range between 100 and 800 eV nm^{-1} . The energy loss dependence on sample composition and density enables RBS measurements to estimate layer thickness, a process called depth profiling. A brief discussion of Rutherford backscattering from thin film is given below.

If a film is sufficiently thin, the energy loss in the layer is less than the experimental energy resolution. In this case, there is negligible change of scattering cross-section in the layer. If Q particles are incident at an angle α to the normal, as shown in Fig. 6.6, the effective thickness becomes $(\Delta t/\cos\alpha)$. If $d\Omega$ is the detector solid angle, $d\sigma(E)/d\Omega$ is the differential scattering cross-section, n is the number of atoms per unit volume ($= N\rho/M$) which can be obtained from Avogadro number N , density ρ , and atomic weight M of the target material, $n(\Delta t/\cos\alpha)$ = thickness of sublayer in atoms cm^{-2} , the number of counts (dQ) of backscattered particles or area under the peak is given by

$$dQ = Q\Delta\Omega \left(\frac{d\sigma(E)}{d\Omega} \right) \left(\frac{n\Delta t}{\cos\alpha} \right) \quad (6.12)$$

The convolution with experimental energy resolution can be done by assuming a Gaussian energy resolution function $f(x)$ with standard deviation w

$$f(x) = \left(\frac{1}{\sqrt{2\pi}w} \right) e^{-\left(\frac{(x-x_0)^2}{2w^2} \right)} \quad (6.13)$$

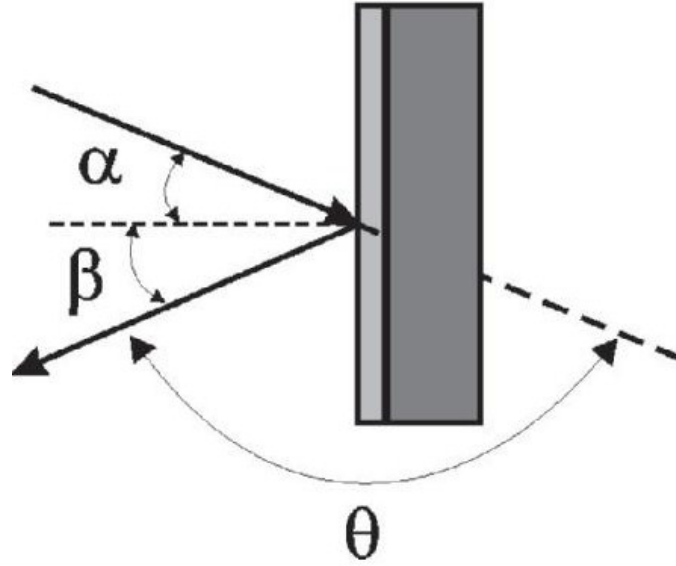


Figure 6.6: Instead of normal incidence, the ion beam is incident at an angle α .

The count density function is represented by

$$n(E) = \left(\frac{Q}{\sqrt{2\pi}w} \right) e^{-\left(\frac{(E-KE_0)^2}{2w^2} \right)} \quad (6.14)$$

where K is kinematic factor that depends on the mass of the incident particle and Count N_i in channel i,

$$N_i = \int_{E_i^{low}}^{E_i^{high}} n(E) dE \quad (6.15)$$

The height of the peak (H) is represented by

$$H = \frac{(d\sigma/d\Omega)\Delta\Omega Q\Delta E}{\varepsilon \sin\alpha} \quad (6.16)$$

The ratio of the spectrum heights for the two elements is given by The height of the peak (H) is represented by

$$\frac{H_A}{H_B} = \frac{\left(\frac{Z_A}{E_A} \right)^2 \varepsilon_B}{\left(\frac{Z_B}{E_B} \right)^2 \varepsilon_A} \quad (6.17)$$

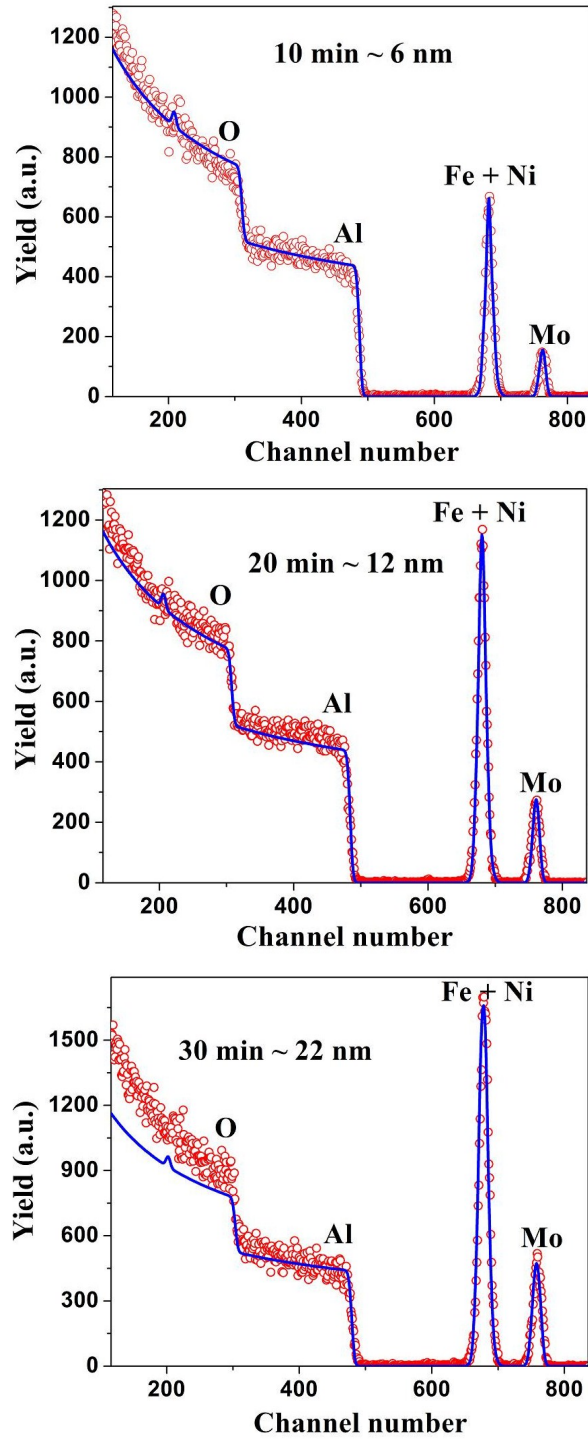


Figure 6.7: RBS spectra for three different thicknesses of Ni_{83.1}Fe_{6.0}Mo_{10.9} alloy (thickness ~ 6 nm, 16 nm, and 22 nm respectively) on Al₂O₃ substrate, recorded with a 2 MeV He²⁺ ion beam.

Figure 6.7 shows the RBS spectra for three different thicknesses of $\text{Ni}_{83.1}\text{Fe}_{6.0}\text{Mo}_{10.9}$ alloy films. There are two peaks, the small one corresponds to Mo and the tall one corresponds to both Ni and Fe. We can not resolve Fe and Ni peaks as their Zs are very close. The thickness is determined using simulation software GISA3. The spectra are fitted with trial values of thickness and composition till a good fit is obtained. No interface roughness is considered while fitting the data.

For this particular alloy films, the thicknesses are ~ 6 nm, 12 nm, and 22 nm for the 10 min, 20 min, and 30 min films, respectively. The thicknesses found from this method are $\sim 50\text{-}60\%$ of the thicknesses found from XRR analysis. The compositions of $\text{Ni}_{83.1}\text{Fe}_{6.0}\text{Mo}_{10.9}$ alloy thin films are found to be $\text{Ni}_{72}\text{Fe}_{20}\text{Mo}_8$ for both 10 and 20 min films whereas it is $\text{Ni}_{70}\text{Fe}_{20}\text{Mo}_{10}$ for the 30 min film. It is quite obvious that in the films Fe has grown more at the cost of Ni whereas Mo is about the same as in the bulk alloy. However, it is clearly seen in the RBS spectra (Fig. 6.7) that Fe and Ni peaks are almost on top of each other; hence their sum is much more reliable than the individual values. On the other hand Mo peak is very well separated in energy and hence its value is more accurate.

6.3.4 Atomic Force Microscopy

Atomic force microscopy (AFM) is an efficient tool to acquire information about the grain growth and surface morphology of any thin film sample. AFM can be used in both contact and non-contact modes. For the present work we have used the non-contact mode. Figure 6.8 shows typical AFM images of three different thicknesses of $\text{Ni}_{80.4}\text{Fe}_{12.9}\text{Mo}_{6.7}$ alloy thin films. The r. m. s roughnesses found from the images are 2.60 nm, 3.51 nm, and 5.06 nm for 10 min, 20 min, and 30 min films respectively using software SPIP. The AFM figures clearly show that on the surface of the film the grains are not sitting at the same height (porous surface). So our inclusion of a porous top layer in the three-layer model used for XRR analysis is indeed a correct input parameter. The roughness values found here are in reasonable agreement with those from XRR analysis. However, the difference is not unexpected since XRR scans the whole sample surface ($5\text{ mm} \times 5\text{ mm}$) whereas AFM does for a few patches (typically $1\ \mu\text{m} \times 1\ \mu\text{m}$).

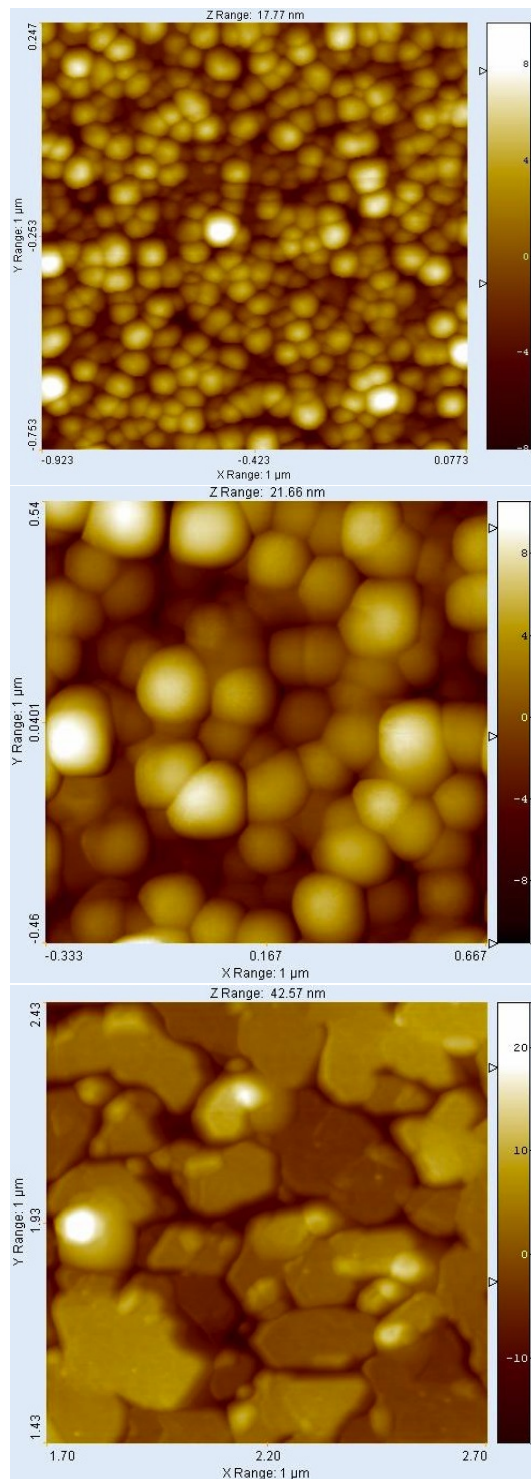


Figure 6.8: AFM images of 10 min, 20 min, and 30 min (top to bottom) films of $\text{Ni}_{80.4}\text{Fe}_{12.9}\text{Mo}_{6.7}$ alloy with a scan area of $1 \mu\text{m} \times 1 \mu\text{m}$. The r. m. s roughnesses are 2.60 nm, 3.51 nm, and 5.06 nm for 10 min, 20 min and 30 min films, respectively.

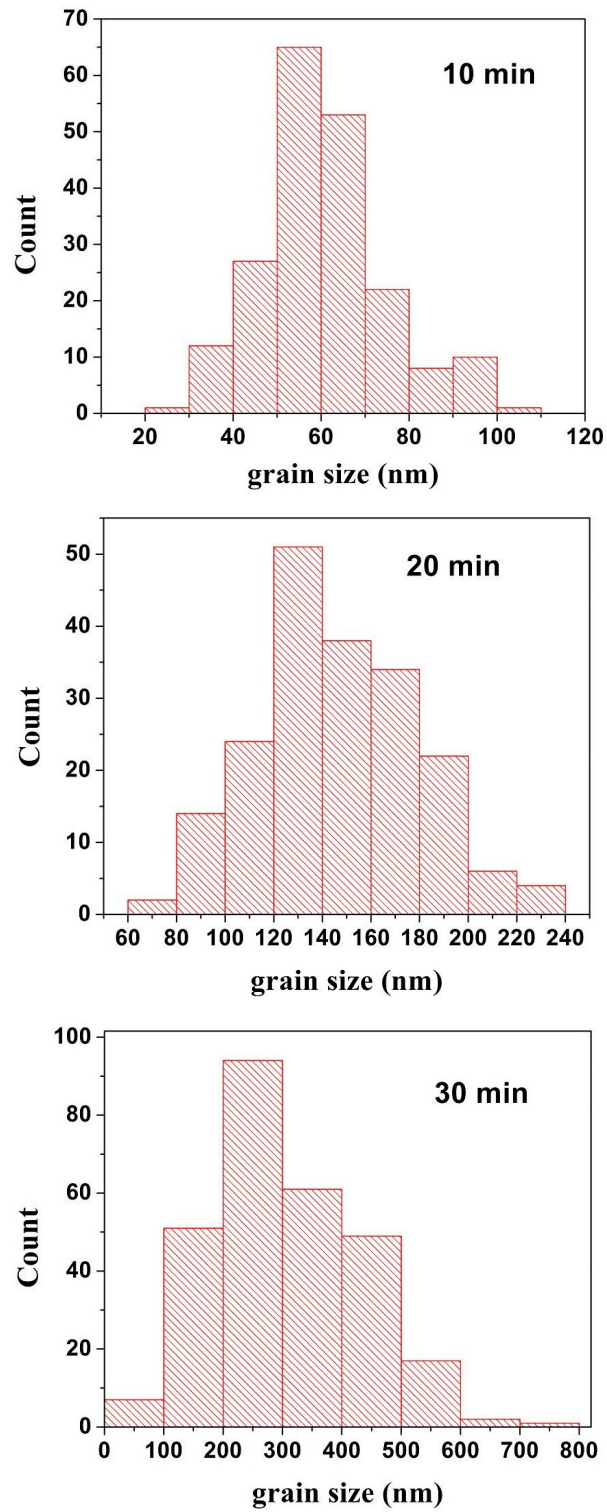


Figure 6.9: Grain size distribution of three different thicknesses of $\text{Ni}_{80.4}\text{Fe}_{12.9}\text{Mo}_{6.7}$ alloy films.

The scan size shown here are the same ($1\ \mu\text{m} \times 1\ \mu\text{m}$) for all the three thicknesses. We can see clearly from the AFM images that the grain size has increased and the inter-grain spacing has decreased with increasing thickness of the films. It can be clearly seen from Fig. 6.8 that in the 30 min film, the grains have started to coalesce. We have calculated the grain sizes for all the samples and they show a similar trend of increasing with thickness. Figure 6.9 shows the grain size distribution of the films shown in Fig. 6.8. The grain size is determined by line analysis method using Gwyddion software.

The volume average grain size found from XRD analysis is not in agreement with those found from the present analysis, though they show similar trends of increase in grain size with thickness. The AFM images show grain growth in X-Y plane of the sample, while even the thickest film (30 min) has a thickness of $\sim 30\ \text{nm}$ only. So we believe that the reason behind so widely different grain size found from XRD and AFM is, whereas the former gives the volume averaged grain size, the latter shows growth in XY plane. Moreover, we feel that the highly oriented growth of the film perpendicular to (111) plane gives rise to this anomaly.

6.3.5 Scanning Electron Microscopy

The energy dispersive X-ray spectra (EDXS) of the thin films are measured using scanning electron microscope (SEM) to determine the composition of the films and to compare them with those of the target alloys. Confirming compositions of thin films using this technique is not the best but still it can be effective if used in proper fashion. The main problem one faces is the huge intensity of the substrate peak in the spectra which introduces large errors in EDXS measurements in thin films. Our PLD grown films have a very few particulates on the surface resulting from the splashing effect (discussed in Chapter 2) in PLD films. The compositions of such particulates have been analyzed so that the substrate can not seriously affect the results. Then a few patches from the neighborhood of that particulate have been used for analysis. Interestingly, the particulates have the exact composition of the targets and the percentages of Ni, Fe, and Mo extracted from the film patches are also pretty close to those of the targets. Figure 6.10 shows the view of such a particulate on the surface of the 30 min film of $\text{Ni}_{83.4}\text{Fe}_{10.7}\text{Mo}_{5.9}$ and the corresponding spectrum found

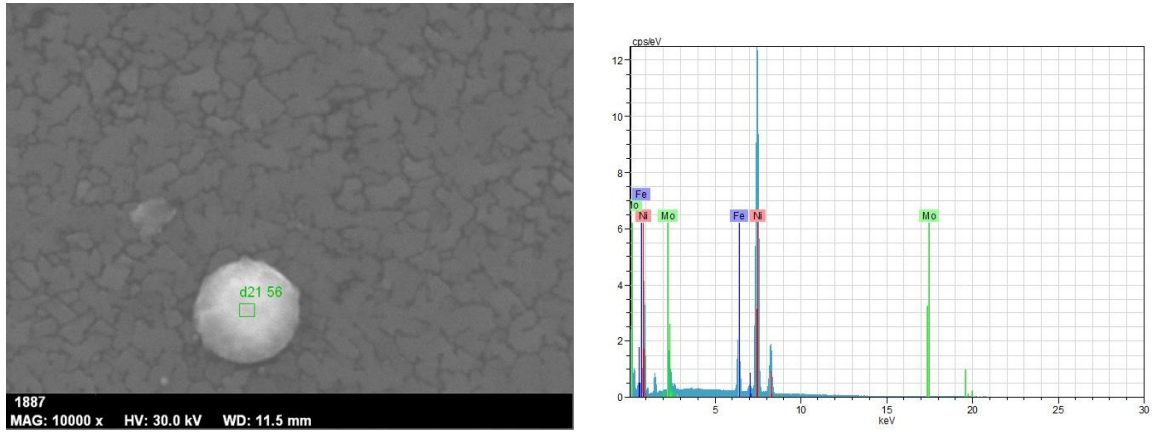


Figure 6.10: Scanning electron micrograph, analyzed at a resolution of 11.5 nm with 10000 X magnification, of 30 min film of $\text{Ni}_{83.4}\text{Fe}_{10.7}\text{Mo}_{5.9}$ (left) and the energy dispersive spectrum (right) measured for that particulate shown on the left.

from that particular particulate. The SEM image of this film exactly resembles its AFM image.

It can be clearly seen from the energy dispersive spectra (left panel of 6.10) that there is hardly any effect of substrate on the spectrum of that surface particulate and the analyzed composition fairly matches that of the bulk alloy. Similar results are found for the other samples. For $\text{Ni}_{83.1}\text{Fe}_{6.0}\text{Mo}_{10.9}$, a few patches around the particulate give quite similar composition of the films as found from RBS analysis and both indicate that the yield of Fe is higher at the cost of Ni than those of the target while the amount of Mo is quite similar. We believe that this information will help us in the analysis of the magnetic data. To make sure that there is no oxidation, XPS measurements on a couple of samples are carried out and hardly any oxide formation is found in the films. Also the compositions from XPS matches quite well with those of EDXS measurements.

The thickness of a thin film is an important parameter which affects its physical properties just as strongly as the composition and the grain growth. Though we have an estimate of the thicknesses of the films from the XRR analysis, still direct evidence can make us even more confident about our findings. For this purpose we have employed scanning electron microscope to get the cross-sectional view of one of the thickest samples as the resolution of the SEM is ~ 10 nm. The thickest film we have made is the 30 min

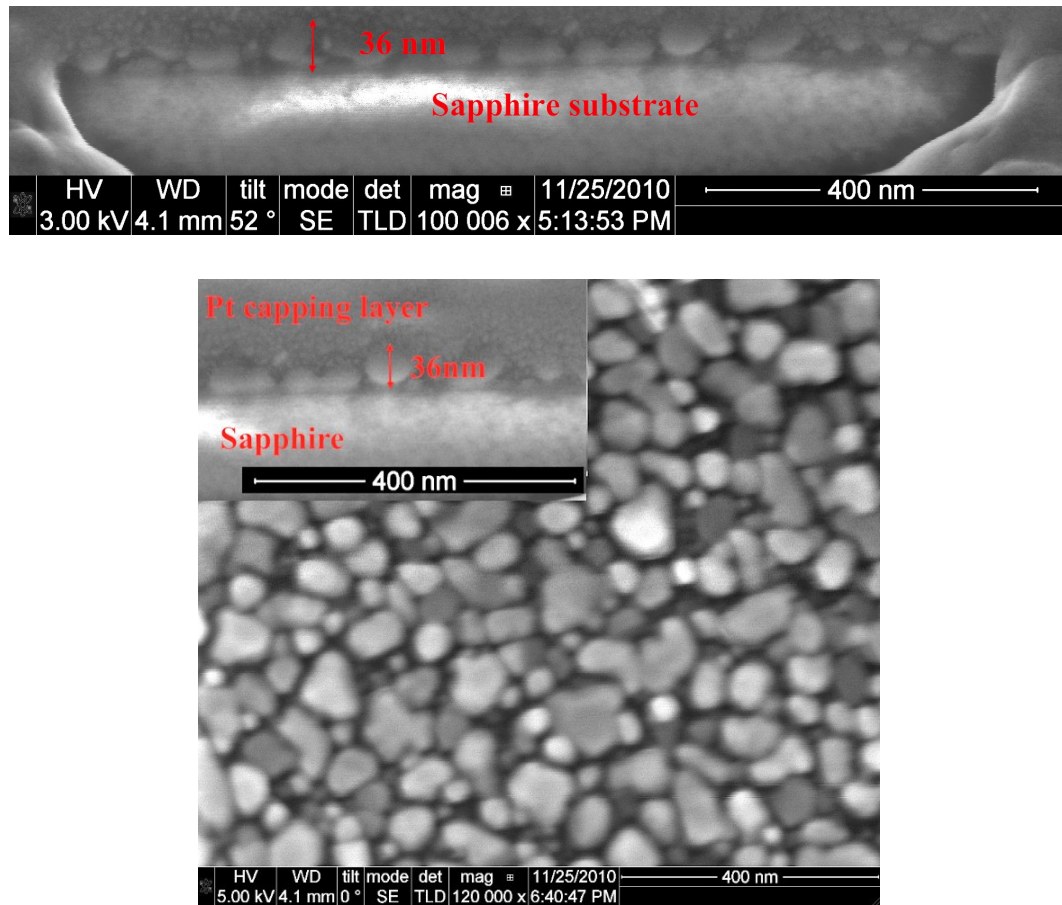


Figure 6.11: Scanning electron micrograph of the 30 min thin film of $\text{Ni}_{83.4}\text{Fe}_{10.7}\text{Mo}_{5.9}$ alloy. The background gives the planer view while the top left inset is the cross-sectional view with platinum capping layer. The thickness of the sample is 36 nm marked in both the cross-sectional images.

film of $\text{Ni}_{83.4}\text{Fe}_{10.7}\text{Mo}_{5.9}$ alloy (~ 40 nm from XRR). We have used focused ion beam (FIB) to get a fresh view of the cross-sectional plane, and we have coated the film surface with a 50 nm thick platinum using FIB to protect the thin film during milling. Figure 6.11 (top) shows a cross-sectional view from one edge of the thin film and (bottom) shows the planer view as the background, with the inset showing the cross-sectional view of the 30 min film of the $\text{Ni}_{83.4}\text{Fe}_{10.7}\text{Mo}_{5.9}$ alloy. The thickness of the film is ~ 36 nm which is in very good agreement with ~ 40 nm found from the XRR analysis.

A closer look at the cross-sectional views shows that there are a few grains on the

substrate with height less than 10 nm. Unlike the bigger grains which can be easily identified in the micrographs, they did not grow till the total thickness of the film. This observation justifies our consideration of a low-density lower layer in the three-layer model for XRR analysis. So our effective Box Model to fit the XRR data is a valid guess and hence we can take the thickness found from the XRR analysis as the true thickness of the films. We believe that it is really hard to see a prominent three-layer configuration in the cross-sectional view since in all the three layers the electron density is the same and hence it is difficult to get enough contrast to differentiate between the three distinct layers.

The structural characteristics of our Ni-Fe-Mo alloy thin films are listed below:

1. All of them are highly oriented in (111) direction.
2. The grain size increases with the thickness of the films.
3. The X-ray reflectivity data indicate that instead of one layer, the thin films comprise of three different layers where the middle layer mainly contributes to the film thickness.
4. The composition of the films shows while yield of Mo is pretty close to the target alloys but that of Fe is increased.

On the basis of these structural findings we will analyze the magnetization data of the thin films in the following section.

6.3.6 Magnetic Characterization

Magnetic properties in nanostructures are most of the time determined by their structural properties such as grain size, surface roughness, crystalline orientation, strain due to lattice mismatch with the substrate and many others. In the last section we have discussed the various techniques for collecting as much information as possible for the structural parameters of the Ni-Fe-Mo alloy thin films. Some of them are the aligned growth of the films from the XRD analysis, the XRR analysis reflecting a density gradient across the thickness of the films, the distribution of grain size found from AFM measurements, etc. All the above structural findings indicate that there is structural disorder due to nanosize

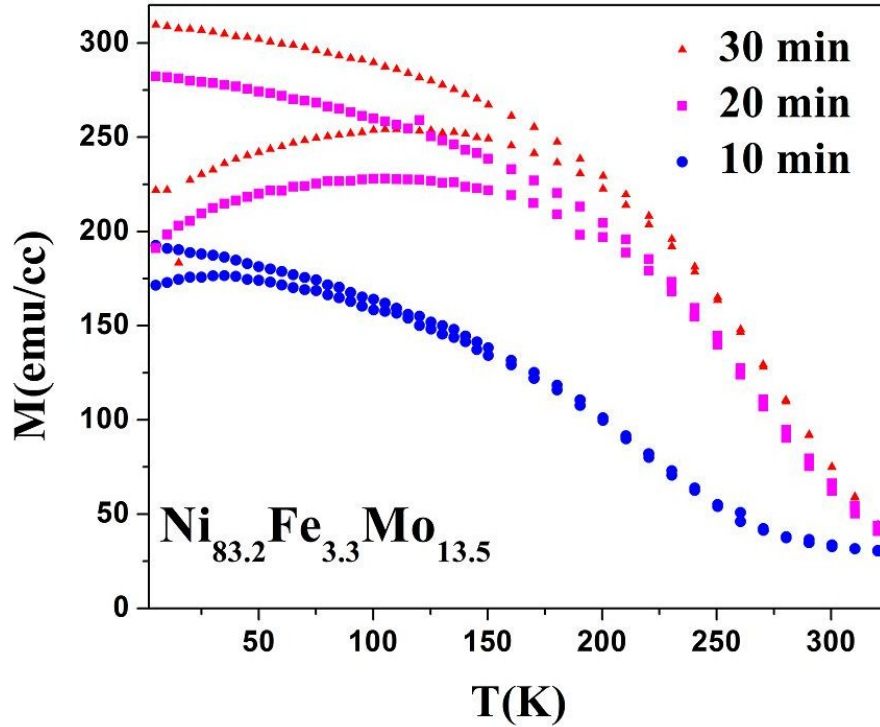


Figure 6.12: Zero-field-cooled (ZFC) and field-cooled (FC) $M(T)$ curves for the three thicknesses of the alloy $\text{Ni}_{83.2}\text{Fe}_{3.3}\text{Mo}_{13.5}$. The applied magnetic field is 200 Oe for the 10 min sample and 100 Oe for the two others.

grains, density gradient across the thickness, and very high void density, which in turn, increases the magnetic anisotropy and can completely or partially change the magnetic behaviors of these alloys in thin film forms. So we have studied dc magnetization of these thin films not only to characterize them but also to have an idea of the size dependence of magnetization in the presence of various structural disorders.

Magnetization as a function of temperature and magnetic field has been measured using a SQUID magnetometer in the RSO mode from 5 to 325 K but not beyond. Figure 6.12 shows the ZFC and FC curves for all the three thicknesses of $\text{Ni}_{83.2}\text{Fe}_{3.3}\text{Mo}_{13.5}$ alloy. The 20 and 30 min films have T_C s of ~ 275 K while for the 10 min film it is ~ 250 K, but all are much higher than the bulk T_C of ~ 44 K. Such is the case for the 3 films of $\text{Ni}_{83.1}\text{Fe}_{6.0}\text{Mo}_{10.9}$ alloy where $T_C \geq 325$ K as against the bulk T_C of ~ 182 K. Three other alloys have $T_C \gg 300$ K even in bulk forms, their thin films also show similar trend,

namely, $M(T)$ decreases by a few % only from 5 to 325 K implying T_C to occur much beyond. Figure 6.12 shows bifurcations at 150 - 250 K between ZFC and FC data of $\text{Ni}_{83.2}\text{Fe}_{3.3}\text{Mo}_{13.5}$ measured $\sim 100 - 200$ Oe. The coercive fields of $\text{Ni}_{83.2}\text{Fe}_{3.3}\text{Mo}_{13.5}$ alloy films are < 100 Oe at 5 K (shown later in this section) which is below the measuring fields for $M(T)$. Bifurcation between ZFC and FC curves is generally a characteristic feature of spin-glass systems, resulting from competing ferro- and antiferromagnetic pair interactions between the components, here Ni, Fe, and Mo. Even this bulk $\text{Ni}_{83.2}\text{Fe}_{3.3}\text{Mo}_{13.5}$ alloy has shown a mixed ferro-spin glass mixed phase although at much lower temperatures (below 10 K) as discussed in details in Chapter 3. Hence this high temperature spin-glass-like phase of this composition can not come from the competing pair interactions only. Moreover, for all other compositions and thicknesses, the FC and ZFC curves have shown similar bifurcations whereas their bulk counterparts have shown no such feature even at low temperatures. The peaks in ZFC $M(T)$ as well as the bifurcation temperatures move to higher temperatures for thicker samples. This is rather surprising since higher spin-glass transition temperature implies more disorder which is not expected in thicker samples. Such large variations could be again due to high lattice strain and substantial void densities in the films as well as the increase in Fe content at the cost of Ni as found in the compositional analysis using RBS and EDXS. We believe that the frustration that is reflected in the magnetic behaviour of all the thin films is due to their enhanced magnetic anisotropy induced by the structural disorder as elaborated above.

The spin wave analysis of the bulk magnetization data has shown clear effect of Fe-clustering in these alloys with reduced spin-wave stiffness constant for high Mo containing alloys. So we have tried a similar line of analysis for the thin films with large Mo content. The $M(T)$ data between 10 and 30 K ($\ll T_C$) fit quite well to the Blochs $T^{3/2}$ law and the spin-wave stiffness constant D is found to be ~ 157 and 195 meV \AA^2 for the thickest films of $\text{Ni}_{83.2}\text{Fe}_{3.3}\text{Mo}_{13.5}$ ($T_C \sim 275$ K) and $\text{Ni}_{83.1}\text{Fe}_{6.0}\text{Mo}_{10.9}$ ($T_C > 325$ K) respectively, as against 20 and 45 meV \AA^2 for the targets. Fig. 6.13 shows the $M(T)$ data of the thickest film of $\text{Ni}_{83.2}\text{Fe}_{3.3}\text{Mo}_{13.5}$ alloy fitted to Blochs $T^{3/2}$ law. The change in M is only 1 % in the range of fit and the average deviation of the data from the best-fitted curve is less than 0.01 %. Again this enhancement in the spin-wave stiffness constant compared to their bulk counterparts could very well be due to the high magnetic anisotropy in these

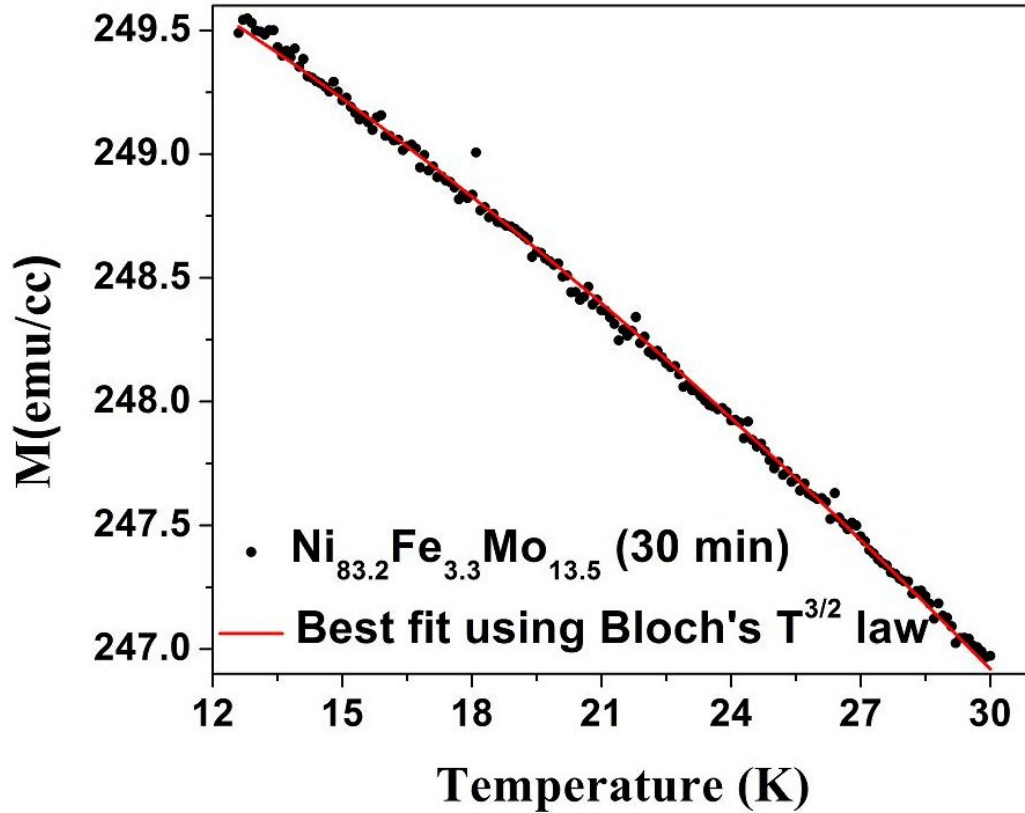


Figure 6.13: Magnetization vs. temperature of the thickest film of $\text{Ni}_{83.2}\text{Fe}_{3.3}\text{Mo}_{13.5}$ alloy where the red curve gives the best fit to Bloch's $T^{3/2}$ law. The spin wave stiffness constant $D = 157 \text{ meV } \text{\AA}^2$.

thin films.

Hysteresis loops, measured at 10, 100, 200, and 300 K for $\text{Ni}_{83.1}\text{Fe}_{6.0}\text{Mo}_{10.9}$ alloy, are shown in Fig. 6.14 (left panel). The coercive fields (HC), decreasing smoothly with increasing T , are $\sim 50 - 70 \text{ Oe}$ at 10 K as shown in Fig. 6.14 (right panel) for $\text{Ni}_{83.2}\text{Fe}_{3.3}\text{Mo}_{13.5}$ alloy and $\sim 90 - 120 \text{ Oe}$ for $\text{Ni}_{83.1}\text{Fe}_{6.0}\text{Mo}_{10.9}$ alloy (not shown). They are much larger than those of their bulk counterparts ($< 1 \text{ Oe}$); the increase could very well be due to internal strains induced from directional growth of the films as against the well-annealed bulk samples. M_r/M_S also decreases with temperature as expected but for the thinnest films of both the samples the curves are concave unlike the convex ones for the higher thicknesses. In other words, M_r/M_S has a much slower initial fall with temperature for the

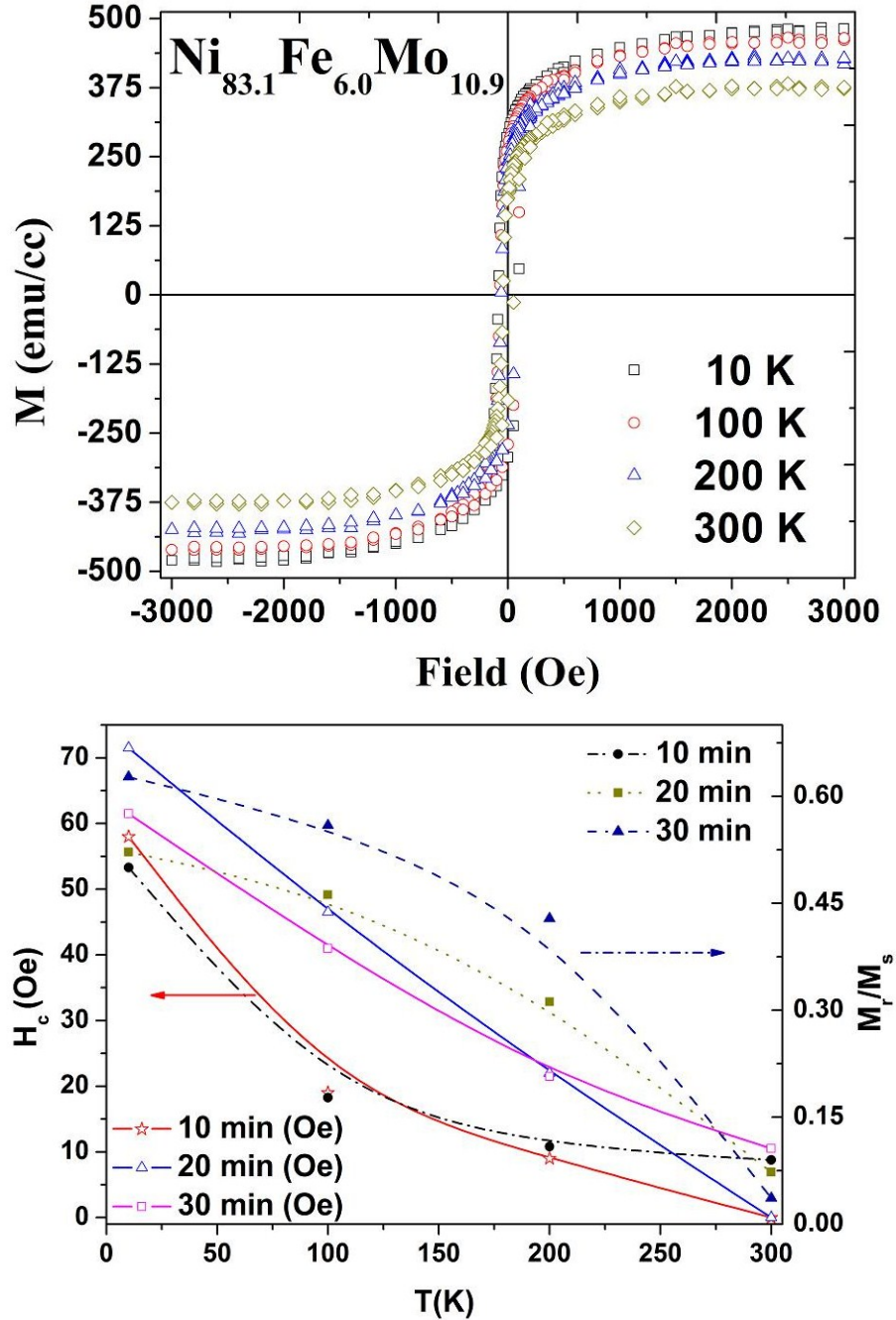


Figure 6.14: Magnetization vs. applied magnetic field at different temperatures for the thickest film of $\text{Ni}_{83.1}\text{Fe}_{6.0}\text{Mo}_{10.9}$ alloy (top panel). H_c and M_r/M_s as functions of temperature are plotted for all the three thicknesses of $\text{Ni}_{83.2}\text{Fe}_{3.3}\text{Mo}_{13.5}$ alloy (bottom panel).

Table 6.3: Target composition, their T_C , M_S , film deposition time, M_S at 10, 100, 200, and 300 K and $\Delta M/M(\%) = [M(10) - M(300)] \times 100/M(10)$.

Target Composition	T_C (K)	M_S (emu/cc)	Deposition Time (min)	M_S at 10 K (emu/cc)	M_S at 100 K (emu/cc)	M_S at 200 K (emu/cc)	M_S at 300 K (emu/cc)	$\Delta M/M$ (%)
$Ni_{81.0}Fe_{16.7}Mo_{2.3}$	720	705	10	361	349	332	317	12.2
			20	438	431	423	410	6.4
			30	472	454	449	437	7.4
			10	357	339	328	312	12.6
$Ni_{80.4}Fe_{12.9}Mo_{6.7}$	495	475	20	413	397	385	371	10.2
			30	445	431	427	409	8.1
			30	557	521	487	456	17.8
$Ni_{83.4}Fe_{10.7}Mo_{5.9}$	470	412	10	330	307	274	219	33.6
			20	467	436	403	379	18.8
$Ni_{83.1}Fe_{6.0}Mo_{10.9}$	182	238	30	483	456	426	375	22.4
			10	246	178	126	79	67.9
			20	272	241	191	83	69.5
$Ni_{83.2}Fe_{3.3}Mo_{13.5}$	45	71	30	306	287	236	152	50.3

thicker samples making them useful for magnetic applications till higher temperatures.

Table 6.3 gives the target composition, their T_C and M_S , film deposition time, film M_S at 10, 100, 200, and 300 K, obtained from $M(H)$ data taken with the film plane parallel to the magnetic field and the resulting $\Delta M/M(\%)$. M_S is calculated considering the total thickness from XRR measurements in computing the volume. So the values of M_S must have typically 20% error since we know that the films have high void densities. We again measure M (T) with the film plane perpendicular to the magnetic field where the demagnetization factor, N is ~ 1 and $M_S \sim H_{ext}$, and hence independent of the volume of the film. We now find, for example, that M_S of $Ni_{80.4}Fe_{12.9}Mo_{6.7}$ (30 min film) is 460 emu/cc as against 445 emu/cc as given in Table 6.3 above. So the thickness obtained from our XRR measurements is indeed meaningful. From Table 6.3 several points/conclusions naturally emerge:

1. Bulk $M_S = 796, 705, 475$ emu/cc for Mo = 0, 2.3, 6.7 %
 = 860, 412, 238, 71 emu/cc for Mo = 0, 5.9, 10.9, 13.5 %
 using M_S of $Ni_{80}Fe_{20} = 796$ emu/cc [156] and that for $Ni_{83}Fe_{17} = 860$ emu/cc [157].
 Obviously, increase of Mo and decrease of Fe, both cause a decrease of M_S .
2. As Mo increases (and Fe decreases) M of films is getting larger and larger (~ 4 times for Mo13.5) compared to the bulk value (say, by looking at only the 30 min films). More specifically, M_S for $Ni_{83.2}Fe_{3.3}Mo_{13.5}$ alloy thin film (30 min) is ~ 306 emu/cc as against ~ 71 emu/cc of the bulk. The corresponding numbers for $Ni_{83.1}Fe_{6.0}Mo_{10.9}$ are respectively, 483 and 238 emu/cc.
3. Both T_C and M increase in films from their bulk counterparts. Both 2 and 3 are easily understood in view of the fact that the composition of the films from both EDXS and RBS studies shows that while the Mo contents are pretty close to those of the target alloys Fe contents are much higher.
4. $\Delta M/M(\%)$ increases as expected with the increase Mo since T_C decreases with Mo addition. 5. For all temperatures, M increases with thickness (larger grains).

To conclude, PLD grown ferromagnetic thin films of different thickness from bulk Ni-Fe-Mo alloys films show highly oriented growth perpendicular to the (111) plane with

grain size increasing with thickness. The X-ray reflectivity data indicate that instead of a uniform density there are effectively three layers with density varying across the thickness. The RBS measurements of the films give thickness $\sim 50 - 60\%$ of that found from the XRR analysis. The AFM images give the average value of the roughness that is very similar to that calculated from the reflectivity data. The thickness found from the cross-sectional SEM image of the thickest sample shows good agreement with that estimated from the XRR analysis. The SEM image even supports the three-layer model used to analyze the XRR profiles. Both the RBS and EDXS measurements reveal that the targets and the corresponding films have somewhat similar compositions but with an enhanced yield of Fe, the Mo content almost remaining the same. Detailed analysis of magnetization data gives much higher values of T_C and D than those of the bulk targets. Low-field magnetization data show spin-glass-like features in all the films probably resulting from frustrations due to both compositional and structural disorder. Detailed analysis of magnetization data gives significantly higher values of T_C , D , and M_S in the films than those for the bulk samples. This could be understood in terms of the enhancement of Fe content in the films at the cost of Ni. Also, the magnetic anisotropy induced due to the structural disorder and strain in these films has largely affected their magnetic state (frustration) and properties, like say, H_C , in making them distinct from their bulk counterparts.

Chapter 7

Conclusions and Future prospects

In this Chapter, we shall summarize this thesis by highlighting our important findings followed by some future prospects. Our aim was to systematically study the changes in magnetism due to various kinds of disorder and its effects on the electrical transport properties of such systems through magnetization and electrical resistivity studies. In the following sections, we shall briefly describe the steps we followed to reach our goal.

7.1 Concluding Remarks

In Chapter 1 we have presented an overview of the different kinds of effects of disorder on magnetic as well as electrical transport properties. We have given brief description of some existing theories which guided us in our analysis of the magnetic as well as the transport data.

Chapter 2 describes the details of our sample preparation followed by a brief description of the pulsed LASER deposition technique which we have used to prepare our thin films, the working principle of Quantum Designs SQUID magnetometer which we used for our magnetic measurements, and finally the working principle of Quantum Designs physical property measurement system which we have used for electrical transport measurements in our samples.

In Chapter 3 we have discussed the effects of Mo/W substitution on a series of Ni-rich Ni-Fe-Mo and Ni-Fe-W disordered ternary alloys. In both the alloy series with increasing Mo/W and decreasing Fe, a sharp decrease in TC as well as Ms is indicative of the presence

of competing ferro- and antiferromagnetic interactions. There is hardly any hysteresis in the M-H loops of these alloys just like the parent permalloy compositions. From our analysis we have found the critical concentration ($T_C = 0$) for Mo-series to be ~ 14.2 at. % Mo and for W-series it is ~ 13 at. % W. One of the alloys in the Ni-Fe-Mo series with 13.5 at. % Mo has shown a low temperature mixed ferro-spin-glass phase unlike only a pure ferromagnetic phase in the other compositions of the series. Such a complex phase has not shown up in the case of W alloys, may be due to the lack of samples in the critical concentration region. Our experimental work has been supplemented by theoretical work from our group which predicts that there is a possibility of a spin-glass phase in the case of Ni-Fe-Mo alloys but not in Ni-Fe-W system.

Chapter 4 is a continuation our magnetization studies to find if there are any specific effects of Fe-dilution in these alloys. So we have analyzed high-resolution low-temperature high-field magnetization data and found that the finite-temperature spin dynamics in the two alloy systems is indicative of a broad distribution of magnetic spin interactions between the magnetically active Fe atoms. We have also analyzed the magnetization data taken at various magnetic fields and temperatures close to T_C and found the critical exponents associated with the phase transition for high Mo/W content alloys. We have seen all the three macroscopic magnetization characteristics, the spin-wave parameter B , the reduced coefficient $B_{3/2}$, and the critical amplitudes Γ^{-1} yield distinctive spin dynamics signatures associated with strongly coupled cluster spins in these alloys. The sharp enhancement in B accompanying the spin stiffness reduction with Fe dilution clearly indicates weakened bulk spin couplings and softening of low-energy spin-wave modes. Furthermore, the magnitude of $B_{3/2}$ rapidly approaches 1 with increasing Fe dilution, and the slower magnetization decay with temperature indicates presence of strongly coupled cluster spins which resist thermal demagnetization and stretch the magnetic order near T_C . Except for the Mo13.5 alloy, which has a spin-glass phase below $T_g = 10$ K, all the other samples gave quite reasonable values of the critical exponents. Non-universal values of critical exponents with $\beta \sim 0.55$ (Mo13.5) have also been found in recent experimental studies of the ferromagnetic transition in re-entrant metallic spin-glass $\text{Au}_{81}\text{Fe}_{19}$ alloy.

In Chapter 5 we have presented electrical resistivity data of three different kinds of disordered systems including Ni-rich disordered Ni-Fe-V/Mo/W alloys, a set of Co-rich

Ni-Cr pseudo binary ferromagnetic amorphous alloys and pulsed LASER deposited self assembled Ni nanocrystallites on TiN matrix. Our choice of such systems is not arbitrary; all these disordered systems show low-temperature resistivity minima and they are all ferromagnetic. We have been able to identify various scattering mechanisms attributed to the electrical resistivity of these systems. The resistivity minima are ascribed to weak localization and electron-electron interference effects and show a prominent $-\sqrt{T}$ dependence below the resistivity minima at T_{\min} . for all the three kinds of disordered systems. The electronmagnon scattering strength shows a tendency to increase with increasing Fe dilution in case of ternary alloys, which we believe is due to the strongly coupled Fe spins in the alloys as found in their magnetization behavior. Also there is an increase in the coefficient of the $-\sqrt{T}$ term (e-e interaction) in $\rho(T)$ with increasing V, Mo, and W which is expected from the enhanced electron localization due to increased disorder in the alloys. The derived Debye temperatures are quite reasonable when compared with those of similar ternary alloy systems. In case of amorphous alloys we could satisfactorily isolate the contributions to the resistivity from the temperature dependence of dynamical structure factor as well as electron-magnon scattering. Finally, in the case of Ni-nanocrystallites, the temperature dependence of $\rho(T)$ is mainly dictated by that of Ni and the residual resistivity wholly comes from the almost temperature-independent resistivity of TiN. Here also we find that apart from electron-phonon scattering there is a substantial amount of contribution to the resistivity due to electron-magnon scattering.

Chapter 6 has been devoted to the structural as well as magnetic characterization of pulsed LASER deposited nanometer size Ni-Fe-Mo alloy thin films which due to their low magnetostriction are useful for applications in micro-electro-mechanical systems. After successful characterizations of the bulk Ni-Fe-Mo alloys our aim was to study the effect of size reduction on their magnetic behavior. We have used the alloy buttons as targets and single crystal sapphire as substrates to prepare thin films of three different thicknesses in order to study the thickness dependence of magnetization as well. The nominal thicknesses chosen for present study are 10, 20 and 30 nm. We have used various techniques for structural characterization of the films which would give us a fair idea about the degree of structural disorder in these films. The X-ray diffraction patterns suggest that all the films are highly textured and oriented along (111) direction. The broadening of the XRD

lines with thickness indicates increase in grain size with thickness and presence of strain in the films as well. The thickness, roughness, and density of the films are calculated from their X-ray reflectivity data. All the films show a trend of three layers instead of a single layer; the change in density of the thin films is due to high void density. The surface morphology has been studied using an atomic force microscope. We can clearly see from the micrographs the increase in grain size with increasing thickness and the roughness calculated compares well with those found from the XRR analysis. We have also studied the thickness and composition of the films using Rutherford back scattering, the thicknesses found in this method are lower than what we have found in XRR analysis. The calculated compositions roughly match with those of the targets with a tendency of yielding higher Fe at the expense of Ni. We could only roughly estimate Ni and Fe contents since in RBS we can not resolve the peaks of Ni and Fe but could quite accurately obtain the Mo content in the films. They are found to be pretty close to the target compositions. Scanning electron microscope is also used to have a rough idea about the compositions of the films. We have taken a cross-sectional image of our thickest thin film, i.e., 30 min film of $\text{Ni}_{83.4}\text{Fe}_{10.7}\text{Mo}_{5.9}$ to check whether XRR or RBS gives better estimates of the thickness. We have found that not only our XRR thicknesses are correct but also the three-layer model used to analyze the XRR data is quite logical. Next we have interpreted the magnetization data of these films keeping in mind the structural findings. The low-field ZFC and FC curves show bifurcations for all the thin films which indicate frustrations in the systems. The M-H loops show much higher coercivity than their bulk counterparts. Only two bulk alloys have T_C lower than 300 K, but in case of thin films only the films of $\text{Ni}_{83.2}\text{Fe}_{3.3}\text{Mo}_{13.5}$ alloy have T_C lower than 300 K but its value is ~ 5 times higher than that of the bulk alloy. The spin-wave stiffness constants have also been found to increase as compared to their bulk counterparts. All these differences in the magnetization behavior are expected due to the structural disorder of the films which increases their magnetic anisotropy. The bifurcations between the ZFC and FC curves are common feature of the spin-glass phase where the reason is competing ferro- and antiferromagnetic interactions in the systems, but here in these films the reason of such bifurcations for all the compositions must be coming from the highly textured films having high void densities due to island-kind growth. The enhancement in the Curie temperature is ascribed to the increase in

Fe content of the films besides the magnetic anisotropy due to structural disorder. The grain size found here is much smaller than the magnetic domains found in bulk materials which must also have an effect on the magnetic behavior. The increment of Fe content also explains the higher spin-wave stiffness constants found here. We have also seen in Chapter 4 that Fe dilution sharply decreases the spin-wave stiffness constants in these alloys.

So in this thesis we have not only been able to characterize a few disordered systems but also successfully analyzed and interpreted the experimental results using existing theories.

7.2 Future Directions

As far as the magnetization studies are concerned we have satisfactorily addressed most of the important issues. However, in the case of electrical transport, a detailed study of magnetoresistance and Hall effect of these disordered ternary alloys could give us more insight to the various scattering mechanisms involved. It could also support the findings of the resistivity analysis. Then looking at the application potential of the magnetic thin films, a rigorous study of the electrical transport properties of Ni-Fe-Mo alloy films could be very interesting as well as useful. Looking at these possibilities we can address the following problems in future:

1. Studies of magnetoresistance of bulk Ni-Fe-Mo/W alloys as well as their thin films and find the effect of size reduction on magnetoresistance of these systems besides verifying the findings of the electrical resistivity of the present work.
2. Studies of Hall resistivity of bulk Ni-Fe-Mo/W alloys as well as their thin films and find the effect of size reduction on Hall resistivity and try to find the respective scaling exponents for these systems.
3. Studies of the magnetic properties of the Ni-Fe-Mo thin films after annealing them at some higher temperatures. This will possibly reduce the strain in the films and lower the disorder.

4. Preparation of magnetic alloy thin films by varying initial conditions and improving them for application purpose. Looking at the present interest of application oriented materials science; patterned thin films are good systems to study.
5. Detailed structural characterization of the thin films using STEM, looking at the fact that the structural properties have large impacts on the magnetic properties of the thin films.

Bibliography

- [1] C. Kittel, The introduction to Solid State Physics, 7th Edition (John Wiley Sons., New York, 1953).
- [2] B. D. Cullity, Introduction to Magnetic Materials, Addison-Wesley Publishing Company. Reading, MS,1972, p.134.
- [3] G. A. Petrakovskii, Sov. Phys. Usp **24**, 511 (1981).
- [4] A. H. Morrish, The Physical Principles of Magnetism (John Wiley Sons., 1965).
- [5] S. Chikazumi, Physics of Magnetism (John Wiley Sons., 1964).
- [6] J. Crangle, The Magnetic Properties of Solids (The Structures and Properties of Solids, Vol. 6, Edward Arnold, London 1977).
- [7] G. Toulouse, Comm. Phys. **2**, 115 (1977).
- [8] J. Mydosh, Spin Glasses: An Experimental Introduction (Taylor and Francis, London, Washington DC, 1983).
- [9] Peter J. Ford, Cont. Phys. **23**, 141 (1982).
- [10] V. Canella and J. A. Mydosh, Phys. Rev. B **6**, 4220 (1972).
- [11] C. N. Guy, Physica **86**, 877 (1977); J. Phys. F : Metal Phys. **7**, 1505 (1977).
- [12] J. L. Tholence and R. Tournier, J. Physique C **35**, 229 (1974); Physica B **86**, 873 (1977).
- [13] J. S. Kouvel, J. Phys. Chem. Solids **24**,795 (1963).

- [14] C. N. Guy, J. Phys. F : Metal Phys. **8**, 1390 (1978).
- [15] S. P. McAlister and C. M. Hurd, Phys. Rev. Lett. **37**, 1017 (1976).
- [16] S. P. McAlister, J. Appl. Phys. **49**, 1616 (1978).
- [17] D. L. Martin, Phys. Rev. B **20**, 368 (1979); *ibid* **21**, 1902 (1980); *ibid* 1906 (1980).
- [18] J. A. Mydosh, Amorphous Magnetism II, edited by R. A. Levy and R. Hasegawa (Plenum, 1977), P.73.
- [19] A. P. Murani, J. Magn. Magn. Mater. **5**, 95 (1977).
- [20] A. P. Murani, J. Physique C **6**, 1517 (1978).
- [21] J. Souletie and R. Tournier, J. Low Temp. Phys. **1**, 95 (1969).
- [22] S. F. Edwards and P. W. Anderson, J. Phys. F **5**, 965(1975); *ibid* **6**, 1927 (1976).
- [23] D. Sherrington and S. Kirkpatrick, Phys. Rev. Lett. **35**, 1792 (1975).
- [24] J. R. L. de Almeida and D. J. Thouless, J. Phys. A **11**, 983 (1978).
- [25] D. J. Thouless, P. W. Anderson, and R. G. Palmer, Phil. Mag. B **23**, 1371 (1981).
- [26] D. S. Fisher and D. A. Huse, Phys. Rev. Lett. **47**, 201, (1986); Phys. Rev. B **38**, 386 (1988).
- [27] A. P. Malozemoff and B. Barbara, J. Appl. Phys. **57**, 3410 (1985).
- [28] B. R. Coles, B. R. Sarkissian, and R. H. Taylor, Phil. Mag. B **37**, 489 (1978).
- [29] A. Banerjee and A. K. Majumder, Phys. Rev. B **46**, 8958 (1992).
- [30] A. K. Majumdar and P. V. Blanckenhagen, Phys. Rev. B **29**, 4079 (1984).
- [31] A. Z. Menshikov, G. A. Takzey, and A. Ye. Teplylykh, Phys. Met. Metall. **54**, 41 (1982).
- [32] R. G. Alikev, T. D. Chemang, J. S. Kouvel, and H. Hurdequint, J. Magn. Magn. Mater. **30**, L1, (1982).

- [33] L. M. Kistler and S. M. Bhagat J. Phys. C **15**, L929 (1892).
- [34] V. Manves, R. A. Brand, W. Kenne, and R. Marx, Solid State Commum. **48**, 811 (1983).
- [35] F. Bloch, Z. Physik, **61**, 206 (1930).
- [36] F. Keffer, in Encyclopaedia of Physics, edited by H.P.J. Wijn (Springer, Berlin, 1966) Vol. **XVIII**, part 2, p.l.
- [37] C. Kittel, Quantum theory of Solids (John Wiley Sons, New York, 1963).
- [38] F.J. Dyson, Phys. Rev. **102**, 1217, 1230 (1956).
- [39] T. Izuyama and R. Kubo, J. Appl. Phys. **35**, 1074 (1964).
- [40] F. Bloch, Z. Phys. **57**, 545 (1929).
- [41] J. C. Slater, Phys. Rev. **49**, 537 (1936).
- [42] E. C. Stoner, Proc. Roy. Soc. A **165**, 372 (1938); *ibid* **169**, 339 (1939).
- [43] E.P. Wohlfarth, J. Appl. Phys. **39**, 1061 (1968); Inst. Phys. Conf. Series **55**, 165 (1980); Handbook of Ferromagnetic Materials, **1**, 1 (1980); J. Magn. Magn. Mater. **45**, 1(1984).
- [44] D. M. Edwards and E.P. Wohlfarth, Proc. Roy. Soc. A **303**, 127 (1968).
- [45] E. D. Thomson, E.P. Wohlfarth and C. Bryan, Proc. Phys. Soc. **83**, 59 (1964).
- [46] C. Herring and C. Kittel, Phys. Rev. **81**, 869 (1951); C. Herring, Phys. Rev. **85**, 1003 (1952); *ibid* **87**, 60 (1952).
- [47] J. Mathon and E.P. Wohlfarth, Proc. Roy. Soc. A **302**, 409 (1968).
- [48] H. E. Stanley, Introduction to Phase Transitions and Critical Phenomena (Clarendon Press. Oxford. 1971).
- [49] S. K. Ma, Modern Theory of Critical Phenomena (W.A. Benjamin, Inc. London, 1976).

- [50] F. J. Wegner, Phys. Rev. B **5**, 4529 (1972); in Phase Transitions and Critical Phenomena, edited by C. Domb and M.S. Green (Academic Press, New York, 1976), Vol.**6**, p.7.
- [51] M. E. Fisher, Rev. Mod. Phys. **46**, 597 (1974).
- [52] S. N. Kaul, Phase Transitions **47**, 23 (1994) and references cited therein.
- [53] S. N. Kaul, J. Magn. Magn. Mater. **53**, 5 (1985).
- [54] A. Arrott and J.E. Noakes, Phys. Rev. Lett. **19**, 786 (1967).
- [55] S. N. Kaul, Phys. Rev. B **38**, 9178 (1988).
- [56] A. Aharony and M.E. Fisher, Phys. Rev. B **27**, 4394 (1983).
- [57] P. A. Lee and T. V. Ramakrishnan, Rev. Mod. Phys. **57**, 287 (1985).
- [58] M. A. Howson and B. L. Gallagher, Physics Reports **170**, 265 (1988).
- [59] J. S. Dugdale, Contemp. Phys. **28**, 547 (1987).
- [60] J. H. Mooij, Phys. Stat. Sol. A **17**, 321 (1973).
- [61] J. S. Dugdale in The Structures of Properties of Solids 5 The Electrical Properties of Metals and Alloys (Edward Arnold, London, 1977).
- [62] N. F. Mott, Proc. Phys. Soc. **47**, 571 (1935); Proc. Roy. Soc. (London) A **153**, 699 (1936).
- [63] A. H. Wilson, Proc. Roy. Soc. (London) A **167**, 580 (1938).
- [64] J. M. Ziman Phil. Mag., **6** 1013 (1961).
- [65] B. Sas, T. Kemeny, J. Joth, and F. I. B. Williams, Mat. Sci. rt Engg., **99**, 223 (1988).
- [66] R. Evans, D. A. Greenwood and P. Lloyd, Phys. Lett. A, **35**, 57(1971); *ibid* **38**, 151(1972).

- [67] P. J. Cote and I. V. Meissel, "Glassy Metals I", edited by H - J Guntherodt and H. Beck, Springer-Verlag, Berlin, 141 (1983).
- [68] S. R. Nagel, Phys. Rev.B, **16**, 1694 (1977); P. J. Cote and L.V. Meissel, Phys. Rev. Lett., **39**, 102 (1977).
- [69] D. Markowitz, Phys. Rev. B **15**, 3617 (1977).
- [70] R. Richter, M. Wolf and F. Goedsche, Phys. Stat. Sol. B **95**, 475 (1979); R. Richter and F. Goedsche, Phys. Stat. Sol. B **123**, 143 (1984).
- [71] S.N. Kaul, W.H. Kettler and M. Rosenberg, Phys. Rev. B **33**, 4987 (1986); S.N. Kaul, W.H. Kettler and M. Rosenberg. Phys. Rev. B **35**, 7153 (1987).
- [72] J. Kondo, Solid State Physics Vol.23, edited by F. Seitz, D. Turnbull and H. Ehrenreich (Academic Press, New York, 1969), p. 184.
- [73] D.R. Hamann, Phys. Rev. **158**, 570 (1967).
- [74] E. Abrahams, P.W. Anderson. D. C. Licciardello and T. V. Ramakrishnan, Phys. Rev. Lett. **42**, 673 (1979).
- [75] B.L. Altshuler and A.G Aronov, "Electron-Electron Interactions in Disordered Systems" edited by F L Efros and M Pollak, Elsevier, New York 1(1985).
- [76] G Bergmann, Phys. Rep.. **107**, 1 (1984).
- [77] S. Chakraborty, A. K. Majumdar, J. Magn. Magn. Mater. **186**, 357 (1998) and references cited therein.
- [78] A. K. Gangopadhyay, R. K. Ray, A. K. Majumdar, Phys. Rev. B B **30**, 1801 (1984) and references cited therein.
- [79] R. M. Bozorth, Rev. Mod. Phys. **25**, 42 (1953).
- [80] W. P. Taylor, M. Schneider, Henry Baltes, and M. G. Allen Electrochemical and Solid-State Letters, **2** (12), 624 (1999); P. Esther, C. J. Kennady, P. Saravanan, and T. Venkatachalam, J. Non-Oxide Glasses, **1**(3), 301 (2009).

- [81] Anup Gangopadhyay, Ph.D. Thesis, Indian Institute of Technology, Kanpur, India, (1992).
- [82] Swapan Chakraborty, Ph.D. Thesis, Indian Institute of Technology, Kanpur, India, (1998).
- [83] Pulsed Laser Deposition of Thin Films, edited by D. B. Chrisey and G. K. Hubler (John Wiley, New York, 1994).
- [84] H. P. R. Willmott and J. R. Huber, *Rev. Mod. Phys.* **72**, 315 (2000).
- [85] D. Dijkkamp, T. Venkatesan, X. D. Wu, S. A. Shareen, N. Jiswari, Y. H. Min-Lee, W. L. McLean, and M. Croft, *Appl. Phys. Lett.* **51**, 619 (1987).
- [86] A. Inam, M. S. Hegde, X. D. Wu, T. Venkatesan, P. England, P. F. Miceli, E. W. Chase, C. C. Chang, J-M. Tarascon, and J. B. Wachtman, *Appl. Phys. Lett.* **53** 908 (1988).
- [87] C. Scarfone, M. G. Norton, C. B. Carter, J. Li, and H. W. Mayer, *Mat. Res. Soc. Symp. Proc.* **191**, 183 (1991).
- [88] R. K. Singh and J. Narayan, *Phys. Rev. B* **41**, 8843 (1990).
- [89] B. Holzapfel, B. Roas, L. Schultz, P. Bauer, and G. Saemann-Ischenko, *Appl. Phys. Lett.* **61**, 3178 (1992).
- [90] J. Tamaki, S. Nakayama, M. Yamamura, and T. Imanaka, *J. Mat. Sci.* , **24**, 1582 (1989).
- [91] K. Oda, H. Yata, T. Yoshio, K. O-Oka and K. Oda, *J. Mat. Sci.* **21**, 637 (1986).
- [92] J. M. Mwabora and R. T. Kivaisi, *J. Mat. Sci. Mat. Elec.*, **12**, 75 (2001).
- [93] J.M. van Hove and P.I. Cohen, *Appl. Phys. Lett.*, **47**, 726 (1985).
- [94] R. G. Humphreys, J. S. Satchell, N. G. Chew, J. A. Edwards, S. W. Goodyear, S. E. Blenkinsop, O. D. Dosser, and A. G. Cullis, *Supercond. Sci. Technol.* **3**, 38 (1990).

- [95] M. McElfresh, Fundamentals of Magnetism and Magnetic Measurements, Technical Resources from Quantum Design, San Diego, CA 92121-3733, USA (2000).
- [96] Physical Property Measurement System Manual, Quantum Design, San Diego, USA (2002).
- [97] Pradip Khatua, Ph.D. Thesis, Indian Institute of Technology, Kanpur, India, (2006).
- [98] S. Chikazumi, Physics of Magnetism (Wiley, New York, 1964) p. 73.
- [99] H. Ashworth, D. Sengupta, G. S. Schnakenberg, L. Shapiro, and L. Berger, Phys. Rev., **185**, 792 (1969).
- [100] Dinesh Martien, Introduction to AC susceptibility, Quantum Design (1994).
- [101] J. A. Mydosh, Spin glasses: an experimental introduction (Taylor & Francis, London, 1993).
- [102] D. Chowdhury and A. Mookerjee J. Phys. C: Solid State Phys., **7**, 5049 (1984).
- [103] P. Monod, J. J. Prejean and B. Tissier; J. Appl. Phys., **50**, 7324 (1979).
- [104] B. Skubic, J. Hellsvik, L. Nordström and O. Eriksson, J. Phys.: Condens. Matter, **20** 315203 (2008).
- [105] A. Mookerjee and S. B. Roy, Pramana, **14**, 11 (1980).
- [106] M. Gabay and G Toulouse, Phys. Rev. Lett., **47**, 201 (1981).
- [107] H. Maletta, G. Aeppli and S. M. Shapiro, Phys. Rev. Lett., **48**, 1490 (1982).
- [108] G. Aeppli, S. M. Shapiro, H. Maletta, R. J. Birgeneau and H. S. Chen, J. Appl. Phys., **55**, 1628 (1984).
- [109] M. Arai, Y. Ishikawa and H. Takei, J. Phys. Soc. Japan, **54**, 2279 (1985).
- [110] T. Dietl, H. Ohno and F. Matsukara, Phys. Rev. B, **63**, 195205 (2001).
- [111] T. Sato, T. Ando, T. Ogawa, S. Morimoto and A. Ito, Phys. Rev. B, **64**, 184432 (2001).

- [112] M. Sperl, A. Singh, U. Wurstbauer, S. K. Das, A. Sharma, M. Hirmer, W. Nolting, C. H. Back, W. Wegscheider, and G. Bayreuther, *Phys. Rev. B* **77**, 125212 (2008).
- [113] A. Singh, S. K. Das, A. Sharma and W. Nolting *J. Phys. Condens. Matter* **19**, 236213 (2007).
- [114] A. Singh, *Phys. Rev. B* **75**, 035206 (2007).
- [115] Subrat Kumar Das, Ph.D. Thesis, Indian Institute of Technology Kanpur (2008).
- [116] S. N. Kaul, *Phys. Rev. B* **27**, 5761 (1983), and references therein.
- [117] A. K. Majumdar, V. Oestreich, D. Weschenfelder, and F. E. Luborsky, *Phys. Rev. B* **27**, 5618 (1983).
- [118] W. Heisenberg, *Z. Phys.* **49**, 619 (1928).
- [119] E. C. Stoner, *Proc. R. Soc. London, Ser. A* **154**, 456 (1936).
- [120] S. Pandey and A. Singh, *Phys. Rev. B* **75**, 064412 (2007).
- [121] S. N. Kaul, *Phys. Rev. B* **24**, 6550 (1981).
- [122] S. N. Kaul and T. V. S. M. Mohan Babu, *J. Phys. Condens. Matter* **1**, 8509 (1989).
- [123] H. B. Callen, *Phys. Rev.* **130**, 890 (1963).
- [124] S. N. Kaul, *J. Magn. Magn. Mater.* **53**, 5 (1985).
- [125] M. S. Rao and S. N. Kaul, *J. Magn. Magn. Mater.* **147**, 149 (1995).
- [126] C. M. Haetinger, L. Ghivelder, J. Schaf, and P. Pureur, *J. Phys.: Condens. Matter* **21** 506006 (2009).
- [127] C. B. Murray, C.R. Kagan, and M.G. Bawendi, *Science*, **270**, 1335-1338, (1995).
- [128] J. Kondo, *Prog. Theor. Phys.* **32**, 37 (1964); J. S. Dugdale, *The Structures and Properties of Solids 5: The Electrical Properties of Metals and Alloys* (Edward Arnold, London, 1977).

- [129] G. Bergmann, Phys. Rep. **107**, 1 (1984); J. S. Dugdale, Contemp. Phys. **28**, 547 (1987) and references therein.
- [130] P. A. Lee and T. V. Ramakrishnan, Rev. Mod. Phys. **57**, 287 (1985).
- [131] E. A. Turov, Izv. Akad. Nauk SSSR, Ser. Fiz. **19**, 426 (1955).
- [132] T. Kasuya, Prog. Theor. Phys. **16**, 58 (1956).
- [133] I. Mannari, Prog. Theor. Phys. **22**, 335 (1959).
- [134] G. K. White and S. B. Woods, Philos. Trans. R. Soc. London, Ser. A **251**, 273 (1958).
- [135] E. Kondorsky, O. S. Galkina, and L. A. Tehernikova, *J. Appl. Phys.* **29**, 243 (1958).
- [136] D. A. Goodings, Phys. Rev. **132**, 542 (1963).
- [137] A. H. Wilson, Proc. R. Soc. London, Ser. A **167**, 580 (1938).
- [138] S. Chakraborty and A. K. Majumdar, J. Magn. Magn. Mater. **186**, 357 (1998).
- [139] A. Banerjee and A. K. Majumdar, Phys. Rev. B, **46**, 8958 (1992).
- [140] P. Khatua, T. K. Nath, and A. K. Majumdar, Phys. Rev. B, **73**, 064408 (2006).
- [141] C. Uher, R. Clarke, Guo-Guang Zheng, and I. K. Schuller, Phys. Rev. B, **30**, 453 (1984).
- [142] M. T. Perez-Frias and J. L. Vicent, Phys. Rev. B, **38**, 9503 (1988).
- [143] C.W. Chen, Magnetism and Metallurgy of Soft Magnetic Materials, Dover, New York (1986).
- [144] O. L. Boothby and R. M. Bozorth, J. Appl. Phys., **18**, 173 (1947).
- [145] E. I. Cooper, C. Bonhote, J. Heidmann, Y. Hsu, P. Kern, J. W. Lam, M. Ramasubramanian, N. Robertson, L. T. Romankiw, and H. Xu, IBM J. Res. Dev., **49**, 103 (2005).

- [146] W. P Taylor, M. Schneider, H. Baltes, and M. G. Allen, in Proceedings of Transducers 97, p. 1445 (1997).
- [147] Y. Zhuang, M. Vroubel, B. Rejaei, and J. N. Burghartz, *Solid-State Electron.*, **51**, 405 (2007).
- [148] T. Zhang, P. Zhang, H. W. Li, Y. H. Wu, and Y. S. Liu, *Mater. Chem. Phys.*, **108**, 325 (2008).
- [149] Q. Zhou, J. Velleuer, P. J. Heard, and Walther Schwarzacher, *Electrochemical and Solid-State Letters*, **12** (3), 7 (2009).
- [150] P. B. Narayan, R. D. Silkensen, and S. Dey, *J. Appl. Phys.* **73**, 6620 (1993).
- [151] V. Holý, U. Pietsch, and T. Baumbach, High resolution X-ray scattering from thin films and multilayers, Springer Tracts in Modern Physics, vol. **149** (Springer, Berlin, 1999).
- [152] N. Suresh, Rachana Thakur, D. M. Phase, and S. M. Chaudhari, *Vacuum*, **72**, 419 (2004).
- [153] S. K. Sinha, M. K. Sanyal, B. Carvalho, M. Rafailovich, J. Sokolov, X. Zhao, and W. Zhzo, Resonant anomalous X-ray scattering: theory and applications, Elsevier Science B.V., Amsterdam (1994).
- [154] S. Rai, M. K. Tiwari, G. S. Lodha, M. H. Modi, M. K. Chattopadhyay, S. Majumdar, S. Gardelis, Z. Viskadourakis, J. Giapintzakis, R. V. Nandedkar, S. B. Roy, and P. Chaddah, *Phys. Rev. B.* **73**, 035417 (2006).
- [155] Fundamentals of nanoscale film analysis, Terry L. Alford, Leonard C. Feldman, and James W. Mayer (Springer Science and Business Media, Inc. 2007).
- [156] S. Gliga, M. Yan, R. Hertel, C. M. Schneider, *Phys. Rev. B* **77**, 060404 (2008).
- [157] M. Barthelmess, C. Pels, A. Thieme, and G. Meier, *J. Appl. Phys* **95**, 5641 (2004).